

Project Number: ME – CF –OHO10

PACKAGING AND OPTIMIZATION OF A DIGITAL HOLOGRAPHIC OTOSCOPE FOR
CLINICAL USE

A Major Qualifying Project Report

Submitted to the Faculty of

WORCESTER POLYTECHNIC INSTITUTE

in partial fulfillment of the requirements for the

Degree of Bachelor of Science

in Mechanical Engineering

by

Simon Goldish

Timothy Kunyz

Christopher Lizewski

Daniel Olecki

Date: April 29, 2010

Keywords:

1. Digital Holography
2. Packaging
3. Spectroscopy

Professor Cosme Furlong

Abstract

Over the last four years, MQP teams have worked in conjunction with the Massachusetts Eye and Ear Infirmary (MEEI) and CHLST to develop an optoelectronic holographic otoscope (OEHO) with the purpose of measuring nanometer deformations in the human tympanic membrane. Although this technology is functional, its current configuration is not feasible for testing in clinical settings. This report details the steps taken to meet the diverse needs for optimization. Mechanical design and fabrication methods are described for a device that converts the experimental systems of the past to a reproducible, stable, and optimized modular tool. Methods of rapid prototyping and digital holography are introduced for obtaining a new generation of OEHO. The image quality of reconstructed images taken with this device are validated theoretically, analytically, and experimentally to demonstrate accuracy and reliability in medical applications. Tests pioneering the reflectivity of biologically compatible materials are also conducted for the maximization of laser reflectivity on the surface of the tympanic membrane. Subsequently, translation of this device to the MEEI will allow for next generation testing and analysis of auditory disorders in the clinic.

Acknowledgements

The group would like to thank Professor Cosme Furlong for his guidance and expertise expressed toward the project. Fellow graduate students working on aspects of this project provided invaluable data while analyzing and fabricating the system. Specifically, Nikhil Bapat for his organization and acoustics work, Ivo Dobrev for his mechanical and robotics work, and Ellery Harrington for his work optimizing the LaserView software. Dr. Maurico Flores also provided hours of guidance for optimizing the optical characteristics of the system. We are also thankful for the work of Dr. Jon Rosowski and his team at the Massachusetts Eye and Ear Infirmary for their co-research and development for this state of the art system.

Finally, we are grateful to the Mechanical Engineering Department of Worcester Polytechnic Institute for the unique opportunity to work on such a challenging and revolutionary project.

Table of Contents

Abstract	1
Acknowledgements	2
List of Figures	5
List of Tables	7
1. Introduction.....	1
2. Objectives	4
3. Background.....	5
3.1. Interferometry	5
3.2. Realization of Theory to Practice.....	6
3.3. Digital Holography	8
3.4. Acoustics.....	10
3.5. Alignment of Fiber Coupling System	10
3.6. Fabrication of Laser Subsystem Bases.....	14
3.6.1. Testing for Dimensions and Tolerances.....	15
3.7. Selection of Optical Components	19
3.7.1. Oscope	19
3.8 Stabilize Imaging Components	29
3.9. Attempt to Minimize Necessary DOF	31
4. Design of the Package.....	33
5. Fabrication of Prototype	39
6. Characterization of Optical Performance.....	41
6.1. Field of View	41
6.2. Magnification.....	42
6.3. Resolution	43
6.4. Depth of Field	44
7. Characterization of Mechanical Properties.....	46
7.1. Finite Element Analysis.....	46
7.1.1. Vibrations in Shell-Type Structures.....	46
7.1.2. ANSYS Analysis	48
7.1.3. Iteration Modifications.....	52
7.2. Second Iteration	53
7.3. Third Iteration	54
7.4 Acoustics Interface.....	56
8. Oscope Package Results	59

8.1. External Shape	59
8.1.1. Ergonomic Comfort	59
8.1.2. Easy interfacing with positioning arm	60
9. Conclusions and Recommendations	62
9.1. Otoscope Head	62
9.2. Thermo-Mechanical Effects.....	63
9.3. Packaging and Prototyping	63
10. Spectroscopy	66
10.1 Coatings Research.....	67
10.1.1 Titanium Dioxide and Cosmetic Make-Ups	67
10.1.2. Sublimating Waxes	68
10.1.3. Collodion.....	70
10.2. Decision on Chemicals Used	71
10.3. Methodology for Spectroscopic Analysis	73
10.3.1. Sample Materials	73
10.3.2. Initial Proposed Application Methods	74
10.3.3. Measuring Thickness	74
10.3.4. Uniformity.....	74
10.3.5. Workflow	75
10.3.6. Sample Mounting.....	75
10.3.7. Data Organization	75
10.4 Configuration of Testing Apparatus	76
10.4.1. Configuration 1	76
10.4.1.2 <i>Experimental Setup</i>	77
10.4.1.3. <i>Measurement Procedure</i>	80
Equations Used:	83
10.4.2. Configuration 2	85
10.4.4. Fringe Pattern Testing.....	86
10.4.5. Surface Interaction Experimentation	87
10.4.6. Configuration 3	89
10.4.7. LaserView Image captures.....	95
11. Spectroscopic Results	98
11.1. Comparing Different Application Methods at Different Concentrations	98
11.2. Comparing Titanium Dioxide to Zinc Oxide at Different Concentrations	100

11.3. Comparing Methyl Blue at Different Concentrations on Different Samples.....	101
11.4. Comparing the Three Coatings Using Their Most Reflective Methods	102
11.5. Repeated Data Analysis Using Specific Wavelength Excitation of the Samples	103
12. References.....	106
13. Appendix A.....	108
13.1. Deformation Shape at a Frequency for a Plate Constrained at its Edges	108
14. Appendix B.....	111
14.1. ANSYS Analysis of Iteration 2.....	111
14.2. ANSYS Analysis of Iteration 3.....	113
Appendix C.....	117
Technical Drawing for Iteration 1.....	117
Technical Drawings for Iteration 3	118

List of Figures

Fig. 1. The Inner Ear	2
Fig. 2. Human Ear Canal.....	8
Fig. 3: Recording and Reconstruction	9
Fig. 4. AOM Sensitivity Analysis.....	13
Fig. 5. Manufacturing Process Flow: From Stock to Alignment of Finished Pieces.....	14
Fig. 6. Newport New Focus 9091	15
Fig. 7. Image Size vs. Distance.....	17
Fig. 8. Angle of View vs. Object Distance	18
Fig. 9. Beam Splitter Cube Sensitivity.....	19
Fig. 10. Generation 2 Packaging.....	20
Fig. 11. Off-center Light Intensity	21
Fig. 12. Otoscope Head.....	22
Fig. 13. Otoscope Light Path	22
Fig. 14. Reference Beam (1), Object Beam (2), Beam Splitter Cube (3), Otoscope (4), Camera (5), Target (6).....	23
Fig. 15. Location of Otoscope in Ear Canal.....	24
Fig. 16. Otoscope Selection	24
Fig. 17. Heine Beta 200	25
Fig. 18. Heine Beta 200 Light Intensity Distribution	26
Fig. 19. Welych Allyn 3.5V Diagnostic Otoscope Head.....	27
Fig. 20. Exposed Diagnostic Otoscope Fiber Bundle	27
Fig. 21. Welych Allyn Light Intensity Distribution.....	28
Fig. 22. RD-407 Latex	30
Fig. 23. First Package Iteration with Top (left) Off and (right) On	33
Fig. 24. Otoscope Head Attachment Rail	35
Fig. 25. (left) Beamsplitter Cube Stage (right) Method of Rotation.....	36
Fig. 26. (left) Fiber Collar (Section View) (right) Internal View of Collars	37

Fig. 27. Internal Components of Iteration 1	38
Fig. 28. Rapid Prototype - Iteration 1 (left) bottom (right) top.....	40
Fig. 29. Assembled and Illuminated Prototype.....	40
Fig. 30. Field of View and Magnification of Image	42
Fig. 31. 1951 USAF Spatial Resolution Test Card.....	43
Fig. 32. 1951 USAF Holographic Image Test	44
Fig. 33. Sample Depth of Field Setup.....	45
Fig. 34. Depth of Field Test	45
Fig. 36. First 20 FNF for Iteration 1	48
Fig. 37. ANSYS: Fundamental Natural Frequencies of Vibration	49
Fig. 38. ANSYS: Total Deformation	50
Fig. 39. ANSYS: Equivalent Stress	51
Fig. 40. 2nd Iteration (left) Solid Isometric View (right) Transparent Side View	54
Fig. 41. Iteration 3 Package Design (left) Isometric View (right) Transparent Side View	56
Fig. 42. Acoustic System (left) Transparent Top Shell (right) Assembled on Second Iteration ..	57
Fig. 43. (left) Conventional Oscope (right) OEHO Prototype.....	59
Fig. 44. Bogen Monfrotto Grip Action Ball Head.....	61
Fig. 45. Thorlabs OSL1 Illuminator with Tungsten Lamp	76
Fig. 46. Tristan USB Spectrometer.....	77
Fig. 47. (left) Light Emitting Cage and (right) Light Gathering Cage	78
Fig. 48. Experimental Setup (front)	79
Fig. 49. Experimental Setup (back)	79
Fig. 50. Raw Data of Reference.....	80
Fig. 51. Raw Data of Green Sample	81
Fig. 52. Raw Data of Reference and Sample	82
Fig. 55. Percent Transmission of Green Sample.....	84
Fig. 56. Absorption Spectrum of Green Sample.....	84
Fig. 57. Configuration 2 Setup.....	86
Fig. 58. Fringe Pattern Testing Setup	87
Fig. 59. Comparison of Different Concentrations of Decyl Glucoside	88
Fig. 60. Contact Angle	88
Fig. 61. Spectroscopy Setup - Configuration 3 and Reference Probe	89
Fig. 62. SpectraSuite Toolbar	90
Fig. 63. SpectraSuite Output of Saturated Sample	90
Fig. 64. Error in Gamma Assumptions	93
Fig. 65. Full Spectrum Reflectance - 700mg TiO ₂ Drop Brushed.....	95
Fig. 66. Numerical Focusing Using Digital Holography	96
Fig. 67. Fringe Pattern Testing with Different Coatings	97
Fig. 68. Measure of Reflectance between Application Methods of Titanium Dioxide at 450mg (Full Spectrum)	98
Fig. 69. Measure of Reflectance between Application Methods of Titanium Dioxide at 700mg (Full Spectrum)	98
Fig. 70. Measure of Reflectance between Application Methods of Titanium Dioxide at 250mg (Full Spectrum)	99
Fig. 71. Comparing Titanium Dioxide to Zinc Oxide at Different Concentrations.....	100
Fig. 72. Comparing Methyl Blue at Different Concentrations on Different Samples	101

Fig. 73. Comparing the Three Coatings Using Their Most Reflective Methods	102
Fig. 74. Comparison of Reflectance between Application Methods of Titanium Dioxide at 400mg	103
Fig. 75. Comparison of Reflectance between Application Methods of Titanium Dioxide at 700mg	103
Fig. 76. Comparison of Reflectance between Application Methods of Titanium Dioxide at 250mg	104
Fig. 77. Comparison of Reflectance between Concentrations of Methyl Blue	104

List of Tables

Table 1. Mechanical Properties of RD-407 Latex	29
Table 2. 1951 USAF Spatial Resolution Spreadsheet	44
Table 3. ANSYS: First 20 FNF for Iteration 1	49
Table 4: Table of Chemicals and Concentrations Used.....	72

1. Introduction

The tympanic membrane (TM) is part of a complex system of tissue and bone that allows for the sense of hearing. As sound waves enter the ear canal, the TM absorbs kinetic energy. The kinetic energy is then transmitted through a four-bar linkage made from three bones: the malleus, incus, and stapes. This can be seen in Fig. 1 below. The kinetic energy from the sound waves forces the TM to oscillate in a specific pattern resulting from the frequency and amplitude of the sound waves. The pattern of oscillation that the TM undergoes defines the frequency that the stapes vibrates at while in contact with the fluid of the inner ear. It is at the inner ear where hairs transmit signals to nerves as the brain interprets electrical pulses to psychoacoustic sounds. This system also acts as a sound amplifier. Acoustic vibrations in the air can carry little kinetic energy. However, transmitting acoustic signals from the air to a fluid in the inner ear provides a denser medium for the sound waves to travel through. Therefore, the acoustic signals can gain velocity through the fluid and provide a more substantial kinetic energy for sound signals to the brain.

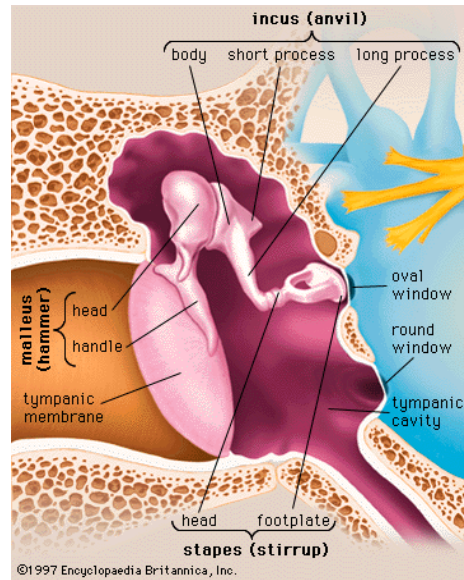


Fig. 1. The Inner Ear

Despite the substantial knowledge of how the mammalian auditory system works, there is still little quantitative data regarding the mechanical aspects of the ear relating to hearing quality. Diagnosis of hearing illness is done almost exclusively by qualitative examination of the TM. Surgical procedures exist to repair tears and fractures in the bone and membranes of the middle ear, but there is no optimized method for diagnosing injury for reparation. Therefore, answers are being sought for the development of a tool to perform quantitative measurements of the tympanic membranes response to acoustic stimuli.

The current practiced method for measuring the mechanics of the TM is a process called laser tympanometry which uses Laser Doppler Vibrometry to measure frequency response. A laser vibrometer is equipped with a specialized speculum outfitted with an acoustic delivery system. The acoustic source is used to excite the surface of the tympanic membrane at a certain frequency. The laser vibrometer is aimed at a chosen point on the ear drum, typically near the umbo, and measures the deformations at that single location (H. Mojallal). Measurements are

made using the principles of laser interferometry. The main drawback to this method of ontological diagnosing is the limited region within which the measurement is taken. By only calculating the deformations at a single point, the rest of the surface of the TM remains a mystery, allowing for potential misdiagnoses or further prolonged invasive testing.

2. Objectives

The betterment of methods for tympanic membrane observation is essential for the advancement of audiology. The following bullets outline the key objectives to meeting the needs of the third generation of optoelectronic holographic otoscope:

- **Selection of optical components:** *Development of a simplified, efficient data capturing system*
- **Miniaturization of previous generations:** *Sizing of a package to allow for ease of maneuverability*
- **Packaging of the otoscope head assembly:** *Design of an assembly that optimizes the alignment of optical components with minimal degrees of freedom*
- **Stabilization of the system:** *Ensure static conditions during data acquisition for optimal holographic image quality*
- **Validation of the integrity of the holographic images produced:** *Prove that the holographic image quality of the redesigned clinical system has not diminished at the expense of package size*

3. Background

3.1. Interferometry

Since the vibrations that occur in the tympanic membrane are at the sub-nanometer level, the only practical method that currently exists to measure them with a full field of view is with a laser system. Until this past year, the method of laser imaging used was classic holographic interferometry. The method of holographic interferometry uses the superposition of two laser beams to produce a holographic image. This process is performed in two steps: recording, and optical reconstruction. The recording is done by shining an illumination beam at an object, which then reflects back onto a photosensitive holographic plate, and simultaneously shining a reference beam at the same holographic plate. The beam that is reflected back, known as the object beam, recombines with the reference beam to generate an image that is capable of conveying information about brightness, contrast, and depth. On the other hand, an image taken with a camera and no laser simply records the intensity of light. The additional data provided in the holographic image is due to the difference in phase of the laser beams. The reconstruction of the image is done by shining the reference beam at the holographic plate through lenses and visually observing the image with the naked eye.

Unfortunately, there are several shortfalls to using holographic interferometry for laser imaging. A key limitation is the immobility of the system. The previous generations of the system is fairly large with all components fixed to a table. The size and rigidity of this system makes it extremely difficult to use on live humans. The system is very unstable because everything is mounted on posts. This allows all components to vibrate independently, resulting in unreliable measurements. Additionally, previous generations of the system require lenses with

a four inch focal length to focus the image, meaning that the smallest possible package would be far too burdensome to handle in a clinical environment.

3.2. Realization of Theory to Practice

Much progress has been made in the development of a working clinical otoscope since the 2009 MQP. However, there is still much to be done to achieve a hospital-ready device. The main issue was the interaction between the otoscope and reference assembly with the environment. Inherent instabilities resulted making it impossible to use in a clinical setting.

The current setup is mounted on a breadboard plate which is, in turn, bolted to a pneumatically controlled vibration isolating table. While this isolation adds a certain amount of stability to the system, additional control is necessary. Individual parts of the otoscope assembly are mounted on Thorlabs PH Ø½” posts. These posts are then secured to a breadboard by UPH Post Holders. This gives each component a minimum of two degrees of freedom. Although such flexibility is desirable from the standpoint of alignment and fine tuning, it adds an element of volatility. Parts of the system assembly are not interconnected, leaving them free to move from each other due to ambient temperature changes, noise, and vibrations. By extending the components above the tabletop by use of posts, moment arms are created which amplify unwanted vibrations from the surroundings.

Interferences from these vibrations have an adverse effect on the optical recreation of the observed fringe pattern on the computer. This issue is most noticeable on the lab monitors when no test is being run and the static test sample is undergoing examination. Upon viewing the monitors, a flickering can be noticed in the image. People walking in proximity to the system, ambient sounds, heat, and thermal changes all have an undesirable effect on the quality of the

image. In a clinical setting, this type of disturbance is unacceptable. Patient motion, motion of machinery in the room, and the constant movement of the doctor while performing his/her duties all effect the stability of the system. If the size of the system is compressed into a single unit that is rigidly secured, these difficulties can be overcome. A patient's heartbeat also has an adverse effect on the overall quality of the holographic image. Since the tympanic membrane is an interconnected part of the auditory system, it is affected by the blood flow to surrounding elements.

As aforementioned, the most limiting factor in the previous iteration was its lack of portability. Portability and a decent range of motion are critical for being able to use the otoscope on a living patient. It takes up roughly 1ft² of table space and would not be reasonable to move around a patient. Aside from vibrational effects from the posts, relative motion between the fiber patch cords delivering the illumination sources from the laser subsystem causes distortion in the output. Thus, the cables are secured to the table where they are unable to move and alter the quality of illumination delivered in the form of the object and reference beams.

As shown in Fig. 2. Human Ear Canal below (), the inner ear is seen to be made of complex curves and geometries; it is not a straight path to the tympanic membrane. Due to this complex nature of the human ear, it would be impractical and unsafe to move the patient around the rigid tip of the otoscope's speculum.

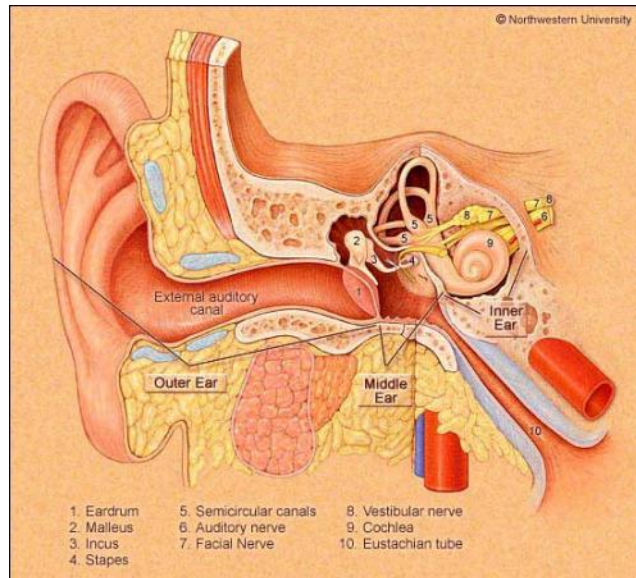


Fig. 2. Human Ear Canal (Hain, 2010)

Patient head movement including twitching and the fact that every ear canal is of a different shape further complicate the otoscope insertion process. Moving the entire body with an acceptable range of motion to ensure a good view of the TM would require an impractical amount of force and precision.

3.3. Digital Holography

A first step to minimizing the size of the package is to eliminate the need for lenses. This is done through the use of digital holography. Similar to interferometry, digital holography (DH) takes place in two steps: recording using a charge coupled device (CCD) camera and numerical reconstruction. The difference in the recording process is that a CCD camera is used to digitally record the hologram instead of a photosensitive plate. More importantly, the difference in the reconstruction process is that it is done numerically by computer software (i.e. without lenses). This provides the ability to take high-speed measurements with comparable image quality in a compact lens-less system. The equations used for digital holography as well as the recording and

reconstruction processes are shown below in Fig. 3: Recording and Reconstruction.

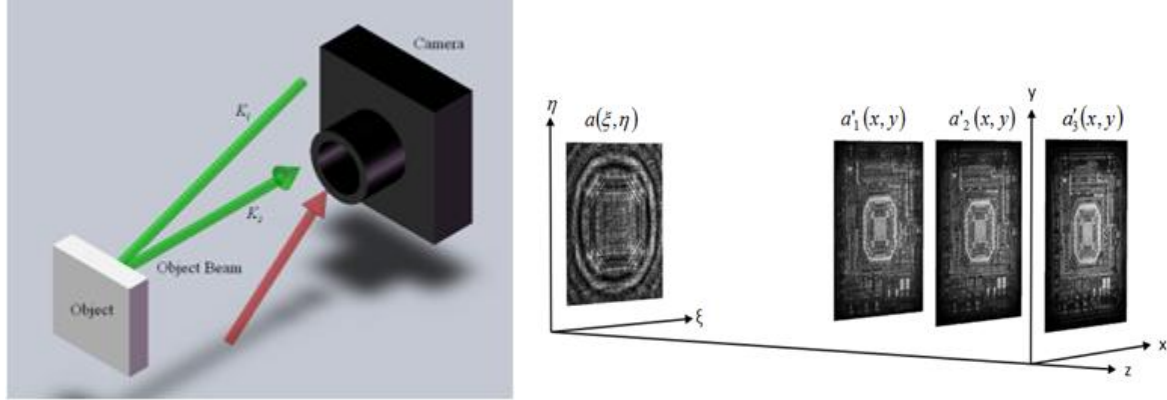


Fig. 3: Recording and Reconstruction

$$I_n(x, y) = I_B(x, y) + I_M(x, y) \cos[\Delta\phi(x, y) + \Omega + \theta_n] \quad (3.1)$$

$$\Omega = (\mathbf{K}_2 - \mathbf{K}_1) \cdot \mathbf{L} \quad (3.2)$$

$$a(\xi, \eta) = (I_1 - I_3) + i(I_4 - I_2) \quad (3.3)$$

$$a'(x, y) = \frac{1}{i\lambda} \iint a(\xi, \eta) \frac{1}{r} \exp(-ikr) \cos\Theta \, d\xi \, d\eta \quad (3.4)$$

$$r = \sqrt{(x - \xi)^2 + (y - \eta)^2 + z^2} \quad (3.5)$$

The intensity I_n (3.1) is the intensity of the light recorded at different phases 1 through 4. It is calculated by recording the brightness I_B and contrast I_M along with the Fringe Locus Function Ω (3.2). This function is defined as the difference between the illumination and observation vectors ($\mathbf{K}_1, \mathbf{K}_2$), and the displacement vector (\mathbf{L}). Once the Intensities I_1 through I_4 are recorded, a complex light distribution \mathbf{a} is created (3.3). This complex light distribution is then substituted into the Rayleigh-Sommerfeld integral (3.4). This integral acts as a Fourier transform, and converts the complex distribution into a holographic image pixel by pixel using a variable r (3.5), the reconstruction vector. This vector is largely based on a parameter z , the

reconstruction distance. This value z represents a virtual distance away from the camera plane at which the image is portrayed. The reconstruction distance is adjusted via a software interface (i.e. no rearranging of the laser setup or sample) and is what allows for the numerical focusing.

3.4. Acoustics

In order to fully investigate behavior of the tympanic membrane, readings must be taken in conjunction with a precisely generated acoustic stimulus. Diagnosis of the tympanic membrane can be performed by investigating its dynamics in response to a specific tone. Currently, membranes being viewed with the system are excited with a large speaker which is set up behind the membrane. This is feasible merely because the membrane has been isolated. In a real clinical setting there would be no way to place a speaker behind a patient's tympanic membrane.

Commercial otoscopes provide channels which can generate a very basic pressure across the membrane, however more advanced micro packaging need to be designed. These would allow for exact stimulation to drive the membrane. However, with this additional subsystem, additional complexities arise. The acoustical energy which may bleed off of the excitation channels could cause disruptions to the imaging system. Particular natural frequencies of the package could be excited with enough force to render the system unusable if not carefully avoided. For this reason, the design must take into consideration the complex interaction between geometries and materials with acoustic excitation present.

3.5. Alignment of Fiber Coupling System

As outlined in the 2009 MQP report, an integral component of the holography system is the laser subsystem that splits and transmits the object and reference beams through fiber optic

patch cords. The division of the singular coherent laser beam into two beams at a ratio of 80:20 is due to a precisely toleranced beam splitter cube. The cube has an exact 45° angle reflective surface to split the laser into perpendicular directions. The beams then reflect off mirrors that direct the beams through objective lenses and finally into the fiber optic cables. This amounts for a total of five redirections and two precise collimations. Since the openings for the fibers are only five microns in diameter, the alignment of all devices must be exact to achieve optimal coupling efficiency. However, each of the subsystem coupling components has varying degrees of freedom for proper alignment. Thus, it is essential that each component be aligned at the correct height to have a basis from which to begin the positioning process.

In the previous design, each component was fastened atop a precision machined aluminum base that was attached to a common breadboard. It was determined that this system was capable of producing acceptable results, so the same design was replicated for a second iteration. Dimensions were measured from the existing pieces and solid models were created to use when machining the new pieces.

For the bases that support the New Focus 9131 and GM100 components, there are two basic elements that comprise its design. Essentially, the two bases are of congruent profiles with different lengths, widths, and overall heights. The structure consists of two rails that attach the base to the breadboard and a raised plateau to which the New Focus 9131 and GM100 devices are fastened. The rails are identical in height and have similarly sized holes drilled into them for the bolts to fit. These slots allow for rough adjustments to the position and angle of each component by altering the location of the bolt along their length.

The base for the AOM and beam splitter cube, however, requires a different level of precision and care in sizing. The efficiency of the beam transmittance through the AOM is wholly dependent on its incident position through the modulating window. By altering the Bragg angle and the location of the laser in the window, the laser output strength can be optimized.

Essentially the base consists of a thin bottom with a pedestal upon which the beam splitter is secured. This height for the platform was obtained from measurements of the first generation system. The vertical location of the beam splitter has a larger allowable tolerance than the rest of the system because the beam splitter has the same reflectance quality along its height. The goal was to have the beam strike the middle of the cube so that there would be available adjustability in all directions. To adjust the cube and AOM assembly, a Newport Linear Stage, Model TSX-1D, was interfaced between the aluminum piece and the breadboard. This stage allowed for a linear travel adjustment of 1 in. It was aligned so that the motion would be perpendicular to the laser, permitting horizontal fine tuning of the AOM.

To adjust the Bragg angle of the incident beam, a New Focus single axis stage is used to attach the AOM module to the base. Since the stages and the modulator window are of standard dimensions set by their manufacturers, the height of the aluminum bottom is critical. The height sets the vertical position of the AOM, and since it is a machined piece, it cannot be adjusted once cut. Therefore, a test setup was designed to determine the optimal height of the laser entering the AOM. In this setup, three axes of nanopositioners were used to adjust the height, translation, and depth of the laser entering the AOM while the output intensity was measured. The pitch of the laser traveling through the AOM was also characterized by intensity. The results are displayed below in Fig. 4. AOM Sensitivity Analysis.

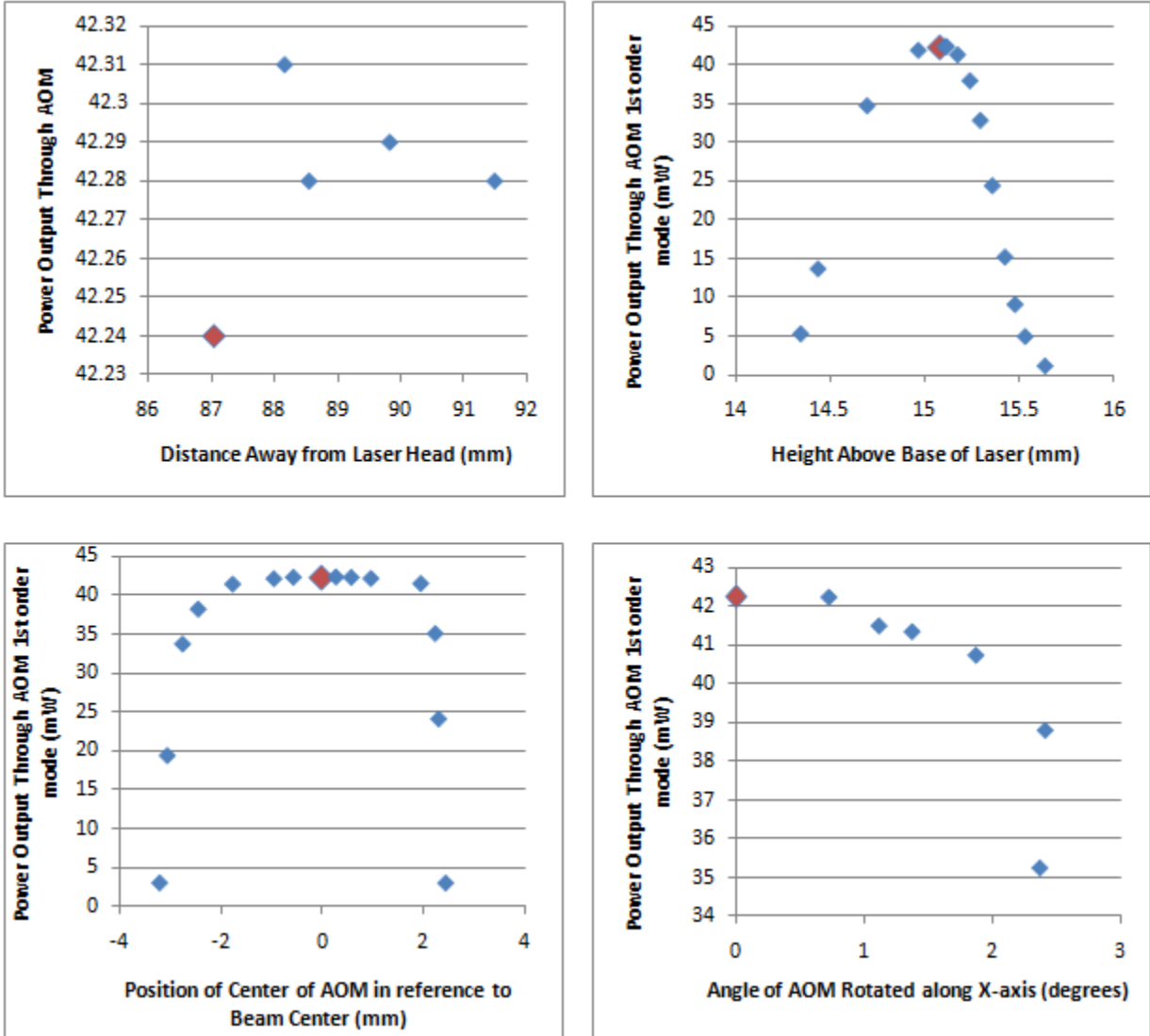


Fig. 4. AOM Sensitivity Analysis

3.6. Fabrication of Laser Subsystem Bases

After the designing and dimensioning of the new bases was completed, CAD models were created in SolidWorks 2009. The 3D parts were integrated into the overall subsystem model as well as used to develop the CAM operations. The cutting of the metal stock was done automatically using the HAAS TM-1 CNC machine. GibbsCAM was used to create the necessary command code for the TM-1 to accurately cut the parts. After the tool paths were created, the final step was to machine the bases.

First, the stock had to be rough cut to size from a larger block of aluminum. Due to its availability from Washburn Labs, 7000 series aluminum was used. After rough blocks were portioned using a horizontal band saw, they were squared using a DoAll manual mill and readied for the final machining process in the CNC machine. When adequately prepared, the aluminum stock pieces were cut to the designated dimensions. This process concluded the preparation of the aluminum bases for the new laser subsystem.

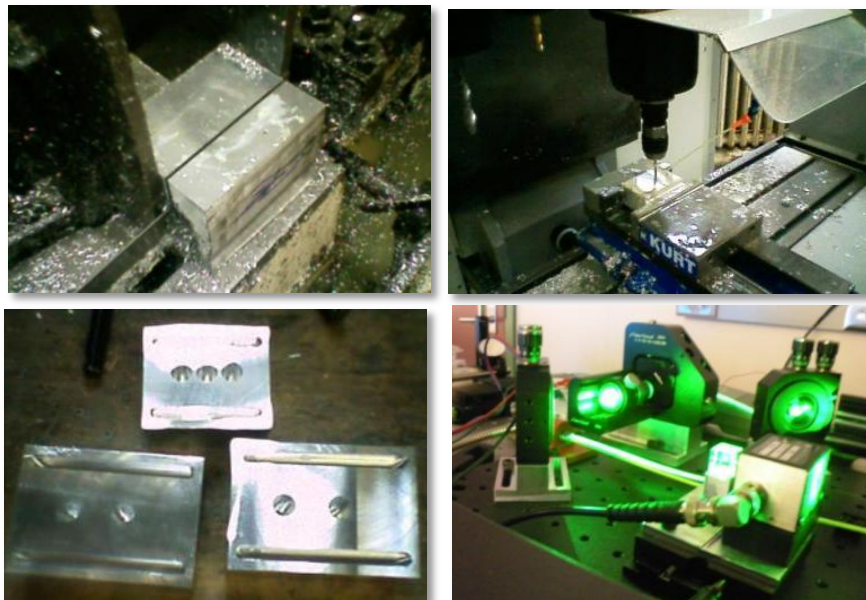


Fig. 5. Manufacturing Process Flow: From Stock to Alignment of Finished Pieces

3.6.1. Testing for Dimensions and Tolerances

The alignment of the fiber optic cables to the laser subsystem required the precision mating of the object and reference beams to the cables themselves. This was done through the use of a Newport New Focus 9091 fiber coupler.



Fig. 6. Newport New Focus 9091 (Newport Corporation)

This is a five axis positioning system to adjust the yaw, pitch, and xyz translation of a stage that holds a fiber optic cable. Once the cable is attached to this stage and the laser is directed toward its opening, fine adjustments can take place. Each of the five axes is adjusted individually while a photometer is used to measure the amount of light being transmitted at the other end of the cable. Each axis is adjusted until the maximum amount of power is transmitted through the fiber optic cable. This is a lengthy iterative process, as each axis must be realigned after the intensity of the light is changed to ensure that it is maximized for optimal light transmission. The amount of light that is transmitted in the reference and object beams are different because of the required light necessary for their purposes. This is why the 80/20 beam splitter cube is utilized in this setup. The object beam must provide enough light intensity to reflect off of the target sample and back into the silicon camera. On the other hand, the reference beam is reflected directly from the beam splitter cube into the camera. Therefore, the object

beam requires far more intensity. A reasonable efficiency for laser to fiber alignment is about 95%. In our system, an efficiency of 92% was achieved to provide an intensity of 36.8 mW from the object beam and about 9.2 mW from the reference beam. This is an increase of 460% in intensity from the previous year's system. This is partly due to our introduction of a 50 mW laser opposed to last year's 20 mW laser.

Upon completion of the laser subsystem, the parameters of the optical package must be established. This was completed through experimental procedures and calculations for optimizing efficiency based on the characteristics of the laser and devices used. The first step is to ensure that the fiber optic cables are the correct distances from their target objects.

A fiber optic cable has a specific angle at which a light source exits. This is known as its numerical aperture. The aperture on the cables that were used is 0.13. Thus, it is possible to calculate the optimal distance from the end of the fiber optic cable to the target based on the size of the target. A difficulty with this is that laser light has a Gaussian distribution of its intensity. This means that the optimal distance may not match the theoretical because of its decay in intensity as the perimeter of the beam is reached. Also, for our application, the target of the laser contains a large variation in uniformity from loose quality control in polishing and dead fiber minimization. This requires practical testing as well, where distances of the fiber to the target are tested and graphed accordingly.

The next parameter to optimize is the distances between the otoscope, beam splitter cube, and camera. The device used to transmit the object beam has a circular orifice at its end where the light is transmitted back to the camera. Thus, the calculation to maximize the field of view to the camera is purely geometrical. As the circular orifice is brought closer to the camera, its

perimeter is effectively increased. This is because a camera interprets light intensity in a two dimensional world. If an object is far from the camera, it appears small. If an object is close to the camera, the object appears large. Therefore, by bringing the orifice as close as possible to the camera, the range of view can be maximized because the opening of the orifice appears larger.

This is shown in equation 3.6 below.

$$i = \frac{o}{d} f \tag{3.6}$$

Where i is the image dimension, d is the distance of the camera to the orifice, o is the dimension of the orifice, and f is the focal length. Because the dimension of the orifice and focal length change little in relation to each other, the only variable parameter is the distance of the camera to the orifice. Therefore, the relationship between image size and distance to the camera is shown in Fig. 7. Image Size vs. Distance.

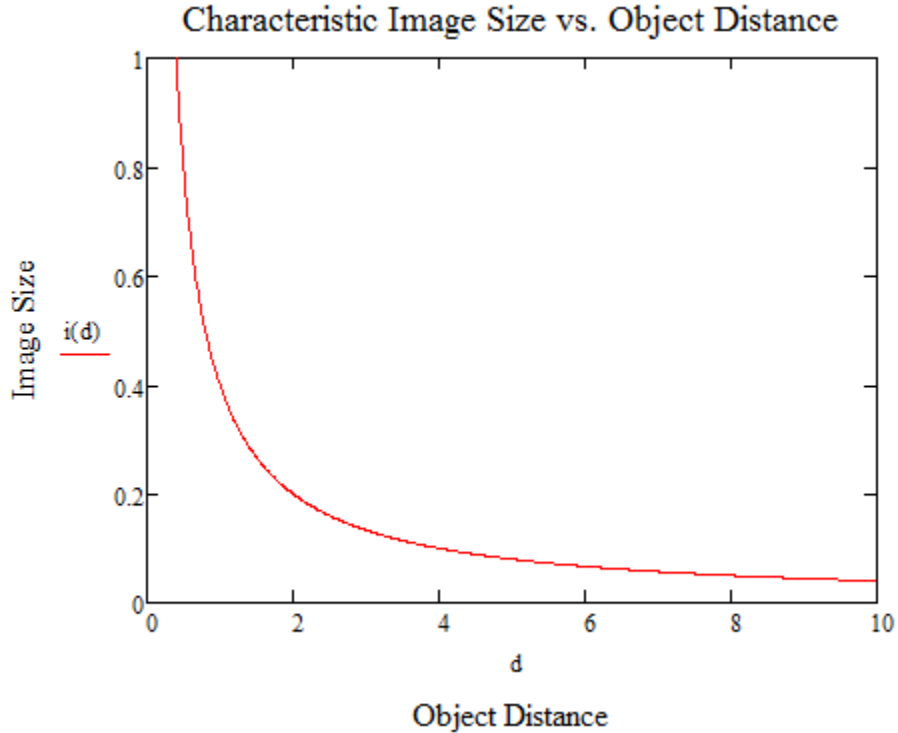


Fig. 7. Image Size vs. Distance

This also directly correlates with the area of view calculation for cameras:

$$AOV = 2\arctan\left(\frac{i}{2f}\right) \quad (3.7)$$

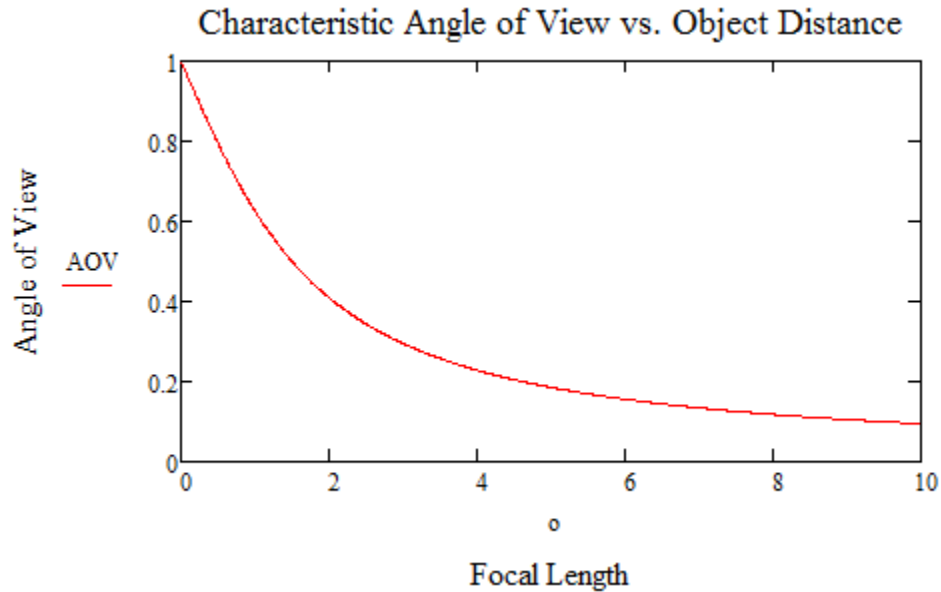


Fig. 8. Angle of View vs. Object Distance

Thus, minimizing the distance between the camera and the object maximizes the potential image size.

The next essential tolerance to specify is the angle at which the reference beam and object beam contact the camera. If the angle is too great, insufficient modulation, poor contrast, and off-center images are likely to occur. Therefore, nanopositioners were used to modify the angle of the beam splitter cube as images were recorded. A plot was formed to show the optimized holographic image quality in relation to angle of contact between the reference beam, object beam, and beam splitter cube in Fig. 9. Beam Splitter Cube Sensitivity.

Center of Otoscope Orifice on Camera vs. Angle of Beam Splitter Cube

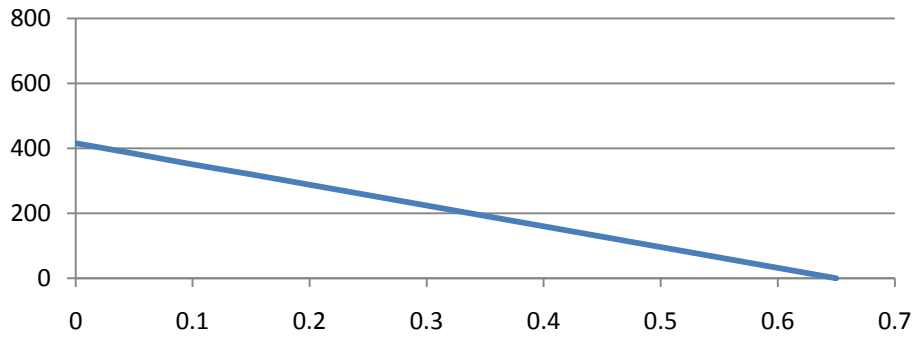


Fig. 9. Beam Splitter Cube Sensitivity

Based on the dimensions necessary to provide high quality data, a proper method must be determined to produce the system. Seeing that the tolerances cannot exceed 0.50 degrees of misalignment, a tolerance of 0.004 inches must be met. This is very reasonable, as machining tolerances at shops in WPI surpass 0.001 inches for manual DoALL mills and lathes as well as the automated HAAS Mini-mills.

3.7. Selection of Optical Components

3.7.1. Otoscope

One of the most critical innovations to this packaging system is the introduction of the otoscope head. In previous generations, the target sample had been illuminated by aiming the object beam around the speculum. A 50/50 beam splitter cube was then used to combine the

light from the speculum with the reference beam, shown in Fig. 10. Generation 2 Packaging.

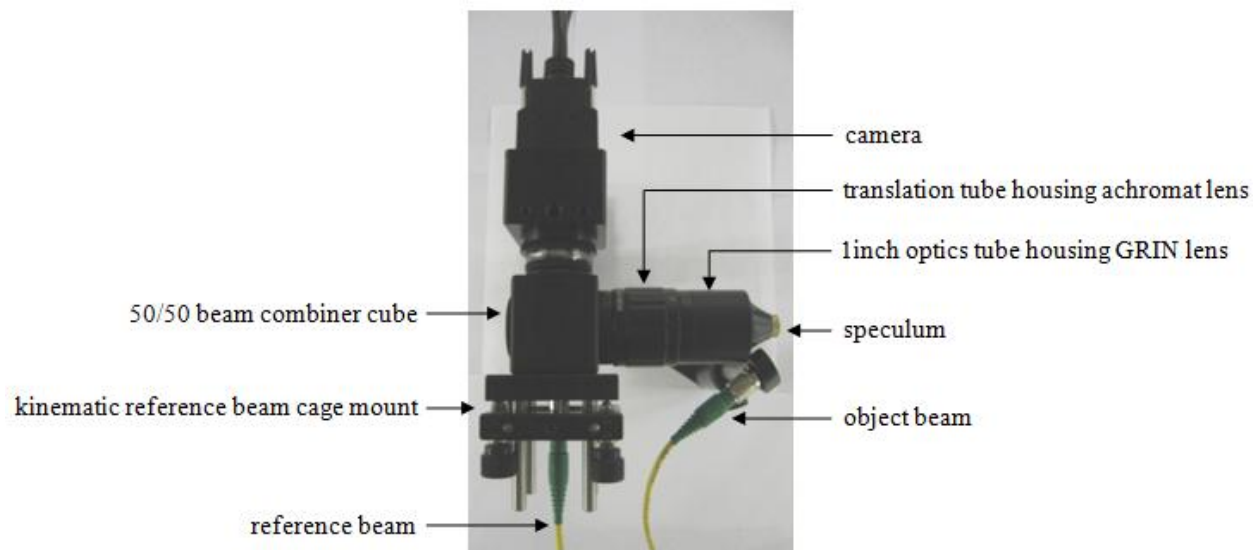


Fig. 10. Generation 2 Packaging

Since the object beam and speculum cannot be axially aligned, the system is very inefficient. This causes significant shadowing in the resulting holographic image. It is impossible to ensure equal intensity of light on the target sample when laser light is being delivered directly from the object beam's cable because of the Gaussian distribution of intensity. The resulting intensity distribution is shown in Fig. 11. Off-center Light Intensity where the most intense light is off centered.

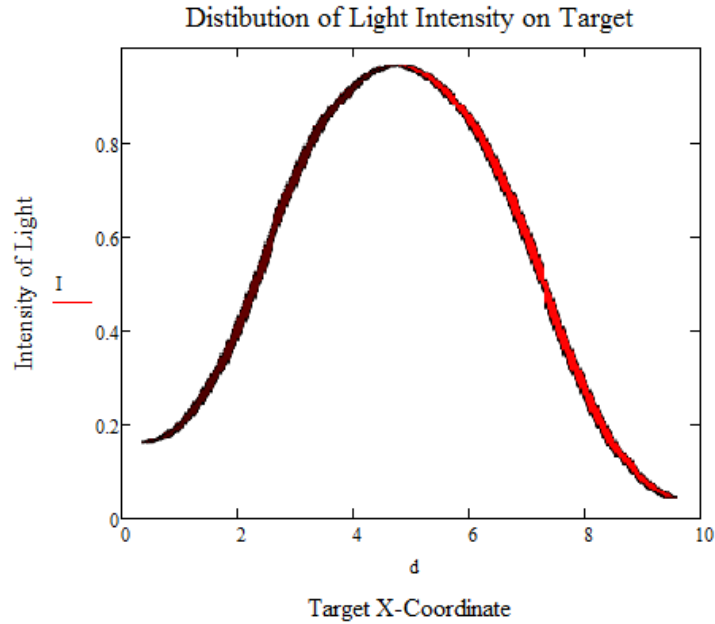


Fig. 11. Off-center Light Intensity

The most appropriate way to remedy this issue would be to axially align the object beam with the speculum. The result would be a perfect distribution of light intensity across the target sample. A concurring result would be improved image quality which is directly related to the equations for digital holography. Because the brightness for each pixel is the same, the Rayleigh-Sommerfield integral will produce results that only vary from the contrast detected by the camera.

The best option for achieving axial alignment is by evenly distributing the light around the camera. A device that is currently available for this use is the clinical otoscope, shown in Fig. 12. Otoscope Head.



Fig. 12. Otoscope Head

The otoscope is made of ABS plastic and wrapped with a fiber-optic cable bundle. Traditionally, a light emitting diode is placed in the handle of the otoscope where the fiber bundle converges. Light is transmitted through the bundle and around the casing to the speculum. At the speculum, the fibers terminate in a circular pattern around the speculum's tip. This provides for even distribution of light as each cable carries light of identical intensity. This is ideal for our application because it provides a 7 mm diameter opening where the light from the object beam can be reflected directly back through to the camera as seen in Fig. 13. Otoscope Light Path.

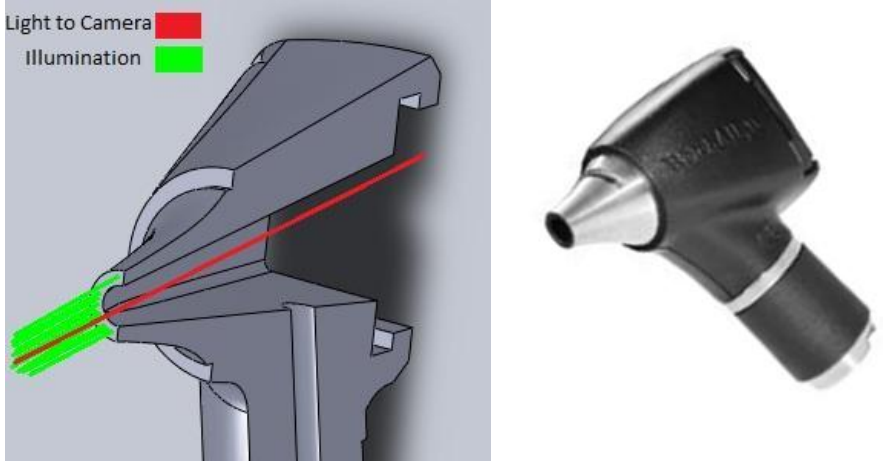


Fig. 13. Otoscope Light Path

Using an otoscope as the light delivery system greatly simplifies the arrangement of the system. Rather than requiring side mounts and angle optimization, every component is aligned axially as shown in Fig. 14. Reference Beam (1), Object Beam (2), Beam Splitter Cube (3), Otoscope (4), Camera (5), Target (6)

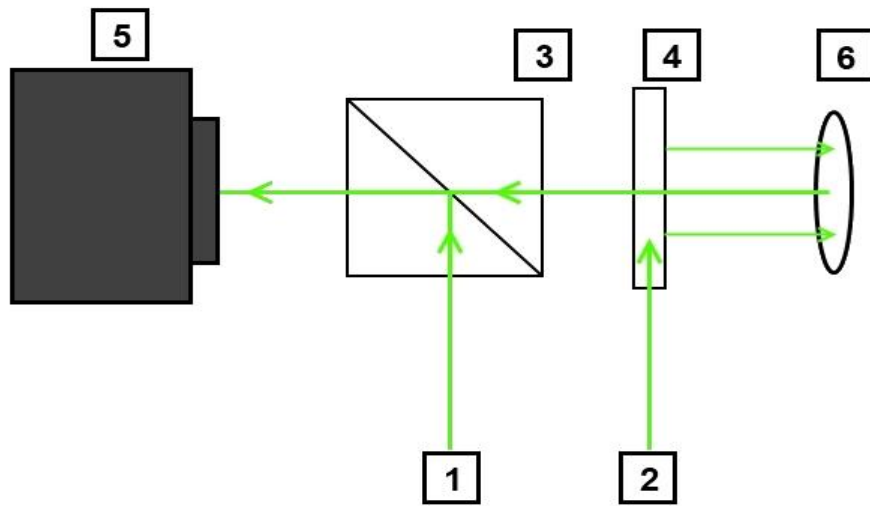


Fig. 14. Reference Beam (1), Object Beam (2), Beam Splitter Cube (3), Otoscope (4), Camera (5), Target (6)

Other benefits include: the object and reference beams approaching the system from the same position, miniaturized form, auto-distribution of light, and use of off the shelf components to simplify the manufacturing process. Another key implication of using the otoscope head is that its shape is already optimized for auditory examinations. The speculum is contoured to fit comfortably inside a human ear canal while the distance from the end of the speculum to the tympanic membrane is already optimized for a maximum viewing angle. An example of the otoscope's position in an ear canal is shown in Fig. 15. Location of Otoscope in Ear Canal.

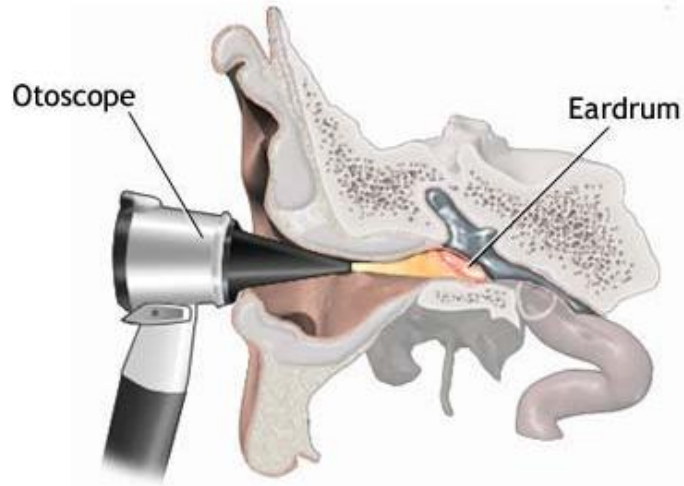


Fig. 15. Location of Otoscope in Ear Canal

A variety of otoscope heads are available, two of the most reputable being Welych Allyn and Heine. Several different models were ordered for comparison including Welych Allyn's: Pneumatic, Pocketview, Diagnostic, and Macroview otoscopes, and Heine's Beta 200 Otoscope shown in order from left to right in Fig. 16. Otoscope Selection. For our purposes, there are two important characteristics for these otoscopes: mechanical stability and fiber optic quality.



Fig. 16. Otoscope Selection

It was easy to eliminate the Pneumatic and Macroview otoscopes because the Pneumatic otoscope did not have an orifice between the cables at its tip to allow axial alignment. The Macroview was almost twice as large as the other otoscopes due to the incorporation of lenses

for focusing. However a lens stage is obsolete with digital holography. By examination of the tip of the Pocketscope it was determined that the distribution of the fiber optic cables around the orifice is heavily concentrated toward the top, leaving the bottom almost bare. This is unacceptable for even illumination. Therefore, the two best options are the Heine Beta 200 and the Welych Allyn 3.5V Diagnostic Oscopes.

The Heine Beta 200 (Fig. 17. Heine Beta 200) is made from stainless steel with all major shapes comprising of concentric circles and a screw above the viewing opening. This is a very mechanically stable construction as circles are ideal load bearing shapes. Furthermore, stainless steel has tensile and yield strengths of 860 MPa and 502 MPa respectively and a modulus of elasticity of about 200 GPa, which is nearly five times stronger than aluminum. Also, the screw opening in the back is ideal for fastening the otoscope head to a package base.



Fig. 17. Heine Beta 200

All of these properties contribute to a very mechanically sound device capable of withstanding forces with little resulting deformation. However, the analysis of the Beta 200's fiber optic quality proved to be less than desirable. It was found that there were many dead

fibers and improper polishing of fiber tips was evident in each head analyzed. This was done by coupling the laser to the input of the otoscope head and placing the tip of the speculum 1 mm from the face of the camera. Then, using LaserView's software, we were able to determine the intensity of the light around the ring of the entire speculum shown in Fig. 18. Heine Beta 200 Light Intensity Distribution.

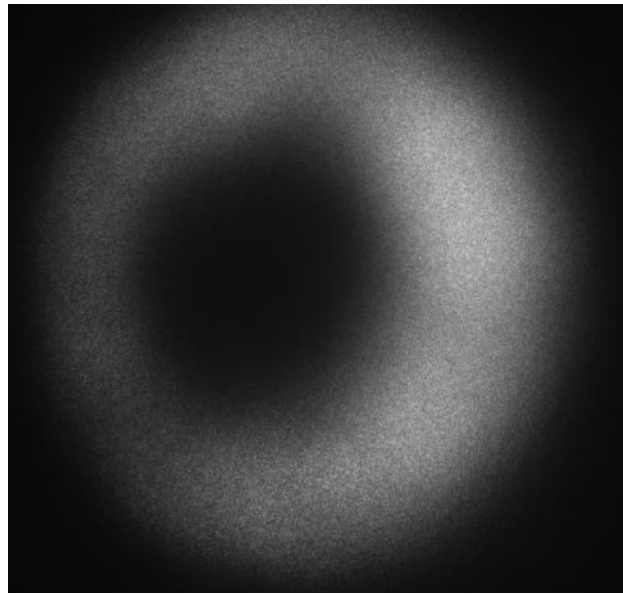


Fig. 18. Heine Beta 200 Light Intensity Distribution

From this picture it is apparent that light distribution around the speculum tip is not uniform. This is expected to be from the manufacturing procedure and quality control on the device. The otoscope is made by holding a set amount of fiber optic cables in one hand while inserting a cone between them. Next, a string is wrapped around the fibers to hold them against the cone while the length of the fibers are measured and cut. Since this is all done by hand, it is impossible for any two otoscopes to be manufactured identically. This proves to be an issue in fiber optic alignment to the otoscope.

The next otoscope examined is the Welych Allyn 3.5V Diagnostic otoscope shown in Fig. 19. Welych Allyn 3.5V Diagnostic Otoscope Head. This otoscope is manufactured from ABS plastic with a slot formed on its rear to house a glass viewing window. This design is less stable in several ways. First, its design is made of flat walled sides that are conducive to buckling under stress which may cause serious deformations, capable of affecting the holographic image. Second, the material is ABS plastic which has a modulus of elasticity of 2.3 GPa and a tensile strength of 40 MPa, nearly 20 times weaker than the stainless steel in the Heine Beta 200. Third, there is no area to fasten the otoscope to the package by means of a screw. The only option is a compression fit in the slot at the rear unless additional machining is performed. However, this would only further compromise the otoscope's structural integrity.



Fig. 19. Welych Allyn 3.5V Diagnostic Otoscope Head



Fig. 20. Exposed Diagnostic Otoscope Fiber Bundle

Although the Welych Allyn otoscope head has inferior package stability, its optical properties are far superior to the Heine Beta 200. Its fiber bundles can be seen in Fig. 20. Exposed Diagnostic Otoscope Fiber Bundle. The distribution of light intensity is uniform around its entire perimeter, providing the exact optical properties required for optimal holographic image quality. The distribution of light intensity is shown in Fig. 21. Welych Allyn Light Intensity Distribution. Thus, the Welych Allyn 3.5V Diagnostic otoscope is chosen for system integration.

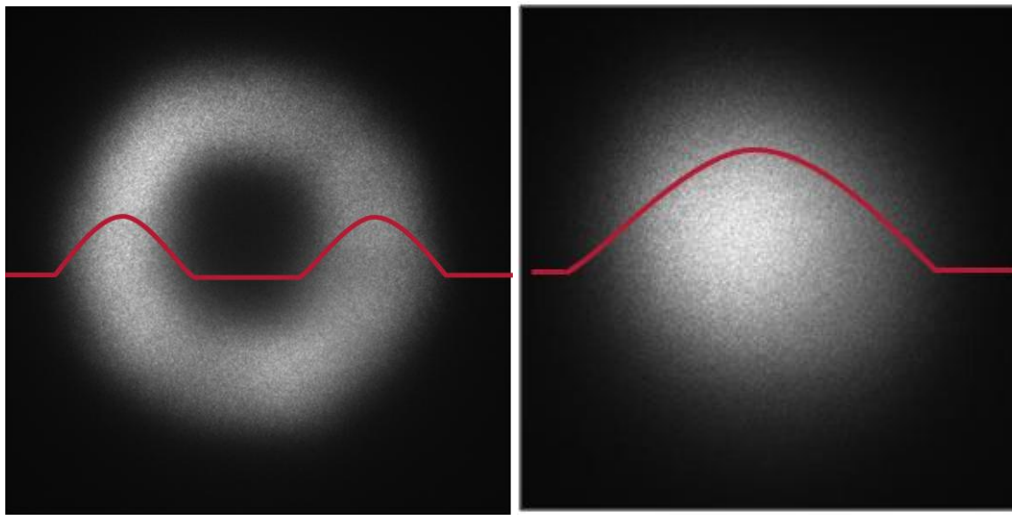


Fig. 21. Welych Allyn Light Intensity Distribution at (left) 1mm and (right) 15mm

An interesting development from the addition of the fiber optic otoscope to this system was the discovery that single mode fibers from the laser subsystem can be used in conjunction with the multimode fibers of the otoscope. This is possible because the multimode fibers are secured to the package so that there is no relative motion between the multimode and single mode fibers.

3.8 Stabilize Imaging Components

An important condition to maintaining the system's stability is to reduce the relative motion between the fiber optic cables carrying the reference and object beams. If one cable is repositioned relative to the other, the properties of the light are affected, causing the holographic image to blur significantly. Thus, the two cables must be securely fastened even while the package head is being repositioned. We recommend the use of Latex RD-407 to produce this result.

To protect the cables from hazard, they are enclosed in a flexible steel conduit leading from the case of the laser subsystem to the otoscope package. This latex compound can then be injected into the conduit at its shipped dilution concentration. Latex RD-407 is ideal for this use because of its flexible mechanical properties shown in Table 1. Mechanical Properties of RD-407 Latex.

Table 1. Mechanical Properties of RD-407 Latex

Mechanical Properties		
Quantity	Value	Unit
Young's modulus	1 - 5	MPa
Tensile strength	20 - 30	MPa
Elongation	750 - 850	%
Physical Properties		
Quantity	Value	Unit
Thermal expansion	6.7 - 6.7	e-6/K
Thermal conductivity	0.13 - 0.142	W/m.K
Specific heat	1880 - 1880	J/kg.K
Glass temperature	-70 - -70	°C
Service temperature	-50 - 85	°C
Density	910 - 930	kg/m ³
Resistivity	1e+21 - 1e+21	Ohm.mm ² /m
Dielectric loss factor	0.0016 - 0.005	

By injecting the RD-407 into the conduit, the cables solidify in the compound at a fixed position relative to each other. However, the motion of the conduit remains unrestrained because of its low modulus of elasticity. The latex is injected into the conduit and left to solidify for 48 hours. At the end of this period, curing is complete and the latex will be in its final form. The environment in which the latex cures should be dry and warm if possible to facilitate evaporation in the molding process. Flexibility of the material can be seen in Fig. 22. RD-407 Latex.



Fig. 22. RD-407 Latex

3.9. Attempt to Minimize Necessary DOF

One of the primary design constraints for the development of the otoscope package is the minimization of degrees of freedom. The general reasoning is that with less moving parts, the package is simpler, and thus easier to align, use, and maintain. However, a certain number of components still require a degree of adjustability in order to obtain the best image quality. For the first iteration of the package, the angle of deflection of the beam splitter cube was made adjustable. This gave the beam splitter 1 degree of freedom, as it would only be allowed to rotate about one axis. Once the optimal angle for the cube is attained, it is then permanently secured with epoxy. A device with 0 degrees of freedom would, in theory, require no maintenance or adjustment from the user. The doctor would be able to pick it up and use it whenever it was needed. By introducing moveable parts, they stand the risk of inadvertent motions, and misalignment may occur. Since it is the goal to design a clinical device, doctors are the main clientele. It is important to note that most doctors do not necessarily have the required training or time to realign the laser system if such a misalignment were to occur. Therefore, an on-call technician would be required to frequently maintain the system.

A secondary concern is the necessity of lubrication. When two surfaces rub, they experience deteriorative frictional forces that could eventually ruin their tightly toleranced interface. The addition of lubrication creates other issues such as the necessity for periodic servicing. This adds another responsibility for the user that has potential for neglect. If the lubrication cavities were prone to leaking or if the areas were close to optical components, there is a chance that the fluid may come in contact with the optics. If this were to happen, the picture quality would be greatly affected, if not ruined. By removing the degrees of freedom of the

system, there is no need for lubrication. The system would require less maintenance and upkeep and prolong the duration of the otoscope's usability.

4. Design of the Package

To best miniaturize the otoscope assembly, all optical components must connect to one another in a singular package. By attaching them in this manner, there are no relative motions between components and the tightly toleranced distances and angles will be maintained while the package is handled by the doctor. The following section will detail how the first iteration of the otoscope package is designed and how the components interlock to form a stable handheld device. Fig. 23. First Package Iteration with Top (left) Off and (right) On gives an overview of the package as a whole with the top off and on.

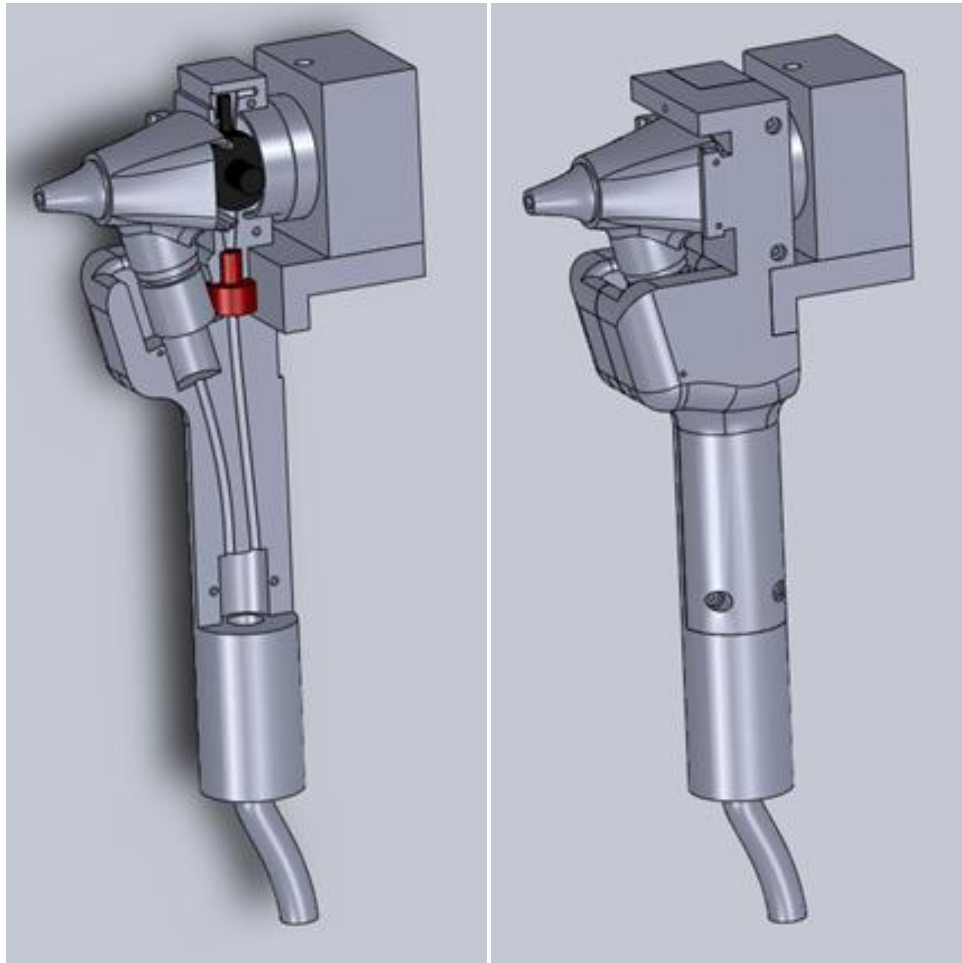


Fig. 23. First Package Iteration with Top (left) Off and (right) On

All components are attached to a central piece that is split into a top and bottom half allowing for easy insertion of components. The bottom protruding handle offers a level of ergonomic comfort and to allow for manual doctor operation. However, as handheld manipulation was not a priority, consideration was given to possible attachment points for a kinematic arm. Such a device would aid in the stable locating and restraining of the package at a location suitable for taking TM measurements. Flat surfaces were designed on the sides and back faces of the package, including the camera shelf, to provide options for the secure placement of the arm, pending its final design. To ensure the top and bottom halves align, the package was designed to use 1/16 inch spring pins at key locations. This guarantees symmetry by negating the undesirable effects a divided package has on fit and tolerances. The halves are otherwise fastened to each other through the use of standard 4-40 bolts, and threaded inserts as the anchor points in the bottom half of the device.

The otoscope head connects to the package through use of its lens holding feature. The manufacturer includes a magnifying lens that can be inserted into the back face by sliding it between two retaining arms. The interference fit that holds the lens in place was determined to be of sufficient strength to also hold the otoscope head to the package shown in Fig. 24. Otoscope Head Attachment Rail. To make use of this feature, a receiver was designed into the package that would slide into the lens slot, creating a similar interference restraint. Railings were extruded on the sides of the receiver to help align the head, ensuring that the camera is axially aligned with the otoscope speculum. A metal sleeve is introduced at the throat of the otoscope to prevent the introduction of ambient lighting into the fiber bundle. The object beam is also routed through this retaining cup.

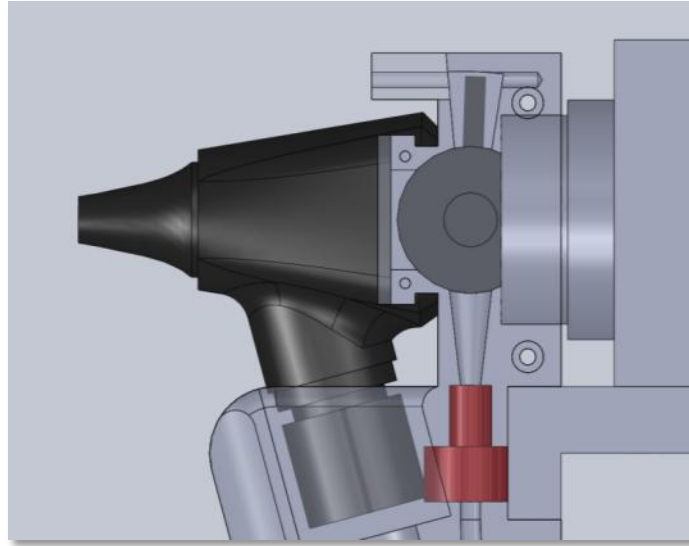


Fig. 24. Otoscope Head Attachment Rail

To position and hold the camera at an appropriate level to receive the reference and reflected object beams, a shelf protrudes from the rear of the package. The camera is interfaced to this shelf by a bolt that secures the shelf linearly. To prevent the camera from rotating on the bolt, as well as to help in keeping the camera aligned along the visual axis of the device, a half threaded ring connects the eyepiece of the camera to a circular channel in the backside of the package.

Next, consideration was given to the beam splitter cube. The beam splitter cube directs both the reference beam and the object beam, after being reflected off the sample, into the camera. It is for this reason that it is essential that the beam splitter is properly aligned and centered with respect to the camera and the otoscope viewing aperture. Due to manufacturing tolerances, it was decided that the beam splitter cube should be on a rotary stage. This introduced two complications in the design: the method of rotating, and how to hold the stage at the desired angle. To keep the design simple, an axle design was decided upon, with the cube sitting in a

cylindrical housing able to pivot on two pins within the OEHO package. On the top of the housing is a cantilever beam that is used to rotate the beam splitter around the pins when the package is closed shown in Fig. 25. (left) Beamsplitter Cube Stage (right) Method of Rotation. The beam is moved through use of a set screw which is accessed through a hole above the otoscope head. The housing is held in place by a recessed spring that keeps the beam tight against the set screw. After installation and completion of the package, the optimal angle was found to be nearly parallel to the base through qualitative comparisons of image quality and brightness.

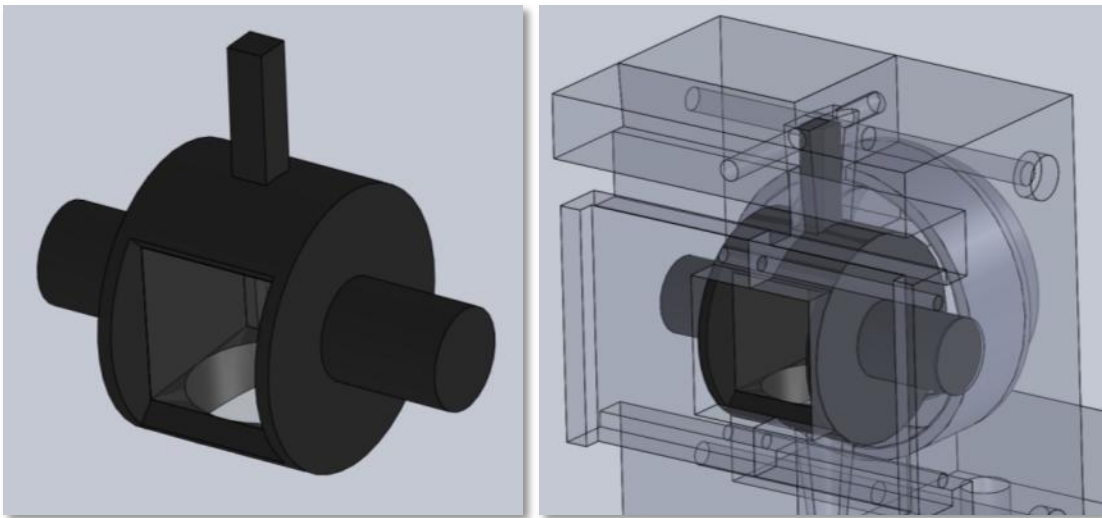


Fig. 25. (left) Beamsplitter Cube Stage (right) Method of Rotation

The conduit, carrying the two fiber patch cords, is inserted into the bottom of the handle and held with set screws. From there, the two fibers split and follow their respective paths toward the otoscope head and beam splitter cube. The tips are both inserted into collars, colored red in the full package solid model, which isolate their movement and position the ends of the fibers at their desired locations. The reference beam is held in place so the distance between the tip of the beam and the center of the reflecting beam splitter surface is 24.84mm to account for the

numerical aperture of the fiber. This corresponds to the optimal length of travel before interacting with the reflector. The collar is designed to fit securely inside the metal sleeve of the Welch Allyn otoscope head so that the tip of the fiber is as close as possible to the illumination surface of the interior fiber bundle. This can be seen in Fig. 26. (left) Fiber Collar (Section View) (right) Internal View of Collars.

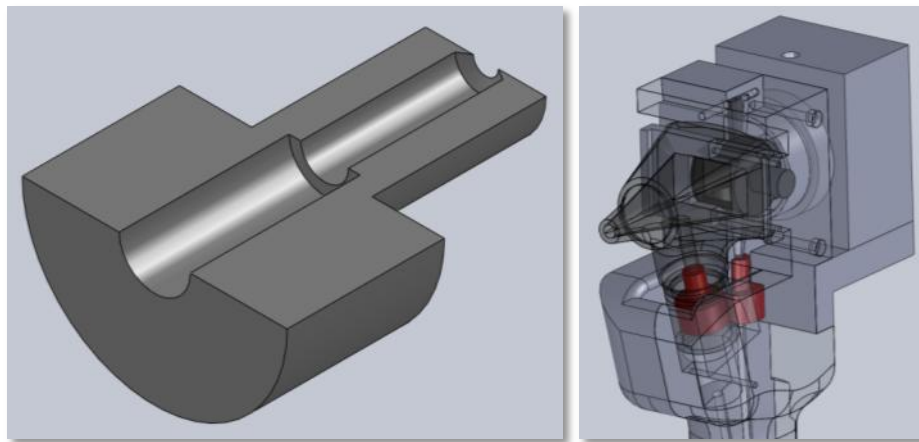


Fig. 26. (left) Fiber Collar (Section View) (right) Internal View of Collars

By incorporating all the components into a singular module in this manner, the overall number of degrees of freedom in the system is greatly reduced. The package has only 7 degrees of freedom: the 6 possible translations and rotations of the device as a whole as well as the single axis internal rotational capability of the beam splitter stage. The unit is an all inclusive design with the goal to bring all necessary components together to work as one. This is demonstrated in Fig. 27 which shows a cut-away view of the package to demonstrate how the illumination travels through the system.

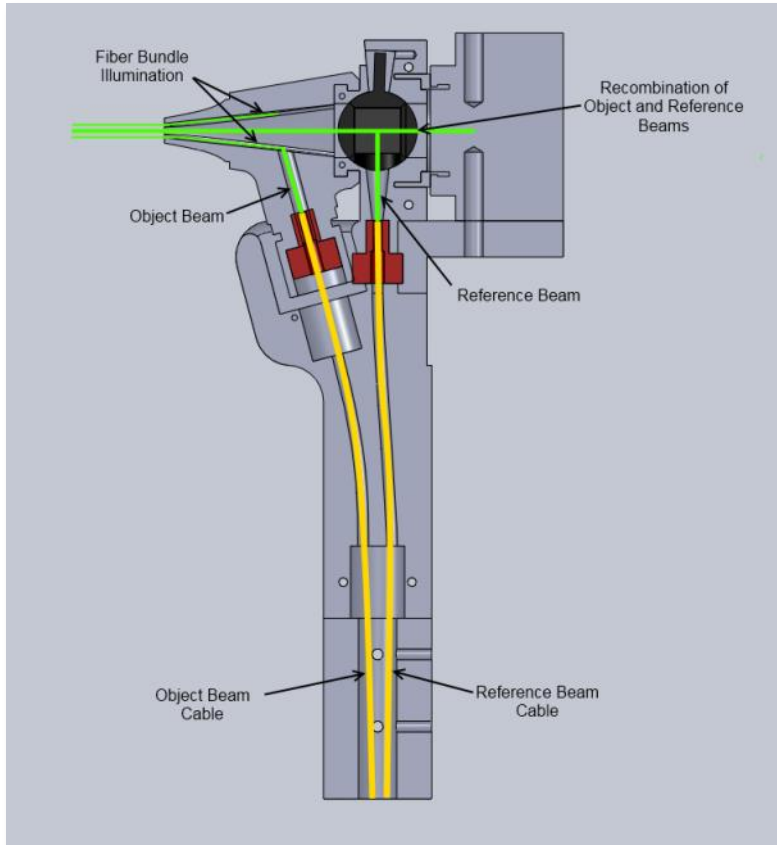


Fig. 27. Internal Components of Iteration 1

5. Fabrication of Prototype

To validate and characterize the design described in the section above, it is necessary to have a manufactured version of the package for testing. Since multiple iterations of the design were planned for optimization purposes, traditional machining processes would be both too costly and time consuming. It was for this reason that rapid prototyping was decided upon as the optimal method for creating a physical version of the first design iteration.

3D printing of the package was done using the Stratasys Dimension FDM Rapid Prototyping Machine in Higgins Laboratories. The Stratasys machine uses stereolithography technology to print the package on a layer basis out of ABS plastic. This method of material deposition allows for the manufacturing of complex shapes such as contoured inner surfaces which would otherwise be time consuming and costly to machine using traditional means.

Although there are expanded capabilities with the process of stereolithography in regards to geometries and time of manufacturing, the trade off is with resolution and material choice. The only material available for prototyping in this manner is ABS plastic which has variable density in the final piece due to resolution, part size, and printing orientation. The other main issue, resolution, is due to the physical tolerance capabilities of the machine, $\pm 0.25\text{mm}$, and the quality of the processed CAD STL output. Since STL files use numerous triangles to approximate three dimensional shapes, the processed image's smoothness and clarity is directly related to the mesh size used to represent edges and surfaces.

With minimal fit issues, the first design iteration was prototyped as shown in Fig. 28. Rapid Prototype - Iteration 1 (left) bottom (right) top and Fig. 29. Assembled and Illuminated

Prototype Slight modifications were done with a hand operated Dremel tool to correct for tolerance errors.

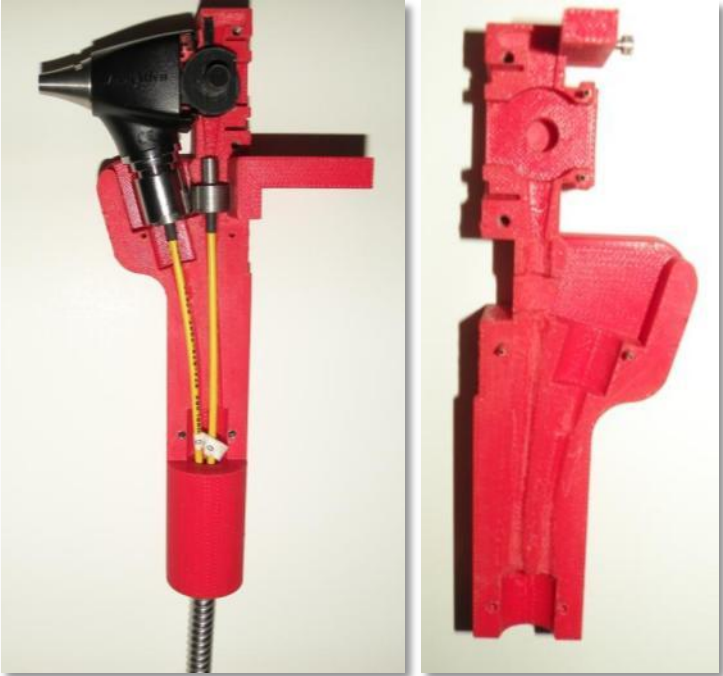


Fig. 28. Rapid Prototype - Iteration 1 (left) bottom (right) top



Fig. 29. Assembled and Illuminated Prototype

6. Characterization of Optical Performance

Upon completion of the otoscope package, a thorough analysis of the optical performance was executed. It is necessary to quantify improvements over prior generations of the otoscope head to ensure the success of the developments. The procedure for characterizing the package involved finding the field of view, magnification, resolution, depth of field, and aberration of the holographic images produced.

6.1. Field of View

The first parameter analyzed was the field of view. Because the human tympanic membrane is approximately 10 mm in diameter, this defines the required field of view. To determine the distance the object must be from the optical system to allow a 10mm by 10mm region to be captured, a target consisting of vertical white and black lines at a frequency of two lines per millimeter was used. At a working distance of 15mm, ten line pairs fit within the field of view. The working distance for the previous generation otoscope head for an equivalent field of view was approximately 13mm. This is sufficient because the distance from the tip of the otoscope to the tympanic membrane is coincidentally 15mm. Fig. 30. Field of View and Magnification of Image compares an image of the target used to determine the field of view at the working distance to an image of the same target, scaled to the actual size.

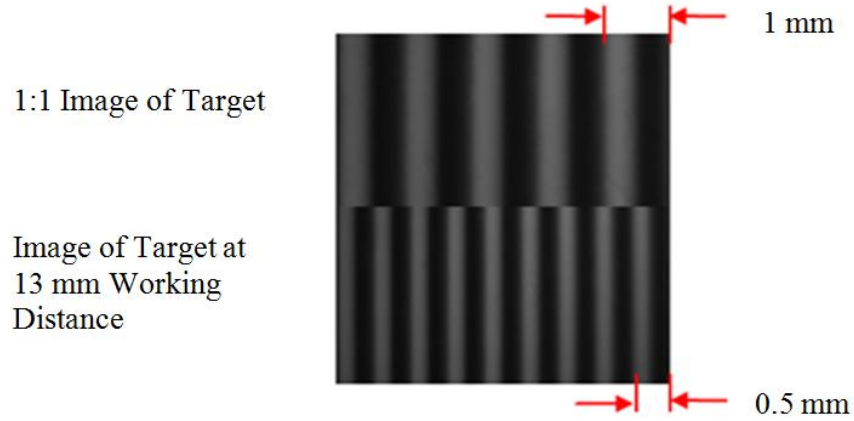


Fig. 30. Field of View and Magnification of Image

6.2. Magnification

The magnification shown in Fig. 30. Field of View and Magnification of Image above is approximately 0.5, this can be calculated from the geometry of the system. The CMOS chip used has dimensions of 1280 x 1024 pixels. Each pixel is a square with edge length of $6.7\mu\text{m}$. The size of the region of interest on the camera being used is 800 x 800 pixels. At a 15mm working distance, a 10mm fit can be calculated by finding the ratio of the length of 800 pixels on the CMOS chip to the actual length of the region being imaged:

$$M = \frac{\left(\frac{800 \text{ pixels}}{1280 \text{ pixels}} \right) \cdot \left(1280 \text{ pixels} \cdot \frac{6.7 \times 10^{-3} \text{ mm}}{1 \text{ pixel}} \right)}{10 \text{ mm}} = 0.536 \quad (6.1)$$

This means that a 10mm by 10mm region of the object is being imaged on a 5.36mm by 5.36mm region of the CMOS chip.

6.3. Resolution

The resolution was determined using a 1951 United States Air Force resolution target shown in Fig. 31. 1951 USAF Spatial Resolution Test Card. The target is comprised of groups of white and black line pairs at various frequencies. The resolution of an imaging system is determined by the visibility of the smallest line pair frequency that the system is able to resolve. The system's ability to resolve a line pair is determined by how well the system can maintain contrast between the white and black regions of that line pair. This is accomplished by implementing image analysis algorithms in computer software capable of pixel-to-pixel contrast comparisons. Because a pixel-to-pixel intensity comparison is used to determine the contrast with the digital holography calculations, uniform object illumination is necessary.

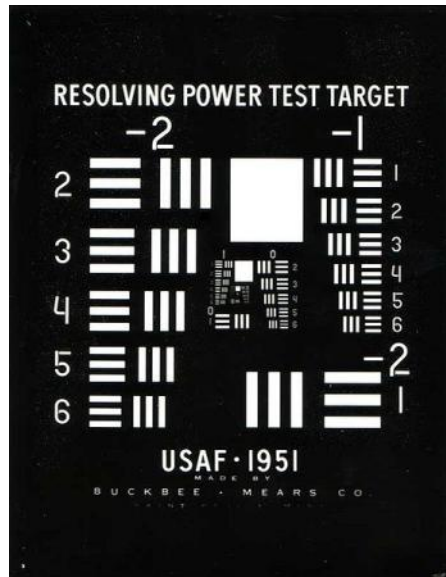


Fig. 31. 1951 USAF Spatial Resolution Test Card

Table 2. 1951 USAF Spatial Resolution Spreadsheet

Number of Line Pairs / mm in USAF Resolving Power Test Target 1951												
Group Number												
Element	-2	-1	0	1	2	3	4	5	6	7	8	9
1	0.250	0.500	1.00	2.00	4.00	8.00	16.00	32.0	64.0	128.0	256.0	512.0
2	0.280	0.561	1.12	2.24	4.49	8.98	17.95	36.0	71.8	144.0	287.0	575.0
3	0.315	0.630	1.26	2.52	5.04	10.10	20.16	40.3	80.6	161.0	323.0	645.0
4	0.353	0.707	1.41	2.83	5.66	11.30	22.62	45.3	90.5	181.0	362.0	-----
5	0.397	0.793	1.59	3.17	6.35	12.70	25.39	50.8	102.0	203.0	406.0	-----
6	0.445	0.891	1.78	3.56	7.13	14.30	28.50	57.0	114.0	228.0	456.0	-----

Fig. 32. 1951 USAF Holographic Image Test is an image taken with the miniaturized otoscope head.

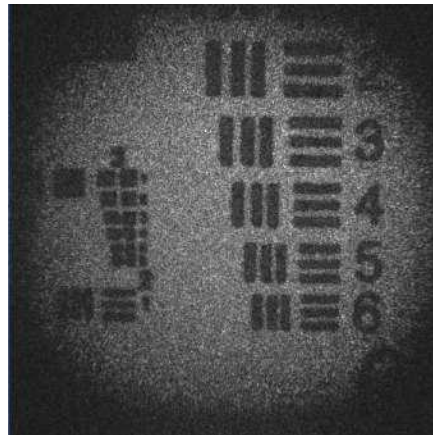


Fig. 32. 1951 USAF Holographic Image Test

Using LaserView, a contrast trace was performed across all of the line pair elements on the target. At the 15mm working distance, the otoscope head is able to resolve element 2 of group 3. This correlates to a line pair per millimeter resolution of 8.98.

6.4. Depth of Field

The depth of field of the otoscope package was characterized by experimental methods using a 45 degree wedge target. The target has horizontal lines spaced at known intervals corresponding to a distance parallel to the optical axis. A contrast trace can be performed on the

image of the target. The point where the contrast drops below a certain percentage of the maximum contrast is said to be beyond the depth of field.



Fig. 33. Sample Depth of Field Setup

The target is positioned at approximately 15mm away from the tip of the otoscope as shown in Fig. 33. Sample Depth of Field Setup. The depth of field target has multiple groups of line pair frequencies; to perform the characterization of the miniaturized otoscope head the five line pair per millimeter group was used. Fig. 34. Depth of Field Test is a graph generated from the contrast trace of the imaged used to characterize the depth of field.

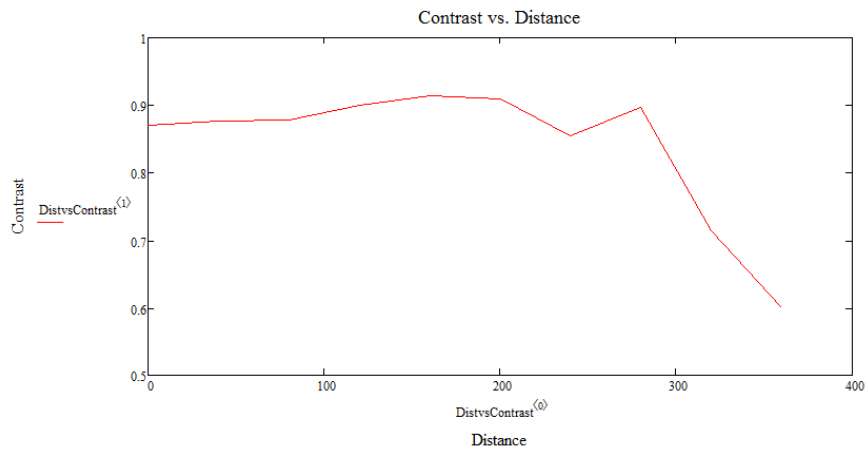


Fig. 34. Depth of Field Test

7. Characterization of Mechanical Properties

7.1. Finite Element Analysis

A critical element of the package stability is the amount of deformation that may occur under normal operating conditions. Fortunately, this system will endure relatively low amounts of stress because of the hospitable environment in which it is used. There is no severe stress or cyclic loading that the package must support because there will be no components added or removed from the device, and there are no moving mechanical components. The only disturbances that may arise are from repositioning the system and acoustic excitation on the package shell meant to stimulate the tympanic membrane. Thus, modal analysis is essential in determining effects of an acoustic subsystem to the outcome of the holographic image quality. Ideally, high fundamental natural frequencies and minimal deformations are desirable.

7.1.1. Vibrations in Shell-Type Structures

A frequent problem encountered in engineering is minimizing the weight and size of a system while still ensuring its structural integrity. When the weight of the system is minimized and its strength is maximized, large amplitudes of vibration occur. According to the linear theory of vibration, natural frequencies and mode shapes are independent of the amplitude of vibration. However, if the amplitude of vibration is large, non-linear effects result.

A first step in performing finite element analysis requires the development of a mesh so that individual nodes may be analyzed. This is commonly done through the use of numerous triangles where each node is interconnected to adjacent nodes. This enables the forces and deformations to be analyzed at a single point and translated to concurrent points until steady-state conditions are reached (M. Amabili and R. Garziera).

One of the most widely used simplifications for developing equations for the vibration of shells are the Donnell-Musthtari-Vlasov Equations. The basic assumption is that in-plane deflections can be neglected in the bending strain expression but not in membrane strain expressions. This results in bending strain equations:

$$k_{11} = -\frac{1}{A_1} \frac{\partial}{\partial \alpha_1} \left(\frac{1}{A_1} \frac{\partial u_3}{\partial \alpha_1} \right) - \frac{1}{A_1 A_2^2} \frac{\partial u_3}{\partial \alpha_2} \frac{\partial A_1}{\partial \alpha_2} \quad (7.1)$$

$$k_{22} = -\frac{1}{A_2} \frac{\partial}{\partial \alpha_2} \left(\frac{1}{A_2} \frac{\partial u_3}{\partial \alpha_2} \right) - \frac{1}{A_2 A_1^2} \frac{\partial u_3}{\partial \alpha_1} \frac{\partial A_2}{\partial \alpha_1} \quad (7.2)$$

$$k_{12} = -\frac{A_2}{A_1} \frac{\partial}{\partial \alpha_1} \left(\frac{1}{A_2^2} \frac{\partial u_3}{\partial \alpha_2} \right) - \frac{A_1}{A_2} \frac{\partial}{\partial \alpha_2} \left(\frac{1}{A_1^2} \frac{\partial u_3}{\partial \alpha_1} \right) \quad (7.3)$$

The main concept allowing for this simplification is that the shell is thin to the point that it deforms as one solid plane. This is acceptable for our application because loads on the system are not nearly enough to cause substantial planar deformation.

Assuming normal loading, corresponding equations of motion are:

$$\frac{\partial (A_2 N_{11})}{\partial \alpha_1} + \frac{\partial (A_1 N_{12})}{\partial \alpha_2} + \frac{\partial A_1}{\partial \alpha_2} N_{12} - \frac{\partial A_2}{\partial \alpha_1} N_{22} = 0 \quad (7.4)$$

$$\frac{\partial (A_2 N_{12})}{\partial \alpha_1} + \frac{\partial (A_1 N_{22})}{\partial \alpha_2} + \frac{\partial A_2}{\partial \alpha_1} N_{12} - \frac{\partial A_1}{\partial \alpha_2} N_{11} = 0 \quad (7.5)$$

$$D \nabla^4 u_3 + \frac{N_{11}}{R_1} + \frac{N_{22}}{R_2} + \rho h \frac{\partial^2 u_3}{\partial t^2} = q_3 \quad (7.6)$$

A simplified characteristic equation can be developed by simplifications done in references (E. Ventsel and T. Krauthammer):

$$D \left(\frac{n}{a} \right)^8 + \frac{Eh}{a^2} \left(\frac{\lambda}{L} \right)^4 - \rho h \omega^2 \left(\frac{n}{a} \right)^4 = 0 \quad (7.7)$$

This gives:

$$\lambda_i = \frac{nL}{a} \sqrt[4]{\frac{a^2}{Eh} \left[\rho h \omega^2 - D \left(\frac{n}{a} \right)^4 \right]} \quad (7.8)$$

Where λ_i is the root, D is the bending stiffness, ω is frequency, E is modulus of elasticity, n is the mode, and the remaining parameters are based on the shape of the object. The fundamental natural frequencies can then be found for real answers for λ_i . An example of a very basic analysis of a disk can be found in Appendix A under Mathcad14 Analysis.

7.1.2. ANSYS Analysis

ANSYS was able to determine these complicated calculations in less than six hours for the otoscope package. A mesh was created and a fixed constraint was placed on the handle of the otoscope. The resulting fundamental natural frequencies were found:

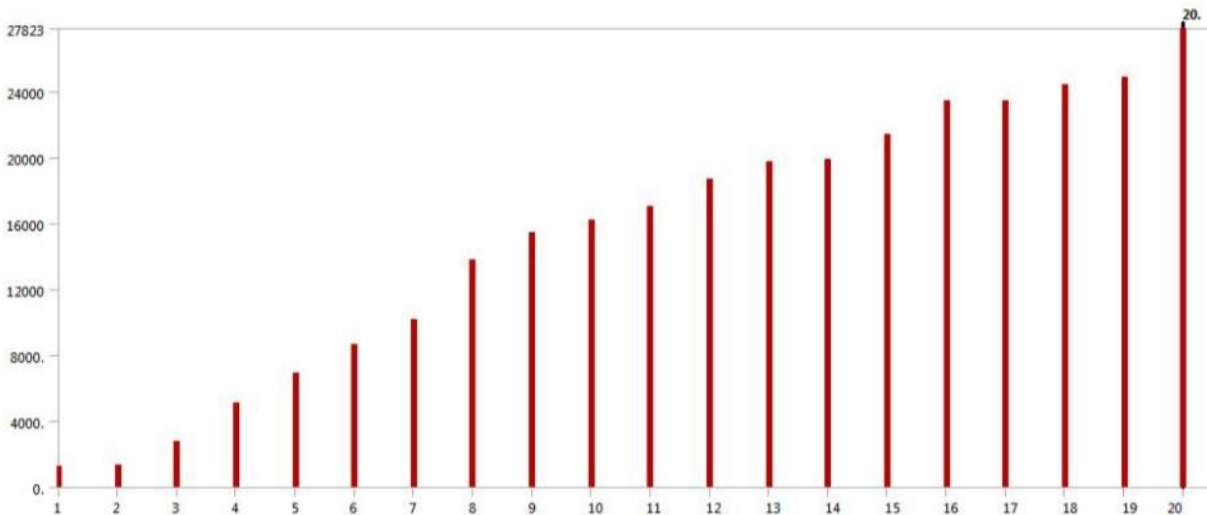


Fig. 35. First 20 FNF for Iteration 1

Table 3. ANSYS: First 20 FNF for Iteration 1

	Mode	Frequency [Hz]
1	1.	1258.6
2	2.	1369.4
3	3.	2789.8
4	4.	5159.2
5	5.	6939.7
6	6.	8638.9
7	7.	10148
8	8.	13808
9	9.	15474
10	10.	16225
11	11.	17005
12	12.	18735
13	13.	19734
14	14.	19898
15	15.	21384
16	16.	23417
17	17.	23452
18	18.	24461
19	19.	24888
20	20.	27823

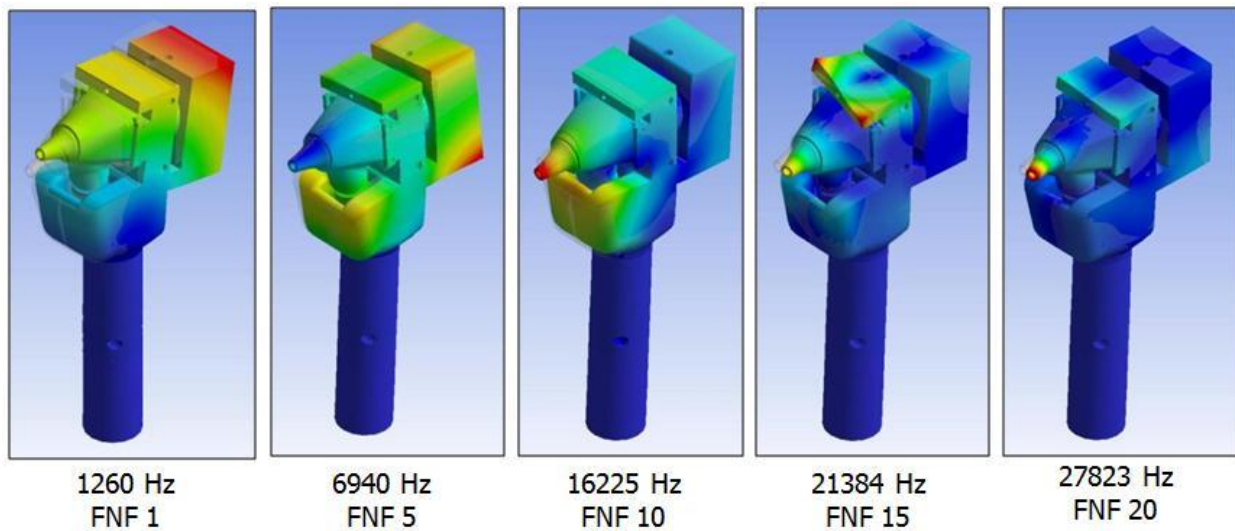


Fig. 36. ANSYS: Fundamental Natural Frequencies of Vibration

The relationship between the modes of vibration follows a nearly linear growth curve, allowing higher frequencies to be estimated fairly accurately. In addition, a static structural analysis was conducted to determine the maximum areas of deformation and stress. Results can be seen in Fig. 37. ANSYS: Total Deformation.

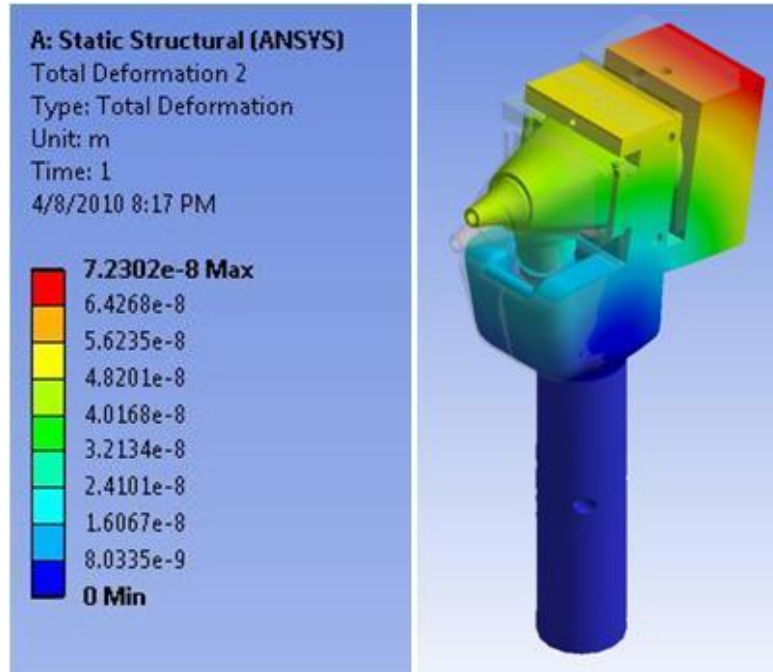


Fig. 37. ANSYS: Total Deformation

A maximum deformation of 72.3 nanometers is achieved at the top of the camera case. This is a significant deformation considering that the measurements being taken are of the sub-nanometer scale. However, it has relatively no effect on the quality of the holographic image because it is a static deformation, so the relative motion between all components is zero. On the other hand, vibrations caused at the fundamental natural frequencies of the system that reach magnitudes greater than this value would cause the reconstructed holographic image to be blurred and distorted. A stress analysis of the package under static loading from the weights of

the various components on the structure and the effects of gravity was also gathered through ANSYS. The resulting stresses are shown in Fig. 38. ANSYS: Equivalent Stress. This figure demonstrates that the greatest stress occurs at the joint of the handle to the otoscope head assembly. The maximum stress is only 1.27×10^5 Pa, or 1.25 times atmospheric pressure. Considering that this analysis was done with stainless steel, regular cyclic loading of this stress on the part would not cause plastic deformation or fatigue on the part. Therefore, there is lifetime expectancy under normal conditions.

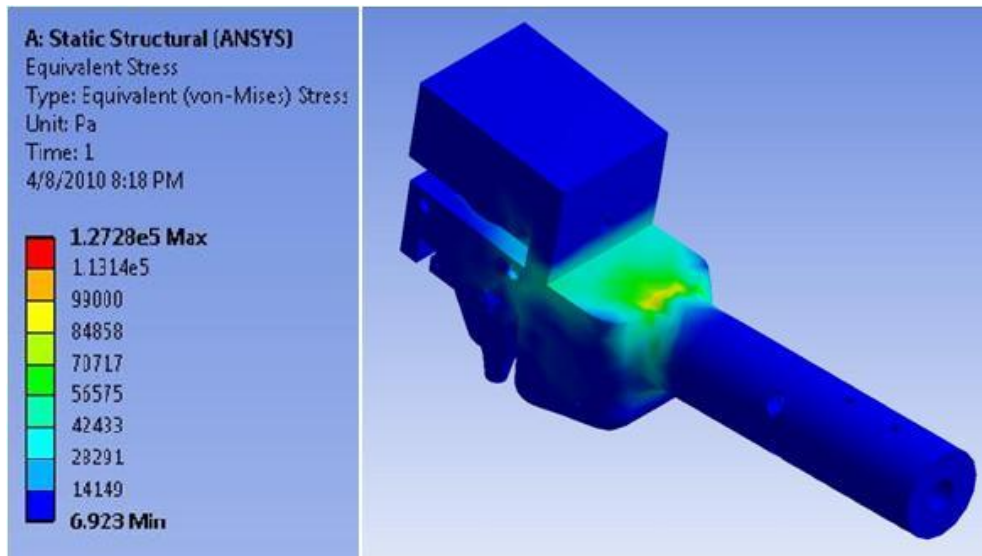


Fig. 38. ANSYS: Equivalent Stress

The result of this analysis is essential in the future development of the system. An acoustic subsystem is being developed to be attached to the speculum of the otoscope head along with a position arm for holding the system. Although a package with a first mode of vibration above 20 kHz, to avoid disturbance from background noise, was unable to be produced in the first package iteration, new materials should be tested that have better damping and insulation qualities. However, it was found to be difficult to get a package of this size to reach a minimum natural frequency of 20 kHz. The implication is that the positioning arm and acoustic subsystem

should be designed around the parameters of the first 20 fundamental natural frequencies of vibration of the package. During clinical use, sound waves should not be broadcast at a frequency that might cause the system to reverberate at one of its modes. Also, the speed of the positioning arm and rate of deceleration should be calculated to determine the necessary time required for the package to stabilize once stopped. Following these guidelines would ensure reliable testing conditions.

7.1.3. Iteration Modifications

Upon completion of characterizing the first iteration of the otoscope package, there were several areas of modification that needed attention. First, the dimensions of alignment of the object beam varied between each otoscope head. It is impossible to create a system with zero degrees of freedom for fiber alignment in the package head which accounts for variation in Welych Allyn 3.5V Diagnostic otoscopes. A method of aligning the object beam with the otoscope head with at least two axes of rotation is necessary to allow for global manufacturing. A more robust system package must be designed to achieve a higher fundamental natural frequency. Background noise that might affect the stability of the system at the MEEI is expected to range from 0 – 20,000 Hz in frequency. Therefore, methods must be investigated that might raise the lowest mode of vibration to the upper limit of our design range. For example, eliminating excessively large cavities, rounding flat faces, and eliminating potential moment arms would increase the fundamental natural frequencies. Experiments while aligning the system resulted in the conclusion that the adjustment on the beam splitter cube is not required for alignment. Any vertical misalignment of the image could be corrected by adjusting the new stage on the object beam. Also, the method of attaching the package to the positioning system

must be modified. More convenient ergonomic handles could be incorporated into the device to allow for greater stability when attached to the positioning arm as well as greater user comfort.

7.2. Second Iteration

One of the main drawbacks to the ergonomic handle design of the first iteration was that it acted as a moment arm and added an unnecessary instability to the system. As was seen in the FEA analysis, the largest stresses were located at the extremes of the package due to its slenderness and length. Since it was planned that the device would be controlled by a kinematic arm and not handheld while in use at the clinic, it was decided that to reduce the potential forces and FNF, the handle would be shortened and brought closer to the main body. Another key change to the first iteration is the removal of the rotational beam splitter stage. It was determined that the angle of the beam splitter cube was optimal when it was lying parallel to the base of the package. This allowed for the removal of the rotating stage and further simplified the design. At this stage, the design was tested using ANSYS for FNF and stresses. The results are included in the digital appendix and show that the fundamental natural frequencies are increased. Fig. 39 shows the tested CAD models and comprises the second iteration of the package design.

Although the level of system adjustability was decreased with the removal of the beam splitter cube stage, an object beam positioner was decided upon to test whether or not the angle of incidence had any effect on the quality of the reflected hologram. The position decided upon is Thorlabs Compact Kinematic Mount, KMSS. The mount allows an angular displacement range of $\pm 4^\circ$.

This iteration was not prototyped since a third generation was planned to address certain other issues that still existed with the OEHO device in its current state.

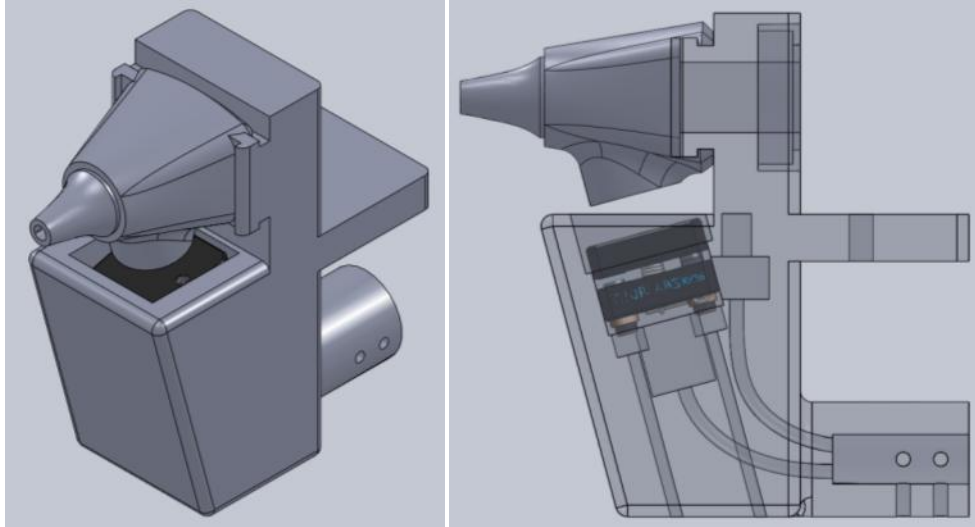


Fig. 39. 2nd Iteration (left) Solid Isometric View (right) Transparent Side View

7.3. Third Iteration

The third and final iteration was designed to address all the potential issues that were discovered from testing the first iteration as well as the FEA of the second iteration. During the characterization of the first iteration, a substantial amount of noise was apparent in the computer output. It was determined that the cause of the disruptions was due to the camera cable that protruded from the back of the package. The cable, being long and rigid in nature, was transmitting the vibrations from the table and surrounding equipment to the camera. Instead of connecting to the outer case, the serial cable connected directly into the chip on which the video acquisition equipment was located. Without the added stability of a case connection, wide variations in picture quality were observed due to the noise in the room. To correct for this problem during testing, a post was setup behind the camera to hold the camera cable, providing a further level of vibration damping and displacing the cable from the table. To prevent this from being an issue in the third iteration, a cable stabilizing feature was designed for the back of the package to hold both the data and power lines.

To address the image quality issues that were determined to be the result of movement between the fiber optic cables, polarizing maintaining (PM) fibers were used in this design. Commonly used in interferometry for laser delivery, polarizing maintaining fibers preserve the polarization of the input light source and reduce the negative effects that bending and moving the fiber optic cables can cause. The slightly more bulky and longer PM fiber connectors required more clearance space in the handle causing the package to be taller than the second iteration.

In an effort to use standard parts in this design, the previously machined fiber connectors were replaced by Thorlabs FC connectors. The reference beam is secured at a distance of 24.84mm by a Thorlabs ADAFC3 FC to FC mating sleeve fastened to the packages interior. The object beam is connected with an ADAFC SMA1 FC Mating Adapter to the KMSS Kinematic Mount that has been modified to accept the adapter.

The kinematic mount is fastened to a machined connector plate that is secured to the bottom of an otoscope with the metallic sleeve removed. By removing the metal sleeve, the distance between the otoscope's fiber bundle and the tip of the PM fiber can be better controlled. The fiber is held at a distance of 15mm for optimal light distribution.

Due to these additions, the package is bulkier than previous versions. The extra mass is desirable from a mechanical standpoint as it makes the system more stable and serves to increase the fundamental natural frequencies. For this reason, the bulk was not attempted to be minimized. The upright connection between the conduit channel and camera support structure was added for supplemental mass as well as to act as an attachment point for the kinematic arm assembly.

The third version of the package was rapid prototyped in the same manner as the first, however, no testing was able to be completed for this project. Likewise, a finite element analysis was done in ANSYS and is provided in the digital appendix.

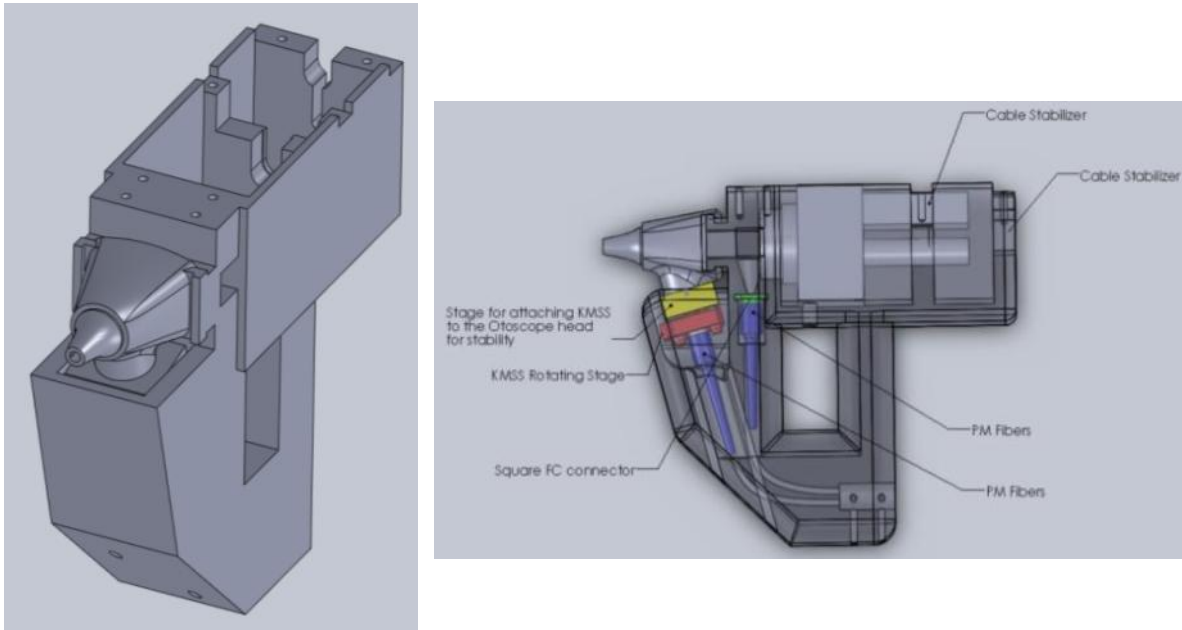


Fig. 40. Iteration 3 Package Design (left) Isometric View (right) Transparent Side View

7.4 Acoustics Interface

As previously described, it is essential to deliver an acoustic stimulus to the TM to incite surface motion for deformation measurements. In conjunction with MS candidate Nikhil Bapat (N Bapat), an acoustic delivery system was designed to interface with the Welch Allyn otoscope head for the third iteration configuration. To be included with the design was a speaker for sound delivery as well as a microphone for audio recognition. Fig. 41. Acoustic System (left) Transparent Top Shell (right) Assembled on Second Iteration is the preliminary design for the acoustic system as was completed with MS candidate Nikhil Bapat.

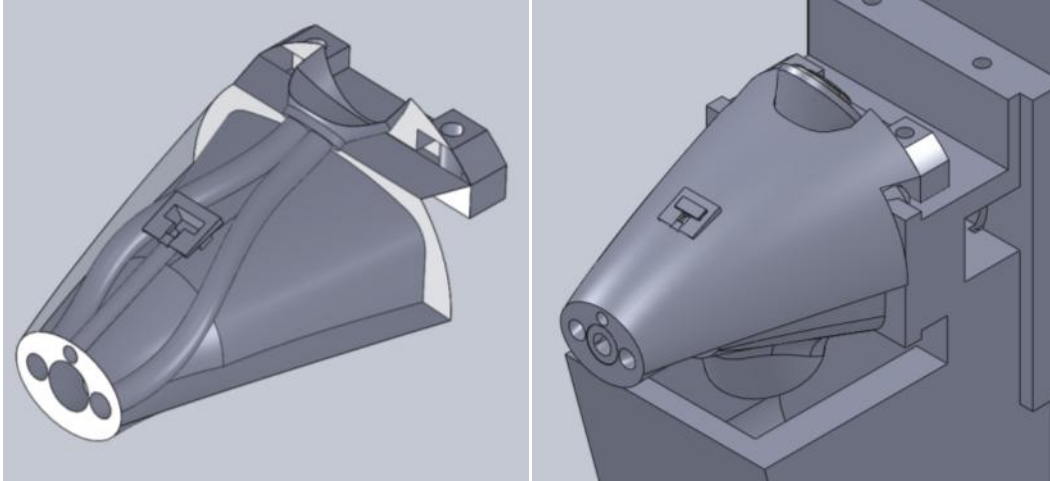


Fig. 41. Acoustic System (left) Transparent Top Shell (right) Assembled on Second Iteration

Two speaker tubes extend through the lofted shell from the speaker interface to the speculum connection. These channels are used to deliver the desired audio signal to the TM. Multiple channels were chosen in order to output a more inclusive signal across the entire membrane's surface. Using COMSOL software, a fluid analysis was completed to validate the sound propagation through the planned speaker tube geometry. The speaker holding cone connects to the receiver on the top and secures the device to the package. The 30° cone directs the sound waves from the speaker to the two-way split where the signals enter the sound delivery tubes. The microphone is held in place in a slot in the top of the lofted shell with a microphone input tube running straight through to the otoscope tip directed towards the sample. The shell itself is aligned and secured to the package in three ways. First, the tip of the apparatus is designed to fit snugly around the tip of the otoscope. This ensures axial alignment of the sound delivery with the laser illumination toward the sample of interest. Second, the inside of the shell is formed so that it follows the curvature of the otoscope casing. The inner walls will enfold the otoscope forcing the acoustic device to be laterally aligned. Lastly, a flange is incorporated into

the design so that it can be securely fastened to the package and relative motion between the two can be minimized.

8. Otoscope Package Results

8.1. External Shape

8.1.1. Ergonomic Comfort

As described earlier in the methodology section, the first iteration design was created in a manner to facilitate both handheld operation as well as connectivity to a kinematic arm. The handle, in combination with the filleted edges for safety, make it possible to easily and comfortably control the motions of the head.

In any design, it is important to take into account the needs of the consumer. A particular design might be mechanically perfect; however, if it is unwieldy or alien to the end user, it will not be welcomed and used. The learning curve of using a new device effectively can be greatly minimized by making it operationally familiar. A benefit to the prototyped OEHO is its familiarity in the hands of anyone who has previously used an otoscope.



Fig. 42. (left) Conventional Otoscope (right) OEHO Prototype

8.1.2. Easy interfacing with positioning arm

Although the ability for a doctor to manipulate the device was an important consideration, it was the ultimate goal to have the OEHO be controlled and stabilized with a kinematic arm. Ph.D candidate Ivo Dobrev's proposed kinematic arm is a combination of beams and magnetic brakes. Essentially, three beams are interconnected with shafts and are secured to a stabilized base. On each beam joint is a magnetic braking system that, when activated, restrains the motion of each beam in relation to the ones to which it is connected. The doctor would be able to freely move the de-energized device to a suitable location for viewing the patients TM, and when satisfied, could energize the brakes to lock the arm rigidly in place. By implementing a passive braking system, the strength of the holding power could be controlled and fine tuning could be done through varying the resistance of the arm's motion.

The proposed method of connecting the kinematic arm to the body of the package is through use of a Bogen Monfrotto Grip Action Ball Head, Fig. 43. This and similar devices are used in the fields of photography and film making where high levels of precision and stability are necessary. This joint allows dexterous control over the connection between any two attached components. Rotation about all three axes is allowed, permitting adjustments in yaw, pitch and roll. This model is particularly desirable due to its ability to set the resistance of movement to allow for fine tuning. After the position is set, the device can be locked and made immobile while the OEHO measurement is taken. Upon completion of the 2010 OEHO MQP, the kinematic arm was in the preliminary construction and synthesis phase.



Fig. 43. Bogen Monfrotto Grip Action Ball Head

9. Conclusions and Recommendations

9.1. Otoscope Head

A key issue encountered with otoscope heads from all suppliers is that they are not designed for our application of the product. Medical otoscopes are designed to be used with a LED light source and viewed with the naked eye. Thus, very little precision is required to produce a part that allows for sufficient viewing clarity. This has a severe effect on the otoscope's effectiveness and precision in delivering a consistent and reliable image when integrating the otoscope with the collection of holographic imagery on the sub-nanometer scale. The quality control of the otoscopes is too poor to produce fiber optic bundles of the same diameter, polish, and distribution from model to model. A direct impact from this is that the object beam must be custom aligned for every different otoscope used. Manufacturing is therefore complicated because degrees of freedom are necessary at the junction of the object beam and the otoscope head, and professional technicians would be required to align each otoscope assembly individually. Therefore, it is recommended that a method be researched to produce a more consistent method of manufacturing otoscope heads as to make fiber optic alignment identical for every model. Although this may require the design of an entirely new light delivery system, it would be easy to integrate into the otoscope head assembly. Parameters could be changed to allow the beam splitter cube to be placed closer to the tip of the speculum to allow for a greater field of view, and a more robust material can be used to increase package stability.

9.2. Thermo-Mechanical Effects

Another aspect of the system that was not analyzed is its thermo-mechanical properties. Heat is the primary byproduct of the system while running. The entire assembly of parts comes in contact with a high powered Compass 532nm 50mW laser that reaches temperatures of 131 degrees Fahrenheit under operating conditions. This heat causes mechanical pieces that it contacts to deform and potentially affect the quality of the reconstructed holographic image. The addition of a fan to cool the components may induce vibrations that adversely affect the stability of the system as well. Thus, cooling fins are a reasonable option to analyze for optimization of a solid state cooling system.

A second aspect that may affect the heat of the system is insulation for the acoustic subsystem. Material may be added to absorb the kinetic energy from the waves propagating from the speakers on the otoscope speculum or to increase the overall system's fundamental natural frequency of vibration. However, the way that insulation mitigates kinetic energy from sound waves and background noise is by converting it to heat as the sound wave dissipates. Therefore, development of a more sophisticated insulation system must be accompanied by the analysis of potentially harmful thermo-mechanical effects.

9.3. Packaging and Prototyping

Overall, the ability to use the Stratsys Dimension FDM Rapid Prototyping Machine proved beneficial to show proof of concept of the iterative designs as well as to validate and characterize the first iteration that was printed. One problem that was encountered was due to the resolution capabilities of the Stratsys machine. Having a resolution of $\pm 0.25\text{mm}$, potential existed for tolerance stacking between the different regions of the package as well as the

differing manufacturing processes between standard Thorlabs parts and the hand lathed connectors for the first iteration.

Although minor alterations were necessary, alternatives to using the in-house 3D printer are not economical. To reduce the potential for tolerance issues, a higher density polymer could be used instead of the ABS used in the Stratysys machine. For the second prototype, in the interest of saving time and possibly increasing end product quality, consideration was put into outsourcing the process. Prototek Machining and Fabrication, LLC was contacted in regards to this matter. Accura 60 polymer was recommended as the new material as it was the highest density resin available that would give the best possible resolution. The estimated cost to have the second iteration prototyped, using similar stereolithography technology, was \$1,100 to \$1,400. The quoted price for the in-house Stratysys machine using ABS was \$122.12. The obvious trade off for quality was a 1000% increase in cost.

Another limitation that the rapid prototyping demonstrated was its dependence on the direction in which the part was printed. Since the machine operates based on material layer deposition, the resolution and quality of certain features can be compromised by the direction in which it is printed. The most notable inaccuracies are apparent with the circular slot features. The slots for the half-threaded camera ring as well as the cutouts for the fiber end connectors showed inconsistencies in their circular shape. Since the parts were printed as shown in Fig. 28, the layers of material were printed so that the cylindrical portions were printed starting from a tangent plane and ending at the package split. Due to the printing process, the round edges formed a staggered pattern that made high ordered polygons instead of circles. Although not possible in this design, such inaccuracies could be accounted for by printing the prototype in a

direction such that the layers are deposited so the circular profile is printed instead of printing across the sides.

10. Spectroscopy

When using laser imaging, it is essential that the surface upon which the beams are emitted is reflective enough to produce a good clean image. When a laser, or any light source is shined on an object, a percentage of the emitted photons are transmitted through the object, another percentage are absorbed by the object, and the remaining photons are reflected at an angle equal to the contact angle. The amount of light that falls into these three categories is dependent on the material's mechanical and optical properties. For example, a very dark object will absorb the majority of the light shined on it, while a bright object will not. Similarly, a translucent object will allow more light to pass through it than an opaque one. The material that this project focuses on is the tympanic membrane, which is somewhat translucent and therefore not very reflective. In order to increase the quality of the laser image, the membrane must be altered somehow. The most practical way of doing this would be to coat the membrane with a thin reflective film. While there are many such chemical compounds that would aid in this matter, most are unsuitable since there are many concerns and limitations regarding what is permissible to use on the human tympanic membrane.

Firstly, the coating must not be toxic, or cause any inflammation or irritation to the skin. Second, there must be a safe method for applying and removing the coating. For example, if the coating must be scraped or peeled off, or needs extreme heat or pressure to apply, it is obviously unsafe and therefore undesirable as a potential candidate for coating materials. Beyond the health concerns, there are also concerns about what impact the coating will have on the results of the experiments. If the coating is too thick or too rigid, it may affect how the membrane vibrates, thus leading to incorrect measurements. Additionally the coating would need to be highly reflective specifically within the wavelength region of the laser that is used during the

tests. Lastly, referring back to application concerns, the coating would need to be evenly distributed on the membrane, as any large scale unevenness could alter the vibration patterns. Overall what this means is that when testing reflectivity, the approved coatings will have to be analyzed under different wavelengths, and safe application and removal methods will also be examined.

10.1 Coatings Research

10.1.1 Titanium Dioxide and Cosmetic Make-Ups

Titanium Dioxide, TiO_2 , is most commonly found as a crystalline powder derived from the Rutile mineral. It is desired for its highly reflective and hydrophobic nature. These characteristics make it an ideal choice for use in cosmetics and other such skin covering applications. Titanium dioxide is relied upon heavily by the sunscreen industry for its ability to efficiently reflect UV rays from the sun. TiO_2 also holds an importance within the medical and scientific communities. It is used primarily as a coating substance with varied applications. Uses such as the use of TiO_2 nanotube arrays as a surface for biomedical implants, being an additive in the resin that forms dental fillings, to its incorporation as a photocatalyst in electrolysis processes. It is interesting to note that in the studies of its use in visible light cured dental resin, there is a linear relationship between the resin's reflectivity index and the percentage of TiO_2 used in its mixture (Titanium Dioxide).

Titanium dioxide, although used topically for cosmetics and sun protection, has an uncertain health risk associated with internal exposure. Especially when particles are in the nanometer range there is debate over whether or not TiO_2 has carcinogenic effects on humans. Compared to their counterparts in bulk form, it is possible for nanomaterials to have different

chemical and physical properties. Unfortunately, as small particles hold the most use as a reflective coating, they may not be suitable for use in a human application. The International Agency for Research on Cancer (IARC) classified TiO₂ as a possible human carcinogen when inhaled. Particles in the nano scale can bypass cell's protective membranes and work their way through cells into other bodily systems (J. Wang et al).

TiO₂ has been used for some time as a coating for reflectivity testing and optical interferometric metrology. It has been found to be useful for most applications while having few difficulties, mainly concerning delivery to, and extraction from, the ear canal. Painting the tympanic membrane can be done with a brush or spray applicator (needing to be developed/improved for use in the middle ear). Problems that arise are that larger particles tend to clump and it is difficult to evenly apply. Safe removal is another issue that needs attention as titanium oxides long term effects are unknown in human (J. J. J. Dirckx, Coating Techniques).

A possibility for a coating that has similar characteristics to TiO₂ is the use of a topical makeup product. As reflectivity testing is not a normal analysis done on beauty supplies, there are few if any studies done on how well a specific make-up will reflect a beam of light in any wavelength range. For this reason, it would be pertinent to use a white color cosmetic for testing in the tympanic membrane. As white has the best average reflectivity over the spectrum of light, it is a good base from which to begin a study.

10.1.2. Sublimating Waxes

10.1.2.1. Cyclododecane

Cyclododecane is a stiff wax, also known as sealing wax, which can sublime at room temperatures. When combined with petroleum ether in certain quantities, the boiling point of the

wax can be modified to vary between 35-60 degrees Celsius. Thus the wax could be sublimated and then condensed on the tympanic membrane with a melting point above body temperature, or be placed on the membrane and later sublimated off if the melting point is below body temperature.

Typically the wax is white in color but can be made orange or blue with pigments. The exact reflectance spectrum of the substance is unknown and warrants experimentation. Although no numerical data is available, the wax is said to have a relatively high stiffness. Thin coatings would thus be necessary, and even then it is possible the coating will significantly affect the function of the tympanic membrane. Uneven application of the wax may produce large fluctuations in the vibration of the membrane. Cyclododecane may be a skin irritant, but its relative medical risk as compared to other methods is not clear. As well, the presence of petroleum ether poses another source of irritation or injury. More research or experimentation would prove insightful into the use of this substance.

10.1.2.2. Beeswax / Paraffin Wax

Beeswax and paraffin wax were also investigated for sublimated wax application. Both beeswax and paraffin wax have a low specific heat, on the order of 3 kJ/kg*K. The boiling point of the wax is roughly 350 degrees Celsius. Thus, the heat transferred to the membrane would be roughly $0.1 \text{ W} / \text{cm}^2$ if the wax condensed on the membrane at a rate of $1 \mu\text{m} / \text{second}$. The exact condensation rates as well as heat transfer thresholds of the membrane are as of now unknown and data on this are necessary to determine the feasibility of this method.

It has also been noted that the application of oleic acid to beeswax lowers its tensile strength. This would reduce its effects on the movements of the membrane. However, the effects

on sublimation as well as any toxic effects of the acid are not clear. Ideally the acid could be applied to the wax after it had sublimated on the membrane, however this may not be safe or physically possible.

Both waxes also have a flash point lower than their boiling point: about 200 degrees Celsius. This means that any ignition source that comes into contact with the wax once it has sublimated (or even at temperatures lower than that) will cause it to burn. Thus the heating elements as well as any applicator must be free of sparks or flames so as not to ignite the wax. Particular care would be required while the wax is in the ear and at a temperature above the flashpoint. This would represent a small amount of time, as the wax will cool rapidly once contacting the ear canal.

Colors of the beeswax vary and exact spectral properties warrant investigation. Pigments added to the wax may or may not sublime or condense properly. Further experimentation is required. It is assumed that both waxes discussed could be removed from the membrane using the natural cleaning processes of the ear.

10.1.3. Collodion

Another of the potential coatings considered for enhancing the reflectivity of the tympanic membrane was collodion. Collodion is generally applied to the skin as a medical coating however for the sake of this experiment, it may not be feasible to apply it to the tympanic membrane. Liquid collodion is applied by allowing its vapors to condense on a surface, thus forming a thin film on the intended target. Although it is used as a skin coating in medical applications, there are many health hazards involved in its use as well as other negative factors that make it undesirable as a reflective material. The chemical dangers associated with it

are its high flammability, as well as its toxicity if inhaled. Another issue with using collodion is that it acts as a skin irritant. Furthermore, it has a boiling point of 96F meaning that it would be difficult for it to remain condensed on the ear drum which is often times close to the body's core temperature of 98.6F. This however may be beneficial in terms of removing the coating after the experiment is complete. Another important issue regarding collodion is whether or not it affects the vibration of the ear drum. One source states that "Coating the tympanic membrane with collodion causes no great real increase of the vibrating mass or of its moment of inertia (E. Luscher)", while another source states "the effect of tympanic membrane vibration was reduced in his subjects by coating the membrane with collodion (M. E Lutman)." Aside from the moderate health risks and discomforts it presents, it is also a bad reflector. This is because it is a clear liquid, thus allowing light to pass through it. Therefore collodion is undesirable as a reflective coating (Collodion; MSDS).

10.2. Decision on Chemicals Used

After narrowing down the list of possible coatings, a discussion with some of the doctors at MEEI helped determine which coatings to test, and at what concentration levels. The current coating used by the doctors during their tests on post-mortem animal membranes is titanium dioxide (TiO₂) at a concentration of 450mg per 5ml of water. The substances that were most promising for safely increasing reflectivity were Titanium dioxide (TiO₂), Zinc oxide (ZnO) and diluted methylene blue. See Table 4 for the various concentrations proposed for each coating.

Additionally, it was desirable to have a small particle size for the solutes so that the thickness of the coating would be minimal, and it would have a more even distribution. The oxide

chemicals were both purchased from alfa-aesar, and the particle sizes are also shown in the table below.

Table 4: Table of Chemicals and Concentrations Used

	Concentration	Particle size(s)
TiO ₂	200mg / 5ml H ₂ O 450mg / 5ml H ₂ O 700mg / 5ml H ₂ O	32nm unknown size (from MEEI)
ZnO	200mg / 5ml H ₂ O 450mg / 5ml H ₂ O 700mg / 5ml H ₂ O	7-13 nm 20-30nm
Methylene Blue	150mg / 15ml H ₂ O 1250 mg / 15ml H ₂ O	unknown

Since TiO₂ does not dissolve in water, the coating is prepared at MEEI by mixing the two substances in a vial, and then placing the vial in a machine which shakes it very rapidly, until the water becomes cloudy, and all the TiO₂ particles are evenly distributed. If the mixture is left alone for more than 5 minutes, the TiO₂ particles will accumulate on the bottom of the vial, thus decreasing the concentration of the mixture. Therefore, it is very important to have the mixture well shaken immediately before applying it. The same effect of the sinking particles was also observed with the zinc oxide on a more extreme level. This is likely due to the higher density of those particles.

10.3. Methodology for Spectroscopic Analysis

10.3.1. Sample Materials

Since the reflectivity testing was unable to be done on actual membranes, it was necessary to find a substitute that shared similar properties to that of an actual tympanic membrane. Some of the essential characteristics of the TM are that it is about 0.1 mm in thickness, it is mostly translucent, it's hydrophobic, and is not very rigid. One TM substitute used in testing that matches this description is semi translucent paper. This special kind of paper has a 0.1 mm thickness, is hydrophobic, but is more opaque, and more rigid than the TM. While this kind of paper seems to be a good proxy, there were several issues regarding the coating of samples. First, the surface was a bit too hydrophobic, and it took a long time for the coated droplets to dry. Second, after the coatings were painted or dripped on to the paper, and given time to dry, the paper would warp, thus leaving an uneven surface which could adversely affect the accuracy of the results. Because of this warping, or wrinkling, the samples were tested while the coatings were still wet, which is not ideal for actual testing on humans. Similar issues also arose when the coatings were tested on wax paper. The wax paper was more water resistant than the translucent paper, but less opaque and less rigid. The last set of tests was performed by sandwiching a droplet of each coating between two glass slides. This provided a very thin uniform film of each coating that could be examined on its own. The results from this would determine the reflectivity of an extremely thin coating if such a thin layer of coating were one day able to be applied to the TM of live patients.

10.3.2. Initial Proposed Application Methods

1. Apply a few drops onto the coating. Wait for it to dry such that residue remains. Use kimwipe to absorb excess liquid. Allow some samples to dry without kimwipe to simulate isolated drying in the ear.
 - a. If sample begins to curl or deform, use a larger sample initially and then cut to fit on the slide once it has dried
2. Brush the coating onto the sample. Investigate different brushing strokes to optimize uniformity. Once an optimal method is identified this will be used to brush all coatings onto that specific sample.

10.3.3. Measuring Thickness

A very exact method for thickness measurements has not been identified which falls into both time and money constraints. Therefore focus was placed on a general magnitude of thickness, and changes of interferometric measurements were used to determine if the sample had become too thick. Coated samples were rejected if their thickness exceeds double their uncoated thickness as viewed by the eye and with caliper measurements.

10.3.4. Uniformity

Each prepared sample was at first inspected with the eye to determine if any blotches or blatant nonuniformity can be found. While measuring the samples, measurements were taken from three separate locations on the sample. This provided a sense of variation as well as a quantitative deviation for samples.

10.3.5. Workflow

One coating type was prepared on each sample type using both methods. Once this was complete the samples were loaded and each light source was tested before unloading the sample. In the event that samples spoiled rapidly, a smaller batch was prepared before testing. Once all testing of one coating was complete, the next coating was investigated.

10.3.6. Sample Mounting

Once coatings are applied, the samples were sandwiched between two slides to ensure that it was laying flat. It was then clamped above the probe of the spectrometer. The white light emitter was placed directly above pointing downward, and 780nm as well as 532nm laser light was illuminated from a slight offset. Before final testing began it was important to determine that the illumination provided reliable and constant values for each sample. Reference samples were recorded over different time intervals, ensuring that the system did not drift significantly between measurements.

10.3.7. Data Organization

Each (coating type – concentration) combination was assigned a number. For example: Methyl Blue: 50% = 1, Methyl Blue:75% = 2, TiO₂: 50% = 3. This was then appended with a letter corresponding to the application method. This was used as the convention for saving files, which allows for expansion should other tests be decided upon. Within each file, there were three columns of data, one for each light system used, which graphed intensity versus light wavelength (as output from the spectrometer). The output was saved as raw data, which was analyzed after all data had been compiled.

10.4 Configuration of Testing Apparatus

An iteration of test setups were designed which provided increasingly pertinent spectroscopic data. Three systems provided results and insight into the reflectivity of our samples. With each generation, improvements in measurement and characterization were achieved.

10.4.1. Configuration 1

The first iteration was a basic reflectance setup which provided for measurements at varying angles of incidence. Ultimately, it was not able to be adapted for use with laser illumination, but worked well to illustrate the underlying mathematics involved in spectroscopy.

10.4.1.1. Components

1. Light source (to provide predictable and wide range illumination to the sample):



Fig. 44. Thorlabs OSL1 Illuminator with Tungsten Lamp

2. Optics to focus the light onto the sample:

- a. Plano-Convex 30mm focal length lens
- b. Linear Polarizer
3. Optics to gather and focus light received from the sample:
 - a. Plano-Convex 30mm focal length lens
 - b. Linear Polarizer
4. Spectrometer to measure light received:



Fig. 45. Tristan USB Spectrometer

10.4.1.2 Experimental Setup

A 30mm cage system purchased from Thorlabs was used to align the optical components in two dimensions. These were then mounted using swiveling clamps to allow easy adjustments of heights and angles for each cage system independently. The light source and spectrometer fibers were both mounted rigidly to the caging system, while the lens and polarizers utilized quick release cage plates. This allows them to be repositioned axially or removed easily. The individual cage setups are shown in Fig. 46 without a polarization stage present.

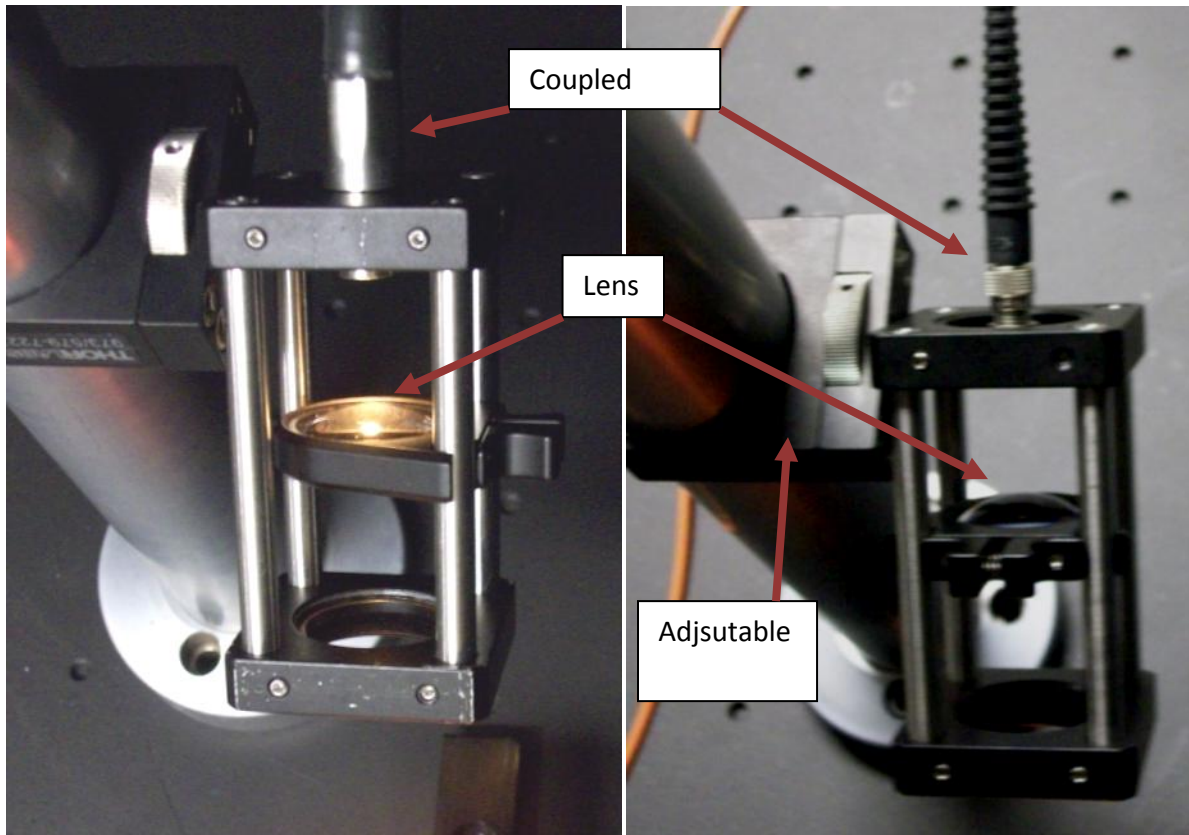


Fig. 46. (left) Light Emitting Cage and (right) Light Gathering Cage

A platform is then placed between the two cage systems to hold the sample. Optionally, this platform can be mounted on a rotary stage to allow for investigation of the sample from multiple angles. The cage systems are then aligned and the lenses are shifted to ensure that light is hitting the sample with the right intensity, coverage and angle and that the spectroscope is receiving light optimally from the sample. The system, after alignment, is shown in Fig. 47. Experimental Setup (front) and Fig. 48. Experimental Setup (back).

During the alignment procedure, the lighting system is typically manipulated until it is at the appropriate orientation. The measuring system is then adjusted while real time measurements from the spectroscope are being viewed from a standard sample. The experimenter then locates

an angle at which the most light is being gathered from the instrument. If a saturation situation is achieved, intensity of the lamp is adjusted to offset this affect.

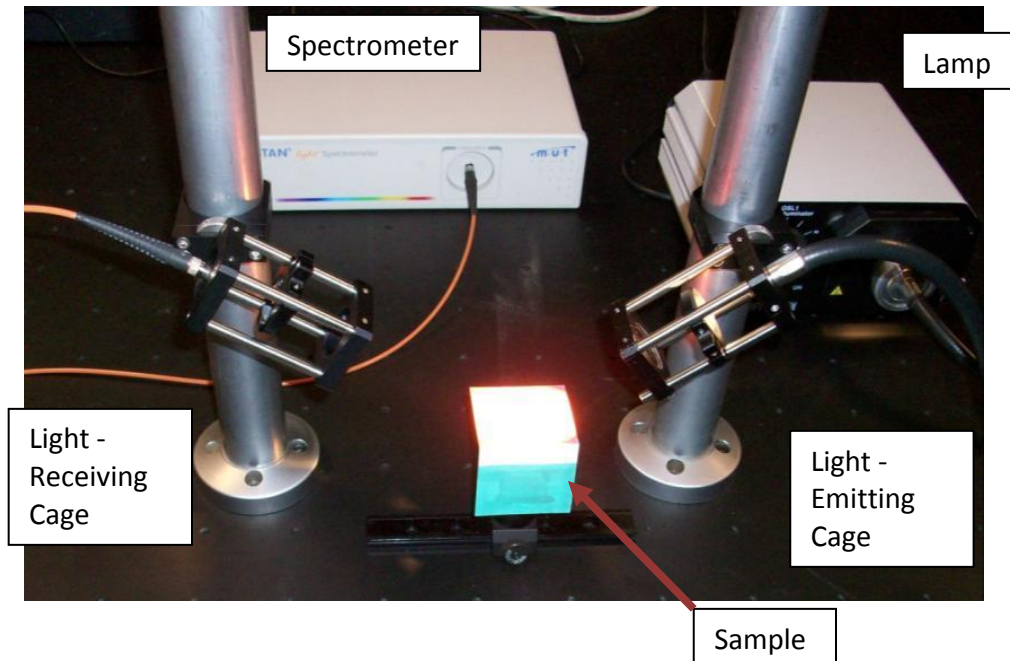


Fig. 47. Experimental Setup (front)

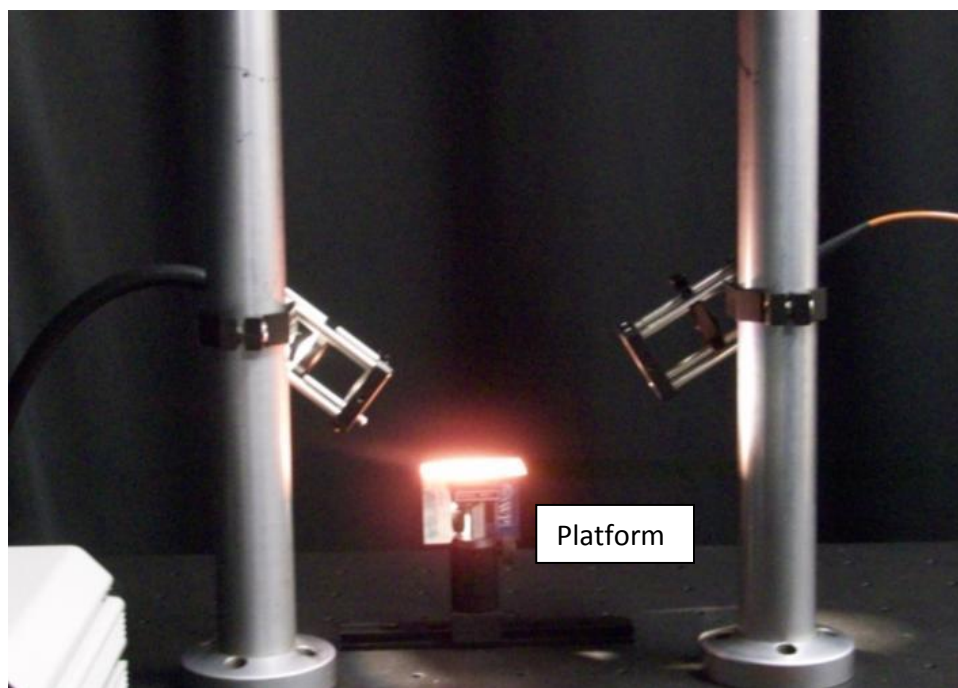


Fig. 48. Experimental Setup (back)

10.4.1.3. Measurement Procedure

Once the system has been aligned for sample measurements, a simple procedure is to be followed:

- 1) A reference sample is mounted on the platform. This reference sample should reflect light within the wavelength range the experimenter is expecting to measure. Most commonly a white sample is used. This reference is assumed to reflect more light than the sample. The lamp can be adjusted at this point to maximize light without overexposing. All other sources of light interference, at this point, should be minimized.
- 2) A measurement from the spectrometer is taken. The data gathered is not only a function of the reflectance pattern of the reference, but also the spectral characteristics of the emitting light source. For this reason, the characteristics of the reference sample should be recorded, as this may be of importance for post analysis. An example of a collected spectrum is given in Fig. 49. Raw Data of Reference.

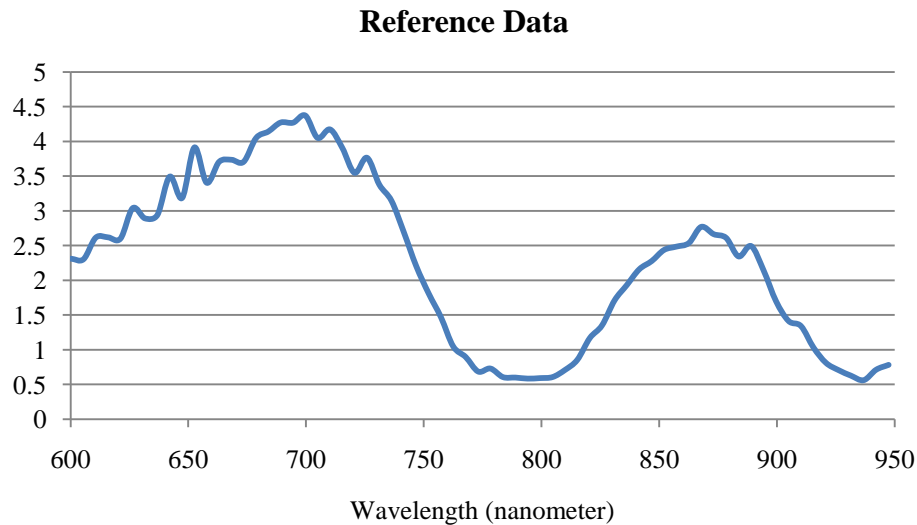


Fig. 49. Raw Data of Reference

- 3) The reference is removed and the sample is mounted, with the platform adjusted to ensure that the top surface of the sample is at approximately the same height as the reference.
- 4) Without adjusting the lamp or caging systems, a reading is taken and recorded. Angles of light incidence as well as orientations of polarizers should be particularly noted and recorded alongside the data as these may be important parameters for post analysis. An example of a green sample reading is given in Fig. 50. Raw Data of Green Sample.

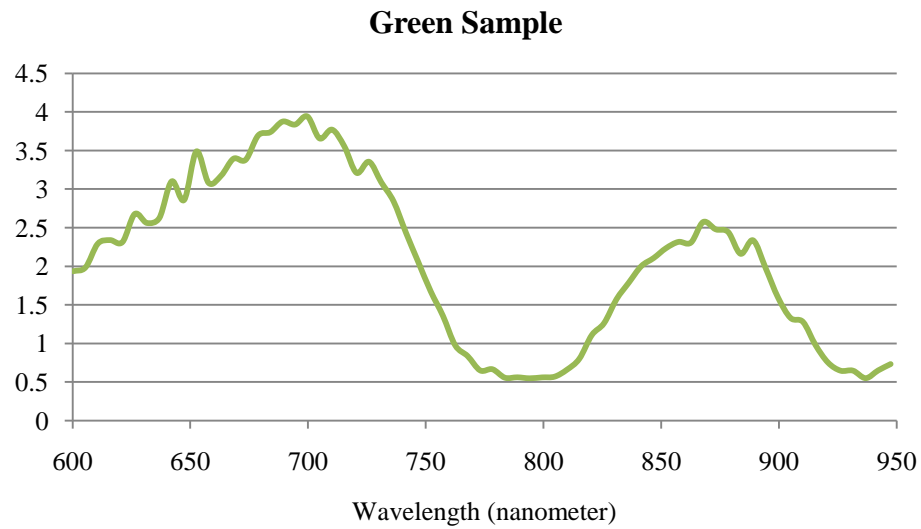


Fig. 50. Raw Data of Green Sample

10.4.1.4. Analyzing the Data

Fig. 51. Raw Data of Reference and Sample displays the absolute light received from the spectroscope (given in arbitrary units) for the reference white card as well as a green card.

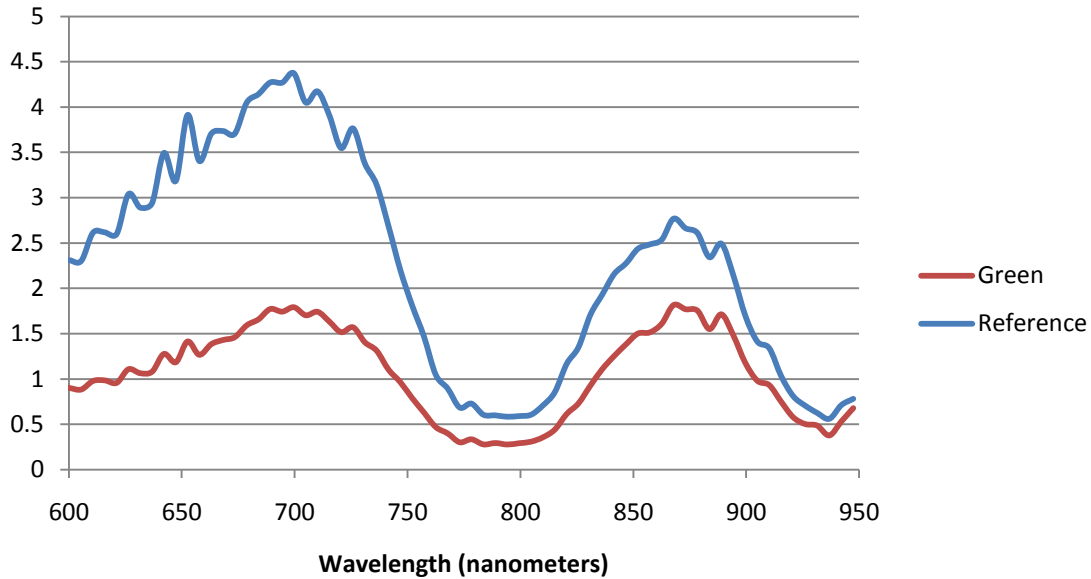


Fig. 51. Raw Data of Reference and Sample

There are clearly two problems with the given plot. Firstly, it is very difficult to view a change in shape of the spectral graph (as compared to the large translation observed) and secondly the units of the y-axis are given in an arbitrary value.

As previously mentioned, the readings include a spectrum that is biased heavily by the light system used. Although this bias can be predicted using the specifications of the lamp provided, variations will still occur. It is necessary to reduce uncertainty of this value by introducing a reference reading. As a result, absolute measurements of any sample cannot be determined without extensive post-manipulation of the data. Our procedure seeks to quantify relative data as an approximation to absolute reflectance using simpler analysis techniques.

To solve the aforementioned problems, a percentage is sought rather than an absolute value. Since the lamp's spectrum remains relatively constant between two readings, its influence will be removed. Percentage of light transmitted and absorbed can then be calculated with reference to the white sample (which is assumed to reflect all wavelengths). Since all samples are compared to the same reference surface using the same lamp, percentage reflectance and absorption can then be compared between samples. Accuracy can then be checked using a standard sample to verify final results.

Equations Used:

$$\%T = 100 * \frac{I_t}{I_0} \quad (10.1)$$

$$I = \log \frac{I_0}{I_t} \quad (10.2)$$

Where $\%T$ is the percent transmission, I_t is the light reflectance measured from the sample, I_0 is the light reflectance measured from the standard white surface, and A is the light absorbed by the sample.

10.4.1.5 Results of Analysis

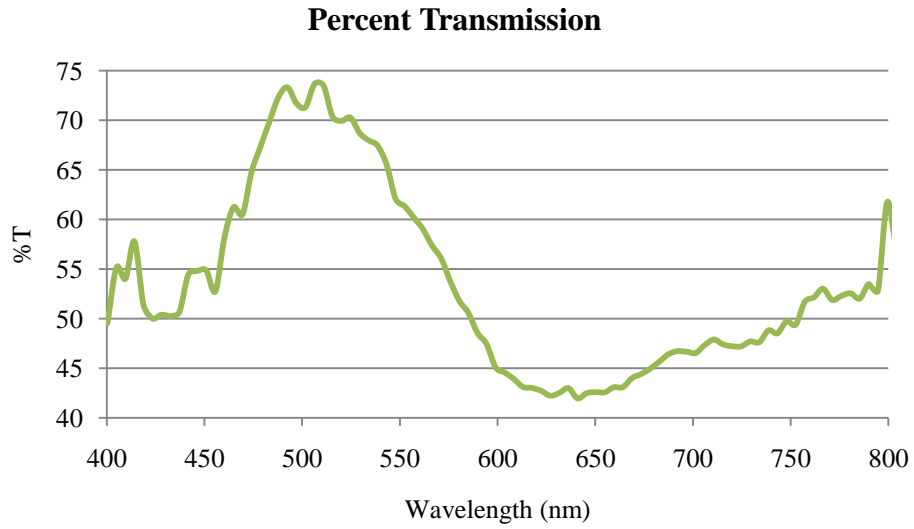


Fig. 52. Percent Transmission of Green Sample

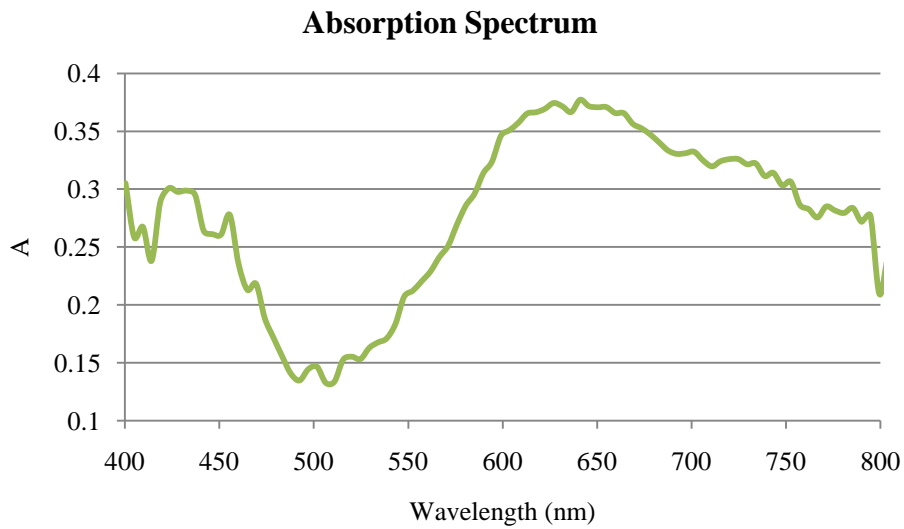


Fig. 53. Absorption Spectrum of Green Sample

These charts have been focused on a range of wavelengths which highlight the characteristics of green light. From this analyzed data, it is clear that the most light is transmitted

at roughly 500 nanometers, which also corresponds to the lowest absorption. From here, further analysis may be done, or parameters selected based upon the wavelengths of light which are best transmitted (or absorbed) by the sample.

10.4.2. Configuration 2

Configuration 2 was designed to allow for spectral investigation at particular laser wavelengths. Transmission light was easier and more reliable to couple into the spectrometer with the probe placed behind the coated sample.

Our test setup involved transmission spectrometry using a 780nm and 532nm laser source as well as a tungsten lamp to provide white light illumination. Samples were rested above the spectrometer with the light sources coming from above, one at a time.

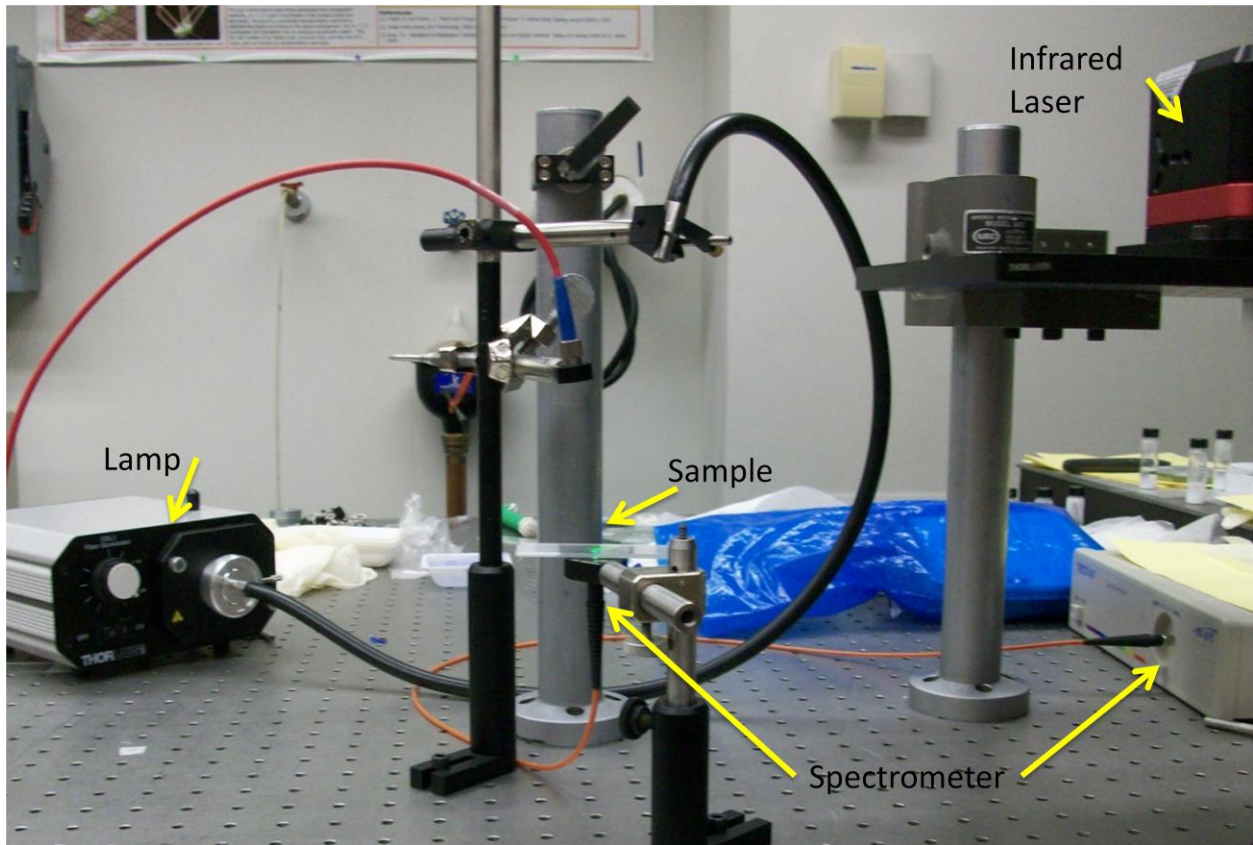


Fig. 54. Configuration 2 Setup

The white and green lights were introduced using a fiber, and the red light was reflected off of a mirror.

10.4.4. Fringe Pattern Testing

The next step is to test the samples in the holographic interferometer to test fringe pattern quality (only with a 532 nm setup). For this, samples will be sandwiched between metal washers and excited acoustically.

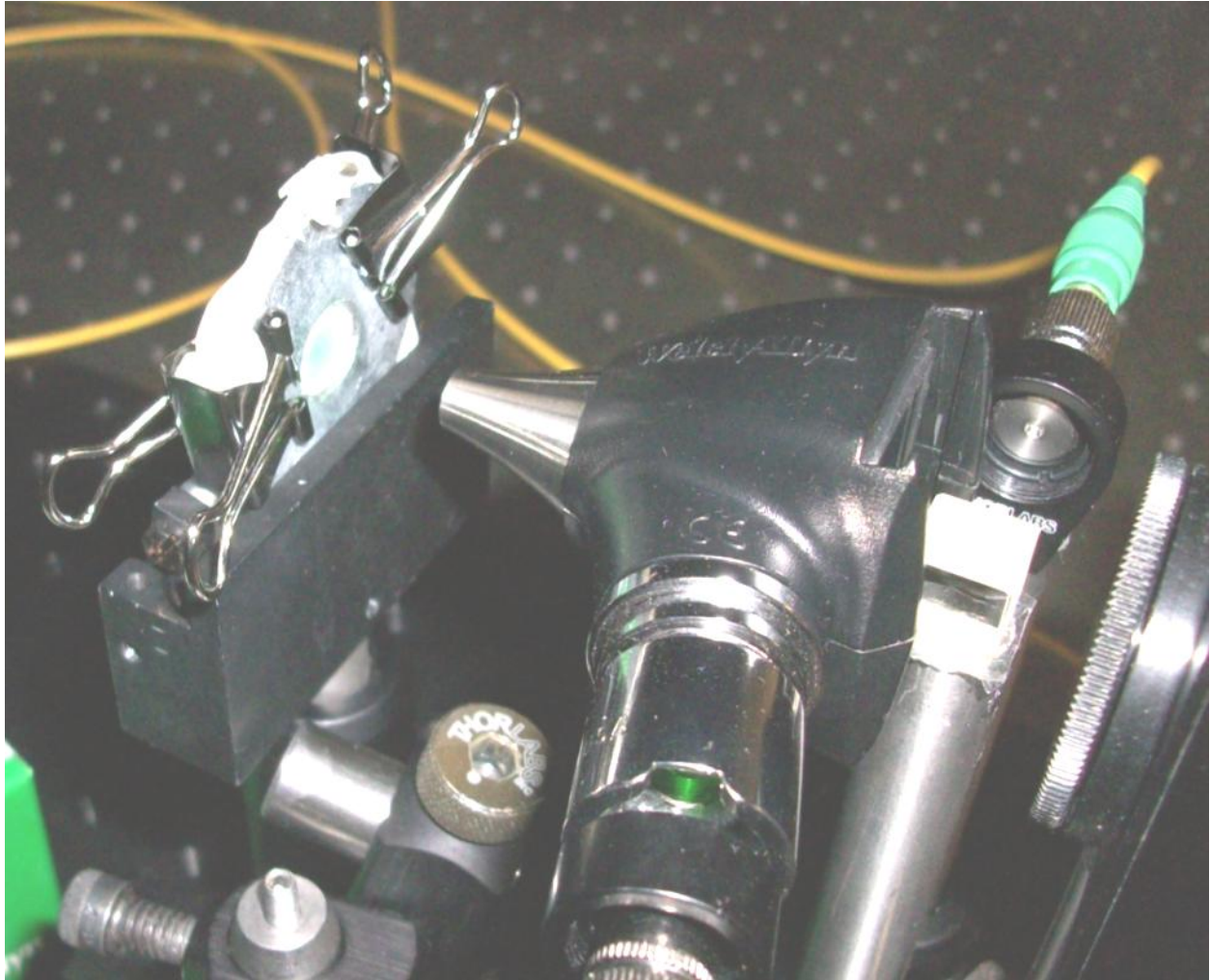


Fig. 55. Fringe Pattern Testing Setup

10.4.5. Surface Interaction Experimentation

Finally, a more even coating on a hydrophobic surface was investigated using surfactants commonly found in cosmetic products. Sucrose was one surfactant that was investigated to lower surface tension. In theory, this allows the drops to spread out more evenly on a wax paper sample (or the tympanic membrane) which results in a more even coating.



Fig. 56. Comparison of Different Concentrations of Decyl Glucoside

The row all the way to the right has a large amount of sugar dissolved in it, the middle row has a moderate amount, and the left row is only a water droplet. The contact angle of the droplets is affected by the presence of sugar. Decyl Glucoside, a corn based surfactant used in a large number of cosmetic products, was used to test as a surfactant. There are a large number of commercial surfactants which can be found which are all used for cosmetics. Most are hard to obtain in their pure form. Another possible surfactant is hypoallergenic laundry detergent.

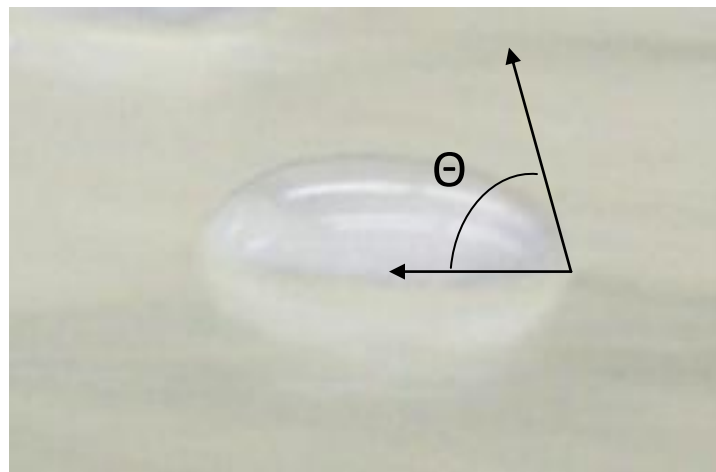


Fig. 57. Contact Angle

10.4.6. Configuration 3

The purchase of a new Ocean Optics spectrometer (*USB2000+XR*) with a reflectance probe (R400-7-VIS-NIR) allowed for more accurate reflectance tests. This allowed pure reflectance measurements to be run with an acceptable degree of reliability. The setup was simple, using the standard procedure as outlined in the Ocean Optics manual:

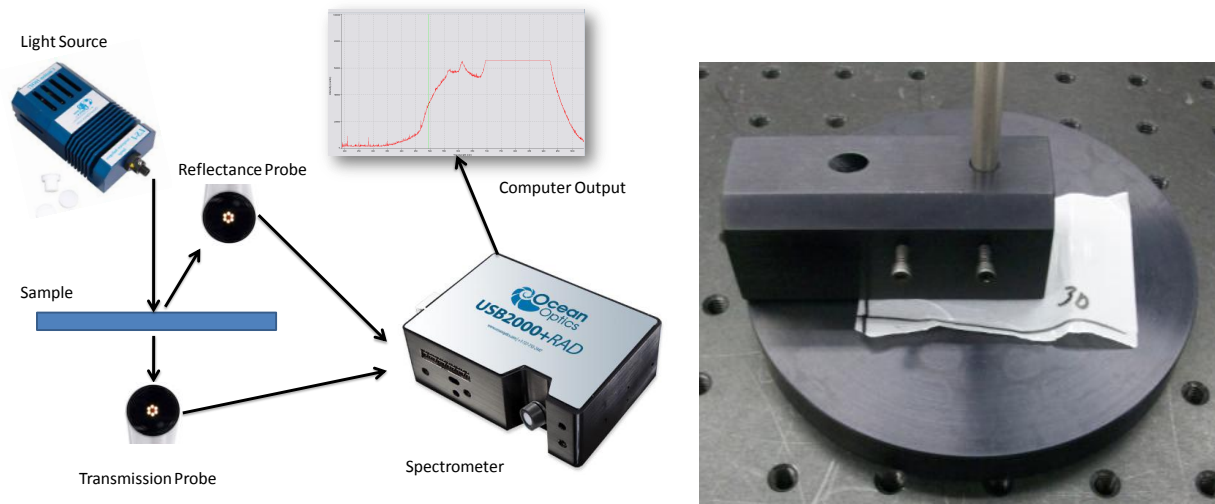


Fig. 58. Spectroscopy Setup - Configuration 3 and Reference Probe

Once the spectrometer had been physically set up, its performance was compared to that of the last spectrometer. The SpectraSuite software allows for direct reflectance tests. However, to avoid undoing any of the background mathematics that the program would perform on the samples, direct irradiance tests were performed to compare the Ocean Optics spectrometer to the previous Tristan spectrometer.

Before any tests are performed, a proper integration time is required to avoid saturation while still ensuring that a significant signal can be obtained. A larger signal will help to reduce noise, as well as avoid potential math rounding errors (however small) during post processing. A

sample with large expected reflectance should be loaded underneath the probe with the system running in continuous mode and the illumination source active. The integration time is increased until the peaks of the graph have nearly reached the saturation level on the graph (roughly 65000 counts).

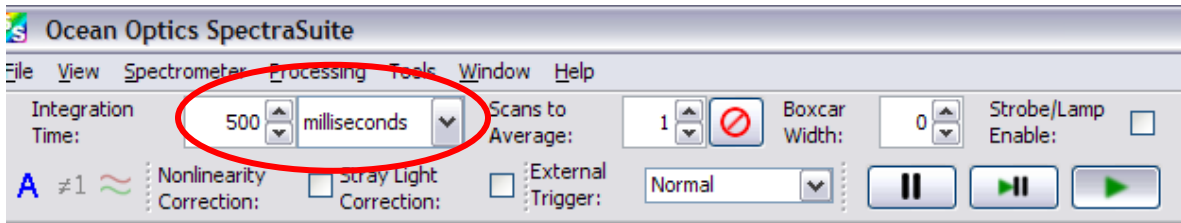


Fig. 59. SpectraSuite Toolbar

Below is an over-exposed sample, showing an integration time which is too high. It is set to 10 seconds for this overexposed sample.

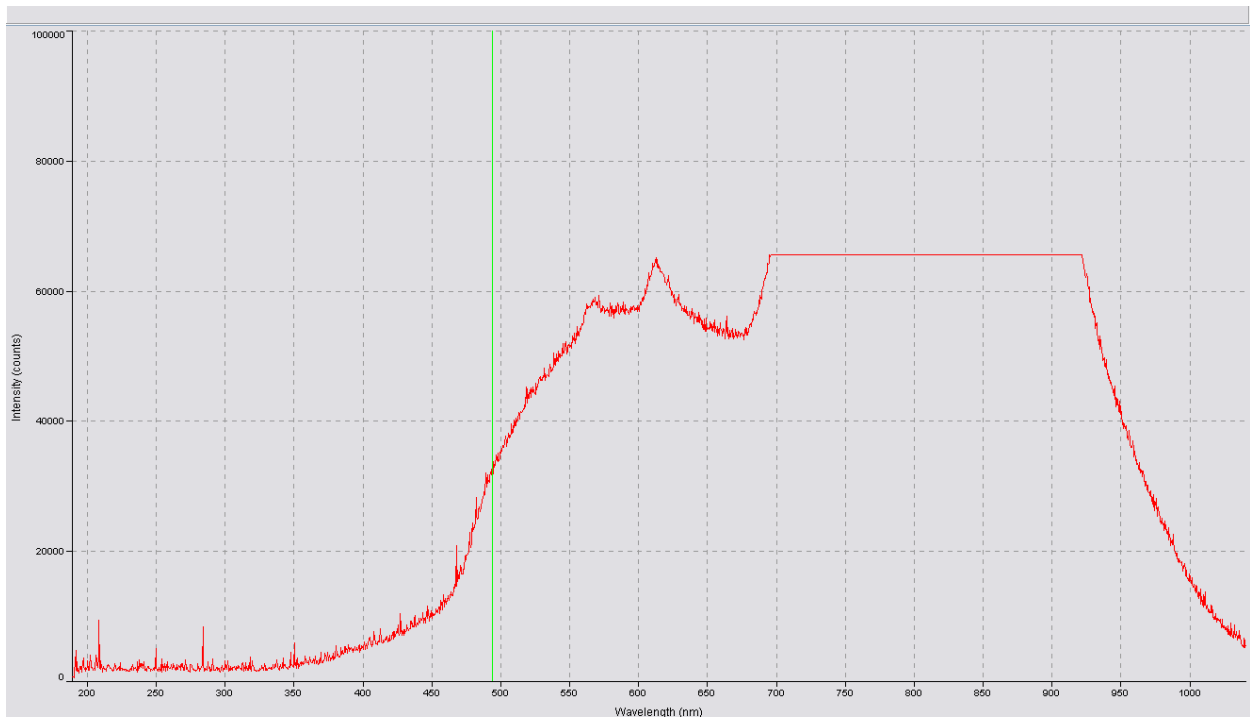


Fig. 60. SpectraSuite Output of Saturated Sample

In order to compare, we then take three measurements directly, as performed in the Tristan experiments which will be averaged. Since transmission tests were compared to a reference (an uncoated sample) we must now repeat the three measurements on an uncoated reference sample. In the future, this reference could be compared to a reflectance standard which would allow for comparison to work done by other groups, rather than simply comparing one of our coatings to another one of our coatings.

Once the three measurements have been averaged, the data must be processed. The mathematics and underlying assumptions must be closely analyzed to compare the measurements taken with a reflectance probe to that of the transmission tests.

Transmission and reflectance values are defined from 3 direct spectral tests as follows:

$$T_{\lambda} = \frac{S_{\lambda}-D}{R_{\lambda}-D_{\lambda}} * 100\% \quad (10.3)$$

$$P_{\lambda} = \frac{S_{\lambda}-D}{R_{\lambda}-D_{\lambda}} * 100\% \quad (10.4)$$

Where T_{λ} is the transmission value at wavelength λ , P_{λ} is the reflectance value at wavelength λ , S_{λ} is the irradiance measured with sample at wavelength λ , R_{λ} is the irradiance measured with reference at wavelength λ , and D_{λ} is the irradiance measured with of dark at wavelength λ .

The tests performed with the Tristan spectrometer ignored a dark reading, as interference and background noise was assumed to be relatively constant, especially if averages were taken, and thus negligible. This simplifies the equations to:

$$T_{\lambda} = \frac{S_{\lambda}}{R_{\lambda}} * 100\% \quad (10.5)$$

$$P_{\lambda} = \frac{S_{\lambda}}{R_{\lambda}} * 100\% \quad (10.6)$$

The equation of energy balance is given as:

$$I = P + A + T \quad (10.7)$$

Where I is the incident light energy, P is the reflected light energy, A is the absorbed light energy, and T is the transmitted light energy.

Since it was assumed that absorbance from the sample was negligible, the equation reduces to:

$$I = P + T \quad (10.8)$$

To produce a reflectance ratio from a transmission ratio, a couple of things must be noted. First of all, illumination power is considered to be constant as the lamps and laser sources did not change considerably from test to test. This meant that, due to our energy balance equation:

$$I_s = I_r \quad (10.9)$$

$$P_s = I_s - T_s \quad (10.10)$$

$$P_r = I_r - T_r \quad (10.11)$$

γ is defined as the ratio of incident light to that of the transmitted reference light. Typically this value is calculated with use of dark and reference values in transmittance tests, but had not been accounted for when initially testing. It is assumed that the transmission ratio be normalized.

Thus:

$$T_r = I \quad (10.12)$$

This automatically defines the calculated reflectance ratio as a normalized value leaving the equation for relative reflectance as:

$$\frac{P_s}{P_r} = \frac{\gamma \frac{T_s}{T_r}}{\gamma - 1} \quad (10.13)$$

The assumption was made that γ is large (greater than 10). This requires that roughly 1/10 of the light be transmitted by the reference material. Although not measured directly, this assumption does not appear to be contrary to the physical setup. This guarantees that error involved by approximating gamma is less than 10% even when transmission values are low (less than 10% of overall light) as shown in the following figure (Fig. 62). Therefore, the samples in which we are interested (high reflectance samples) are expected to have the best correlation between the separate reflectance and transmission tests.

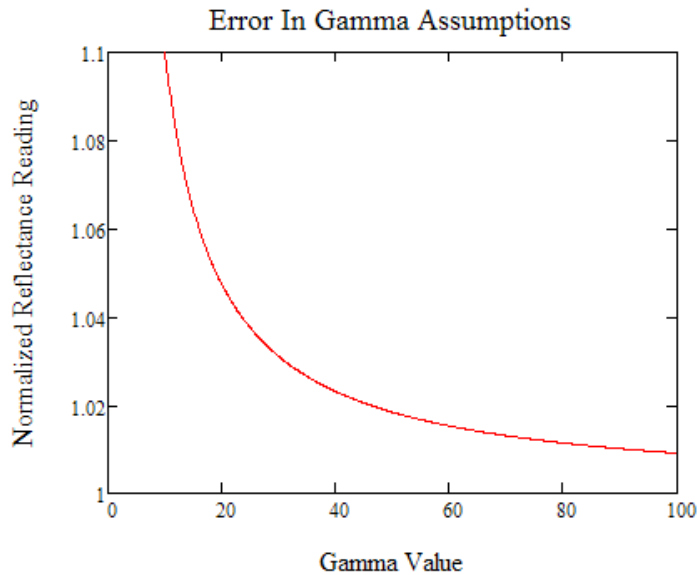


Fig. 61. Error in Gamma Assumptions

This then allows the approximation of a final equation, remembering that the reflectance ratio is a normalized value:

$$\frac{P_s}{P_r} = I - \frac{T_s}{T_r} \quad (10.14)$$

However, the Ocean Optics measurements give a direct ratio of reflectance between samples and reference. Thus one must either denormalize the Tristan data, or normalize the Ocean Optics data to compare exactly. It is in fact much easier to normalize the Ocean Optics data. This is because denormalizing the Tristan data requires solving the coupled equation for true reflectance:

$$P_n = \frac{P_t}{P_t + 1} \quad (10.15)$$

Where P_n : Normalized reflectance ratio and P_t is the true reflectance ratio.

This requires numerical approximation to solve; whereas working in the reverse direction is clearly defined (normalized reflectance is already solved in terms of true reflectance). After comparing the two methods, it is clear that there is some error (most likely from gamma assumptions). However, trends that describe a material's reflective qualities at various frequencies remain preserved.

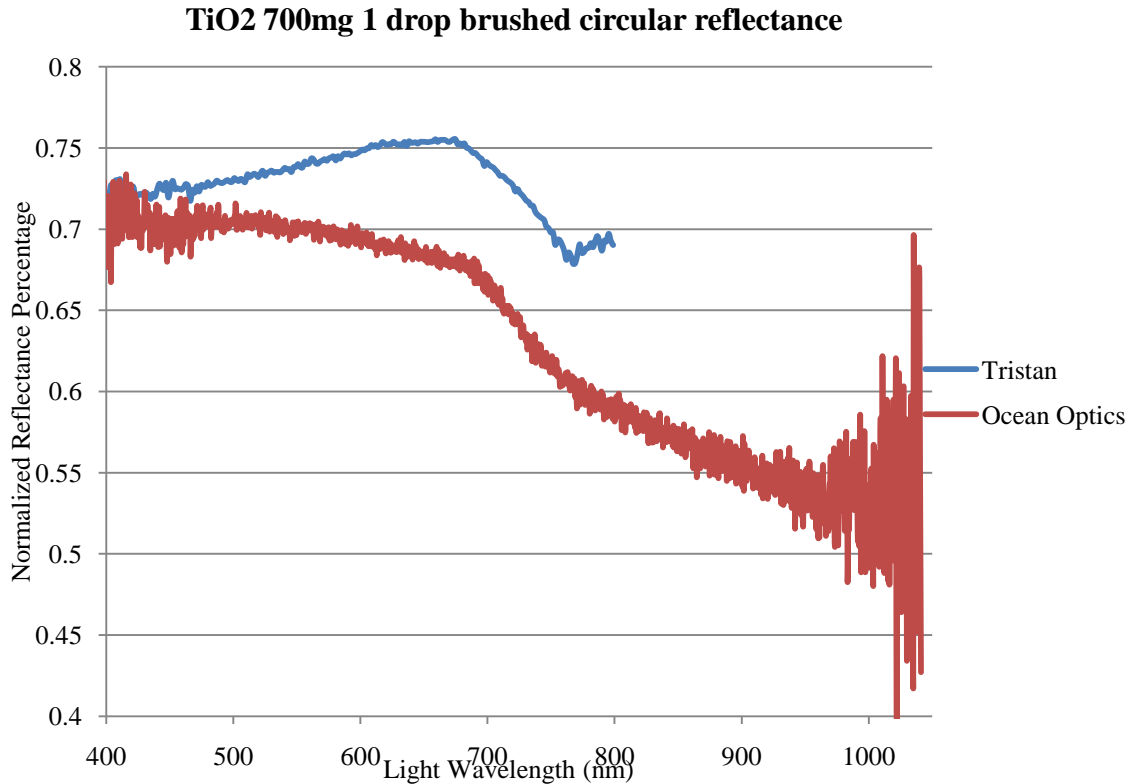


Fig. 62. Full Spectrum Reflectance - 700mg TiO₂ Drop Brushed

10.4.7. LaserView Image captures

A software package known as LaserView 2.0 developed by Ellery Harrington uses digital holography to reconstruct laser images. Once the recording system is set up, the software must be calibrated with the user interface to adjust the brightness and contrast of the images as well as the shutter speed of the camera and the reconstruction distance. The longer the shutter remains open, the more light is allowed into the camera, and thus, the brighter the image. As discussed in the section on digital holography, the reconstruction distance can be adjusted in the software's interface to numerically focus the image. Therefore, without the use of lenses, and without moving anything in the setup, an image like the one in Fig. 63. Numerical Focusing Using Digital Holography below can be brought into focus using only the LaserView software.

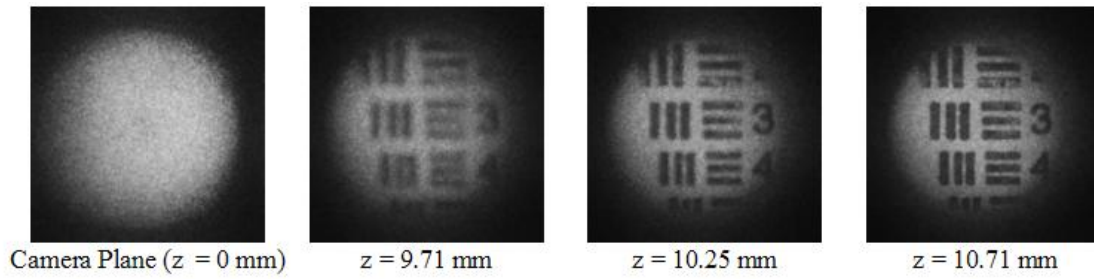


Fig. 63. Numerical Focusing Using Digital Holography

Using LaserView software, several fringe pattern images were recorded for latex membranes coated with the several different samples of reflective additive. Fig. 64. Fringe Pattern Testing with Different Coatings below represents a side by side comparison of these fringe patterns.

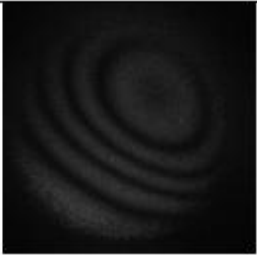
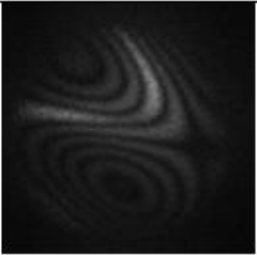
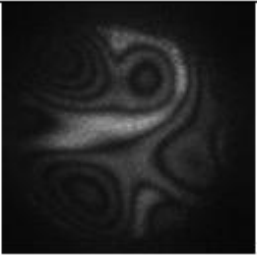
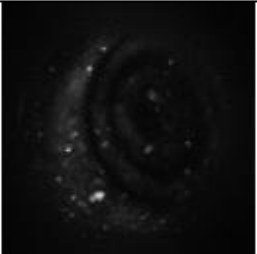
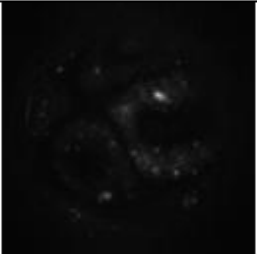
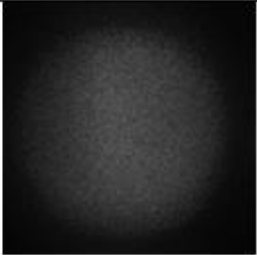
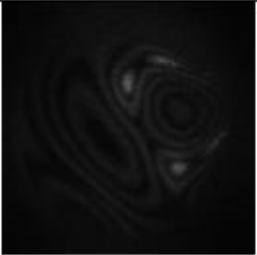
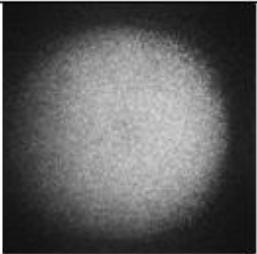
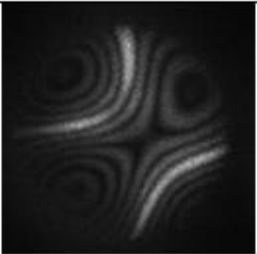
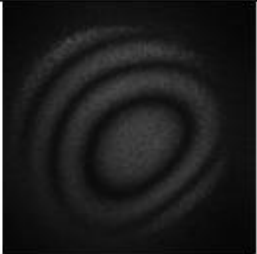
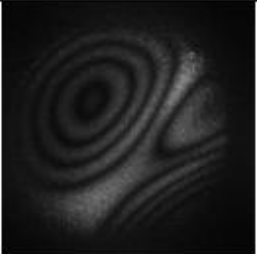
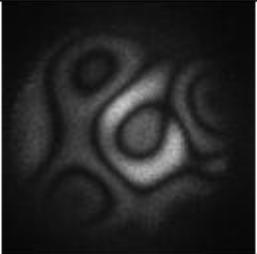
	0.6 kHz	1.2 kHz	2.3 kHz
Reference			
Methyl Blue High conc.			
Methyl Blue Low conc.			
TiO ₂ 700mg/5ml			
ZnO 450mg/5ml			

Fig. 64. Fringe Pattern Testing with Different Coatings

11. Spectroscopic Results

11.1. Comparing Different Application Methods at Different Concentrations

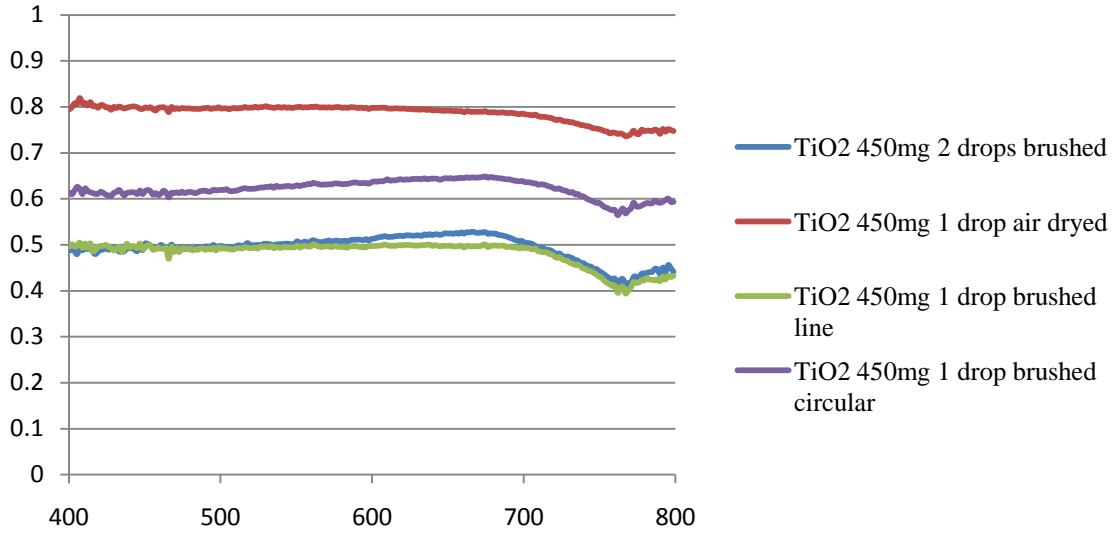


Fig. 65. Measure of Reflectance between Application Methods of Titanium Dioxide at 450mg (Full Spectrum)

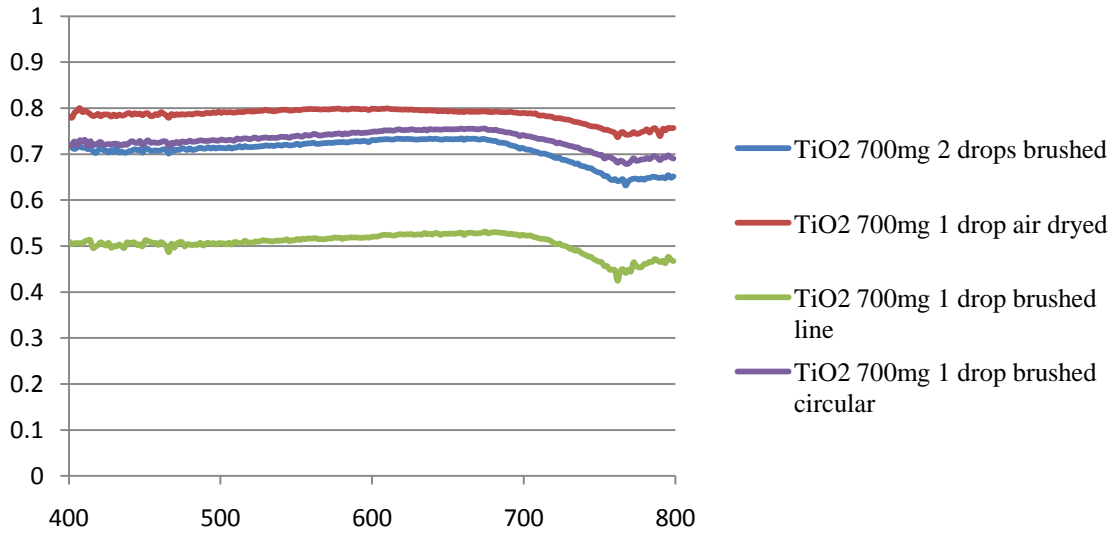


Fig. 66. Measure of Reflectance between Application Methods of Titanium Dioxide at 700mg (Full Spectrum)

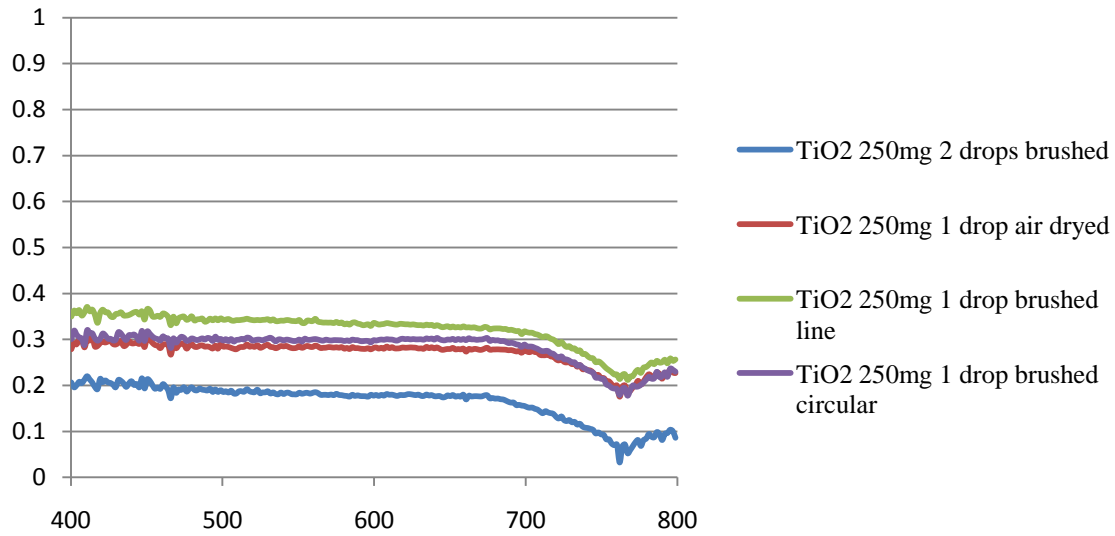


Fig. 67. Measure of Reflectance between Application Methods of Titanium Dioxide at 250mg (Full Spectrum)

From this data it appears that a concentration above 450mg / 5ml is not necessary for straight brush techniques. Presumably a saturation limit has been reached, however improvements do continue for circular brushed and direct drying of the sample. A larger amount of the coating (2 drops) corresponds to more reflectivity. Therefore it is possible to have too little of the coating.

11.2. Comparing Titanium Dioxide to Zinc Oxide at Different Concentrations

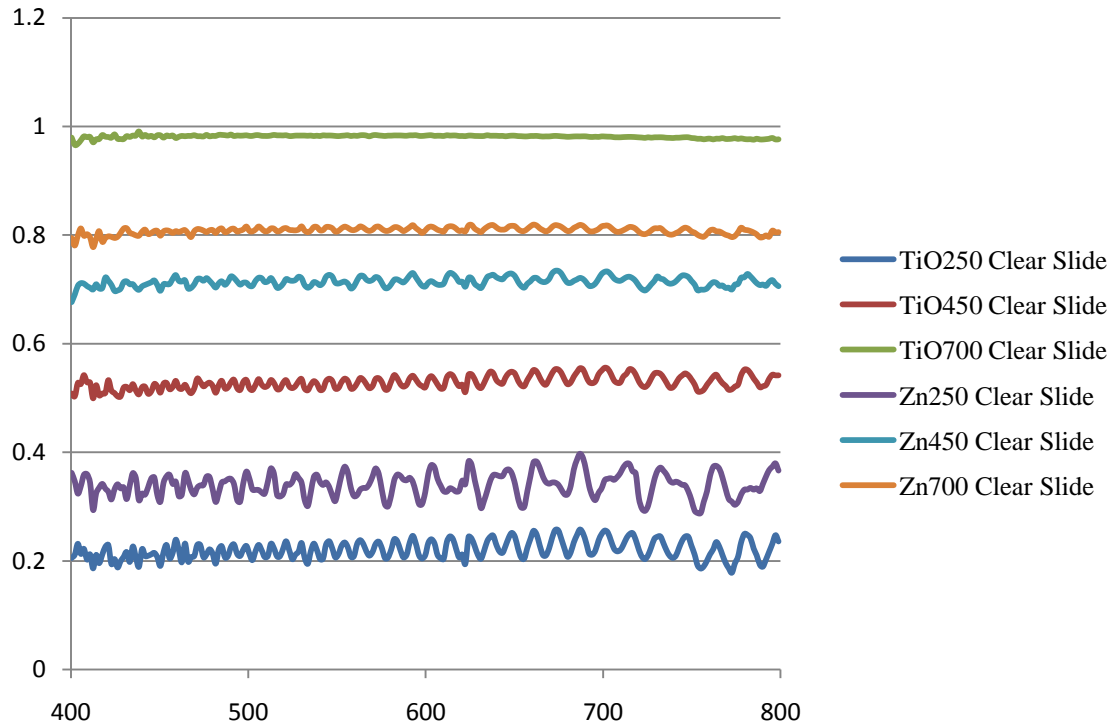


Fig. 68. Comparing Titanium Dioxide to Zinc Oxide at Different Concentrations

When coated on a clear slide, both white coatings reflect a near uniform spectrum.

Conclusions can be drawn: TiO₂ in general is more reflective at 700 mg but this is not true at 450 mg concentrations. Perhaps ZnO reaches a saturation point much sooner. Assuming maximum concentrations will be sought, TiO₂ appears to be the most reflective.

11.3. Comparing Methyl Blue at Different Concentrations on Different Samples

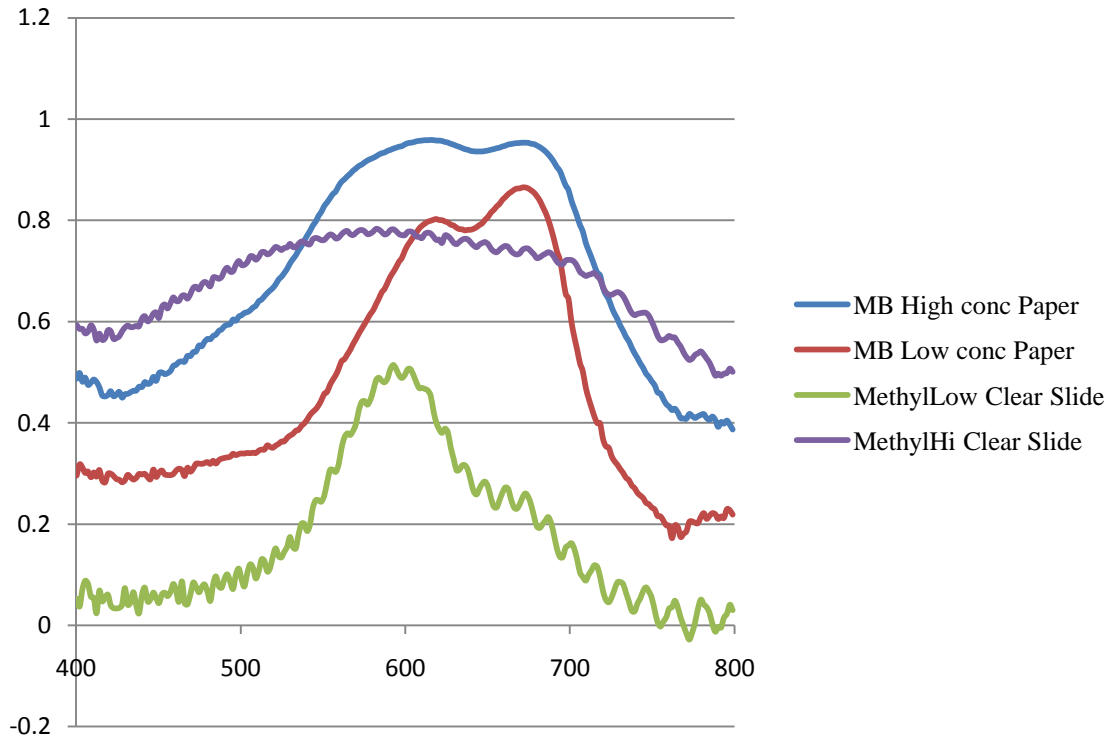


Fig. 69. Comparing Methyl Blue at Different Concentrations on Different Samples

Methyl Blue has a distinct spectrum of reflection that is clearly shifter when tested on the white paper. Concentrations themselves may also shift the spectrum as observed by the eye while doing the experiments. Methyl Blue does not appear to work well with 780 nm light, nor 532nm. A laser system with light in-between the two spectrums seems to be optimal for the methyl blue.

11.4. Comparing the Three Coatings Using Their Most Reflective Methods

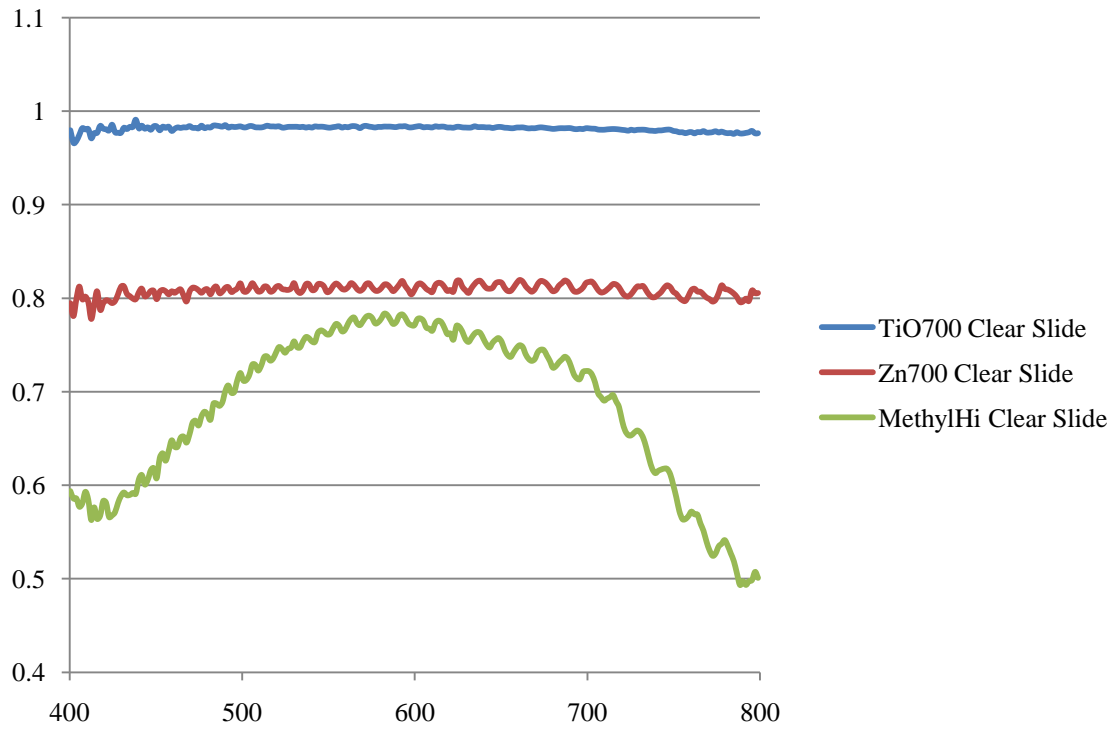


Fig. 70. Comparing the Three Coatings Using Their Most Reflective Methods

At wavelengths near 600, Methyl Blue can compare to zinc oxide, however both are worse at reflecting light than the titanium dioxide. This is clear to see.

11.5. Repeated Data Analysis Using Specific Wavelength Excitation of the Samples

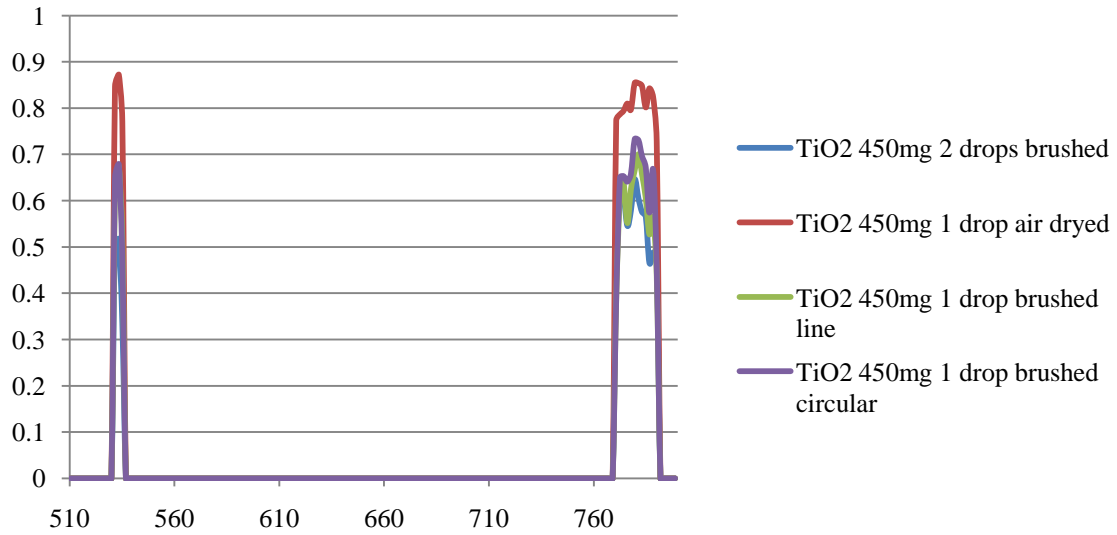


Fig. 71. Comparison of Reflectance between Application Methods of Titanium Dioxide at 400mg

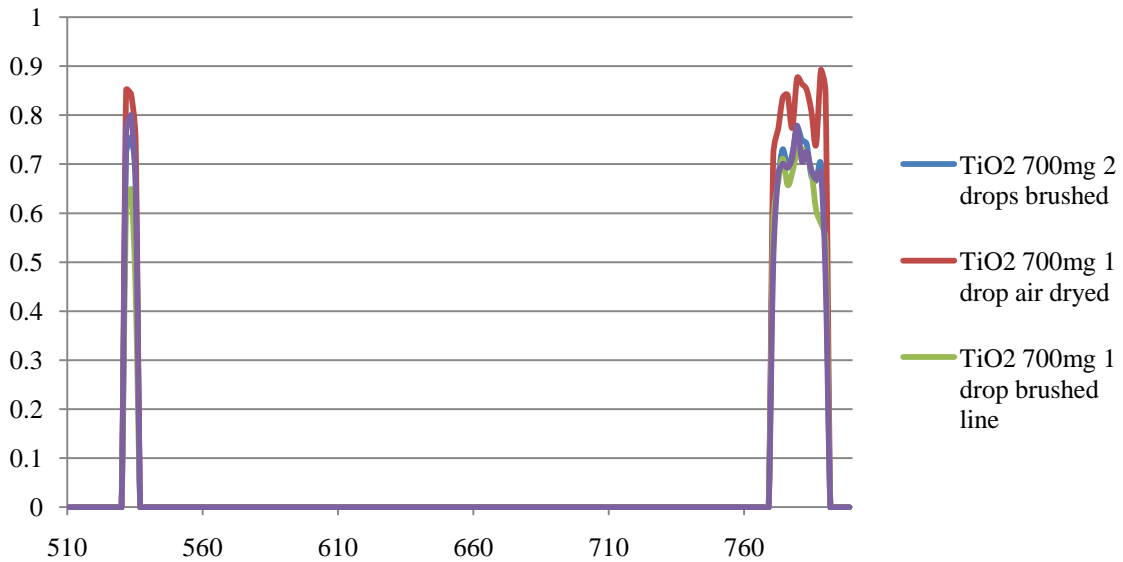


Fig. 72. Comparison of Reflectance between Application Methods of Titanium Dioxide at 700mg

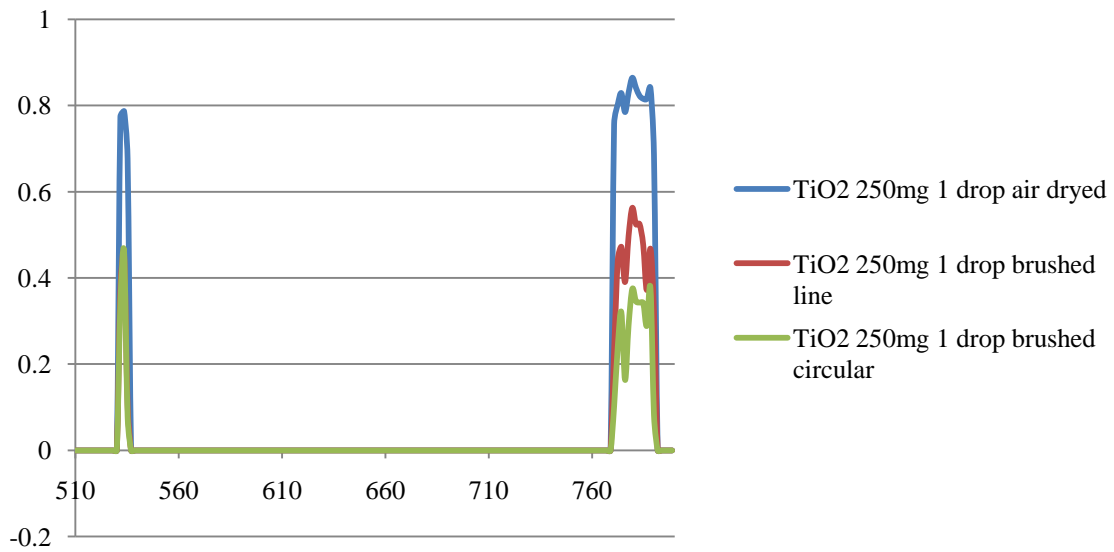


Fig. 73. Comparison of Reflectance between Application Methods of Titanium Dioxide at 250mg

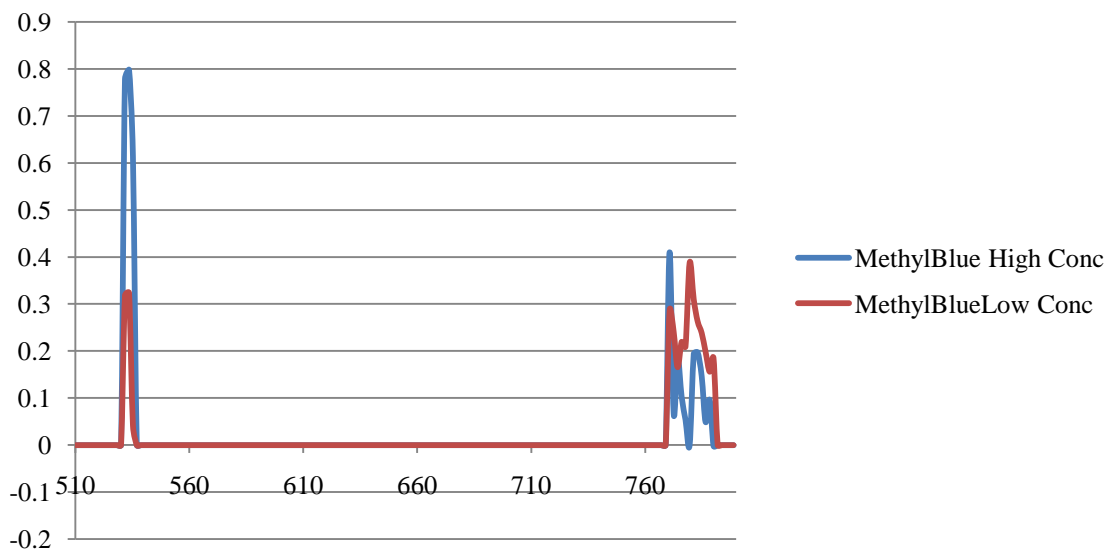


Fig. 74. Comparison of Reflectance between Concentrations of Methyl Blue

As found during white light spectral analysis, titanium dioxide dried at the 700mg / 5ml concentration is the best reflector of our specific laser lights. High concentrations of Methyl Blue may actually be satisfactory for the 532nm laser system according to our data.

Another problem that arose during the spectroscopic testing was how to ensure that the thickness of the applied coatings were uniform and evenly distributed. Variations in coating thickness and concentration sometime gave a wide range of results when performing tests on different regions of the same coated sample. To fix this, a better method of application must be sought after.

12. References

- B. Dywer, M. Maccaferri, C. Wester, "Design and Realization of a Laser Holographic Oscope," MQP, WPI-ME, 2008
- Coherent Inc. Manufacturer of Lasers: World Leader in Photonics. 2010
<<http://www.coherent.com/>>.
- Collodion; MSDS; Mavidon: Lake Worth, FL. 9 April, 2009.
<http://www.mvamed.com/MSDS_Forms/COLLODION%20%20USP%20EU.pdf>.
- E. Harrington. "Development of an Optoelectronic Holographic Platform for Otolaryngology Applications." Masters Thesis, WPI – CS, 2009
- E. Luscher. "The Functional Effect of Loading of the Tympanic Membrane." *Acta Otolaryngologica*, Vol. 33, No. 4-5 : Pages 265-272, 1945.
- E. Ventsel and T. Krauthammer, "Thin plates and shells: theory, analysis, and applications," 1937
- EdmundOptics.com. "1951 USAF Glass Resolution Targets." (2009).
<<http://www.edmundoptics.com/onlinecatalog/displayproduct.cfm?productID=1790>>.
- H. Mojallal. "Laser Tympanometry – More." 4/20/2010.
<http://www.polytec.com/int/158_11617.asp>.
- Heine. Manufacturer of High Quality Medical Diagnostics Equipment. 2010.
<http://www.heine.com/eng_US>.
- I. Karasic, N. Largesse, L. Lincoln, "Miniaturization of an optoelectronic holographic otoscope for measurement of nanodisplacements in tympanic membranes." MQP, WPI-ME, 2009
- J. Wang et al. "Nanoparticles Damage Brain Cells." *Environmental Health News*, 17 November 2008. <[http://www.neighborsagainsttheburner.org/files/Nano's_Brain.cwk%20\(WP\).pdf](http://www.neighborsagainsttheburner.org/files/Nano's_Brain.cwk%20(WP).pdf)>
- J. J. J. Dirckx and W. F. Decraemer, "Coating techniques in optical interferometric metrology," *Appl. Opt.* **36**, 2776-2782 (1997)
- J. J. J. Dirckx and W. F. Decraemer, "Reflective coatings in optical interferometry for in-vitro studies of the eardrum," *SPIE*, 2927:2-10, 1996
- J. Rosowski, J. Cheng, M. Ravicz, N. Hulli, M. Hernandez-Montes, E. Harrington, C. Furlong, "Computer-assisted time-averaged holograms of the motion of the surface of the mammalian tympanic membrane with sound stimuli of 0.4–25kHz," *Hearing Research*, 253(1):83-96, 2009.

- M. Amabili and R. Garziera, "Vibrations of Circular Cylindrical Shells with Nonuniform Constraints, Elastic Bed and Added Mass; Part 1: Empty and Fluid-Filled Shells," University of Parma, Italy, 2000
- M. E. Lutman. "Phasor Admittance Measurements of the Middle Ear I. Theoretical Approach" *International Journal of Audiology*, 13:4, 253-264, 1984
- M. Petyt, "Introduction to finite element vibration analysis," University of Cambridge Press, 1990
- N. Bapat. "Development of sound presentation system for characterization of sound induced displacements in tympanic membranes." Masters Theses WPI – ME, 2010.
- N. Hulli, "Development of an optoelectronic holographic otoscope system for characterization of sound-induced displacements in tympanic membranes," *Thesis, WPI-ME*, 2008
- Newport Corporation. 2010. <<http://www.newport.com/>>
- T. Hain. "Otoneurology." 2010. <<http://www.tchain.com/otoneurology/>>.
- Titanium Dioxide; MSDS No. T3627; Mallinckrodt Baker: Phillipsburg, NJ, November 12, 2003. <<http://www.jtbaker.com/msds/englishhtml/t3627.htm>>.
- W Han and M Petyt, "Geometrically Nonlinear Vibration Analysis of Thin Rectangular Plates using the Heirarchical Finite Element Method-1: The Fundamental Mode of Isotropic Plates," University of Southhampton, 1995
- W. Soedel, "Vibrations of Shells and Plates," Marcel Dekker, Inc., 2004
- Welch Allyn Medical Diagnostic Equipment Manufacturer. 2010. <<http://www.welchallyn.com/>>

13. Appendix A

13.1. Deformation Shape at a Frequency for a Plate Constrained at its Edges

Material Properties

Radius (m)

$$a := 0.01$$

Thickness (m)

$$h := 2.54 \cdot 10^{-5}$$

Poissons Ratio

$$\nu := 0.3$$

Modulus of Elasticity (GPa)

$$E := 120 \cdot 10^9$$

Density (kg/m³)

$$\rho := 8940$$

Solving for Frequencies:

Rank of the FnF

$$m := 1$$

Order of the FnF

$$n := 1$$

Principle Inertia

$$I_P := \rho \cdot h$$

Modulus of Rigidity

$$D := \frac{E \cdot h^3}{12(1 - \nu^2)}$$

Roots

$$\phi := \frac{(2 \cdot m + n) \cdot \pi}{2}$$

$$\lambda := \phi - \frac{(4n^2 - 1)}{8 \cdot \phi} \cdot \left[1 + \frac{1}{\phi} + \frac{28n^2 + 17}{48\phi^2} + \frac{3 \cdot (4n^2 - 1)}{8 \cdot \phi^3} + \frac{83n^4 + 54.5n^2 + 161.19}{120\phi^4} \right]$$

Fundamental Natural Frequency

$$\beta := \frac{\lambda}{a} = 461.131$$

$$\omega := \sqrt{\frac{\beta^4 \cdot D}{I_P}} = 5.988 \times 10^3$$

$$f := \frac{\omega}{2 \cdot \pi} = 953.043$$

Shape Functions

$$A := 4$$

$$C := 1 \cdot 10^{-(n+1)}$$

$$w(r, \theta, t) := (A \cdot J_n(n, r) + C \cdot I_n(n, r)) \cdot \cos(\theta) \cdot \sin\left(\omega \cdot \frac{t}{30}\right)^2$$

$$l_x := 1$$

$$u := [2 + m + .3(m - 1)]$$

$$x_n := 3l$$

$$m := 5l$$

$$(i := 0..x_n)$$

$$(j := 0..m)$$

$$r_i := a + \frac{u - 1}{x_n} \cdot i$$

$$ss_j := 2\pi + \frac{2 \cdot \pi \cdot j}{m}$$

$$k := 1.7$$

Shape in the X-axis

$$Xc_{i,j} := (k \cdot r_i) \cdot \cos(ss_j)$$

Shape in the Y-axis

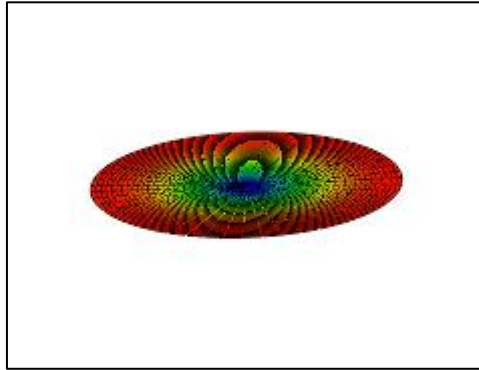
$$Yc_{i,j} := (k \cdot r_i) \cdot \sin(ss_j)$$

Shape in the Z-axis

$$Zc_{i,j} := \frac{w\left[r_i, \frac{\pi}{6}, 3 + 2^{(m-1)}\right]}{5.402}$$

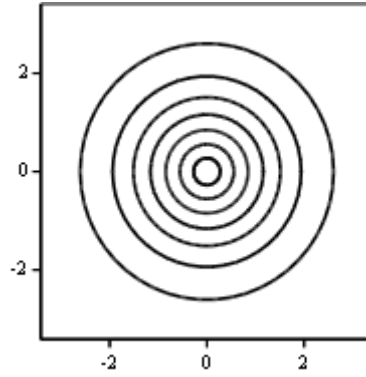
3-D and Countour Plots

3D Response



(Xc, Yc, Zc)

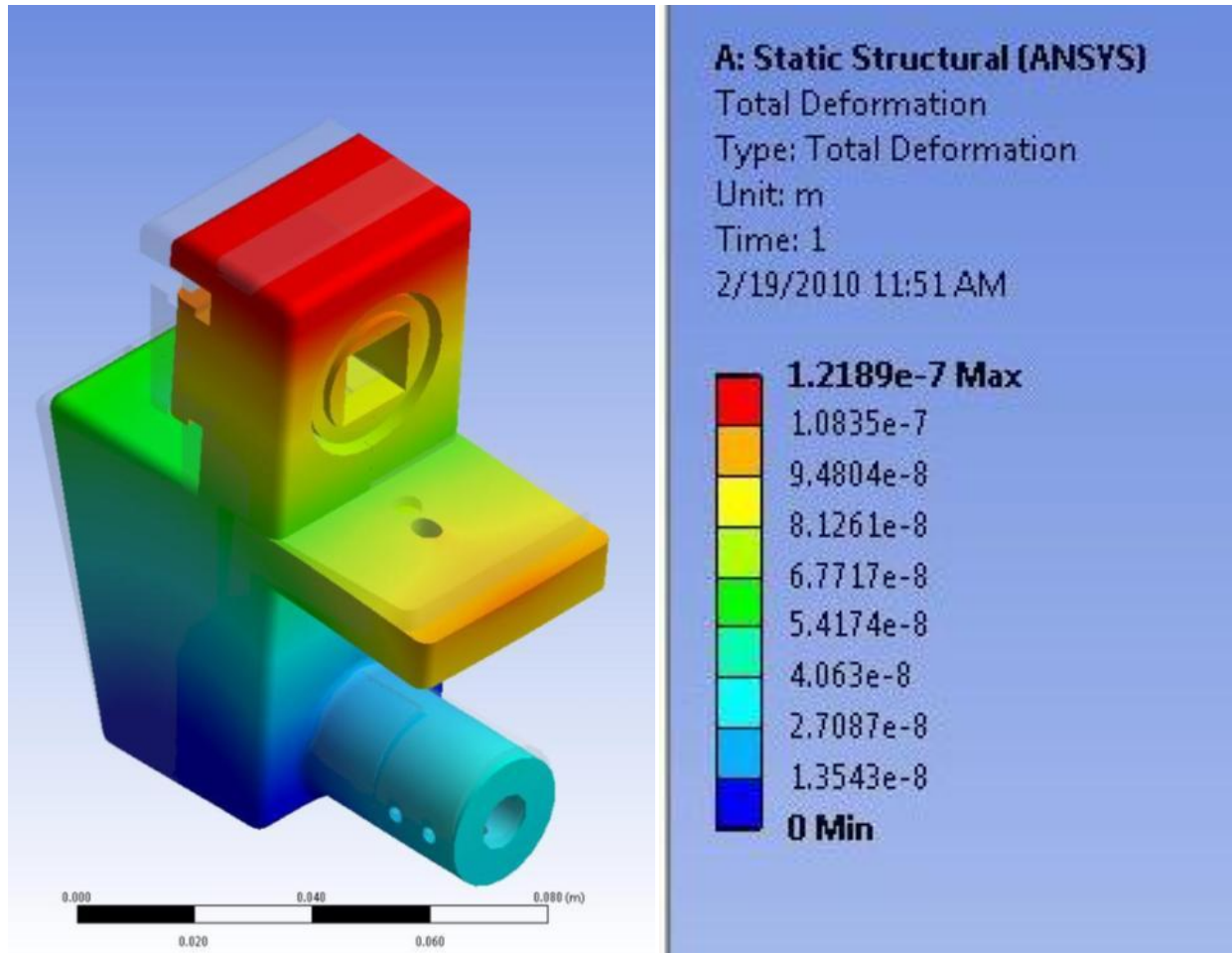
Countour Plot



(Xc, Yc, Zc)

14. Appendix B

14.1. ANSYS Analysis of Iteration 2



1

```
***** ANSYS - ENGINEERING ANALYSIS SYSTEM  RELEASE 12.0.1  *****
ANSYS Academic Teaching Advanced
00000000          VERSION=WINDOWS x64   11:55:40  FEB 19, 2010 CP=    15.600
```

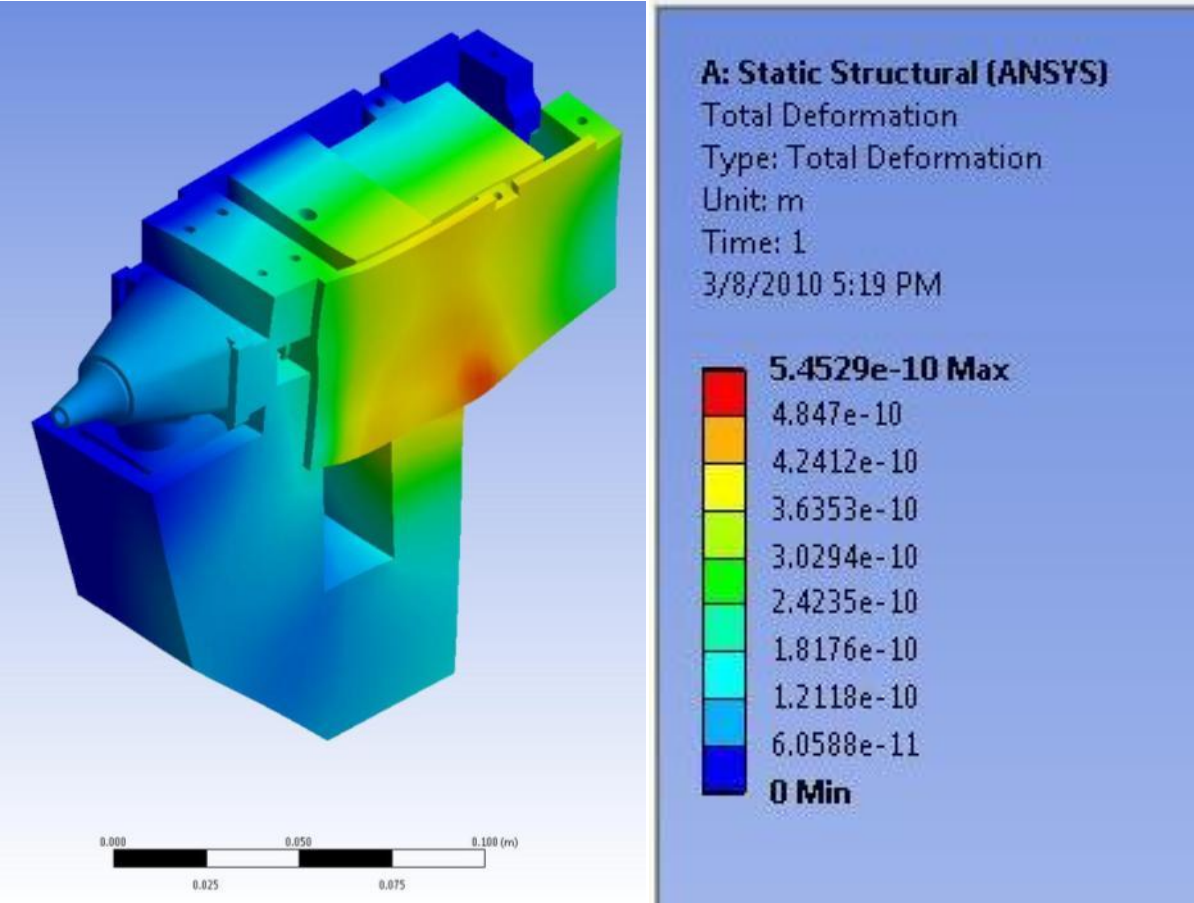
*** FREQUENCIES FROM BLOCK LANCZOS ITERATION ***

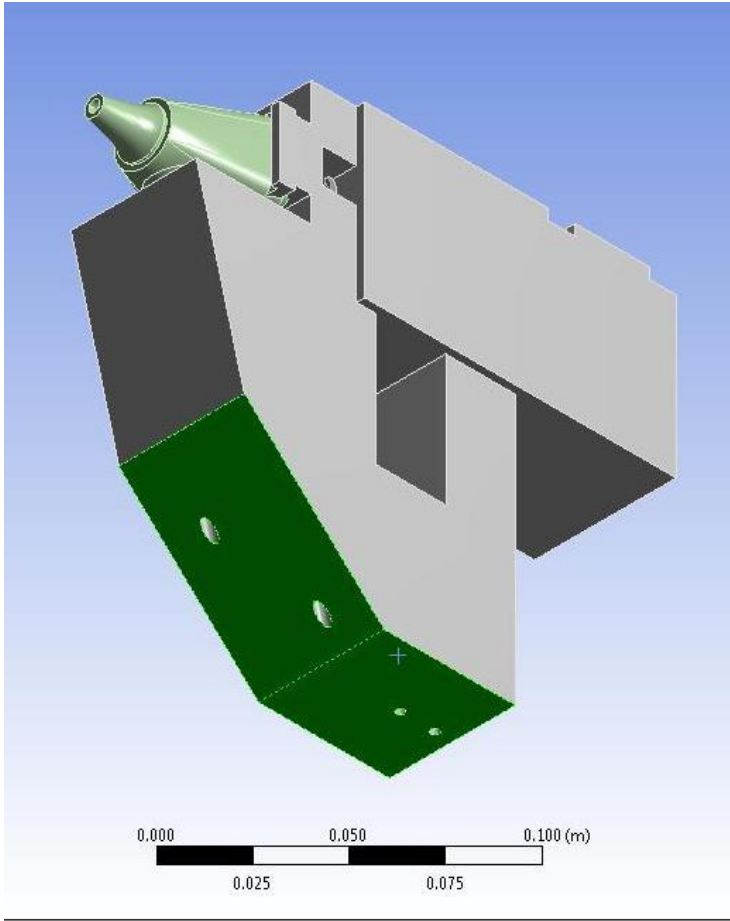
MODE FREQUENCY (HERTZ)

1	2265.775043814
2	2797.700742074
3	4989.006176454
4	5131.879005163
5	5727.529047157
6	7660.677399104
7	8534.418337221
8	9564.805710339
9	9716.046487596
10	10323.27344580
11	11312.75541455
12	15131.64446468
13	16156.34376822
14	19462.37028918
15	19656.43247494
16	19787.63568389
17	20825.38978154
18	21358.17434600
19	21687.45432387
20	22858.94000844

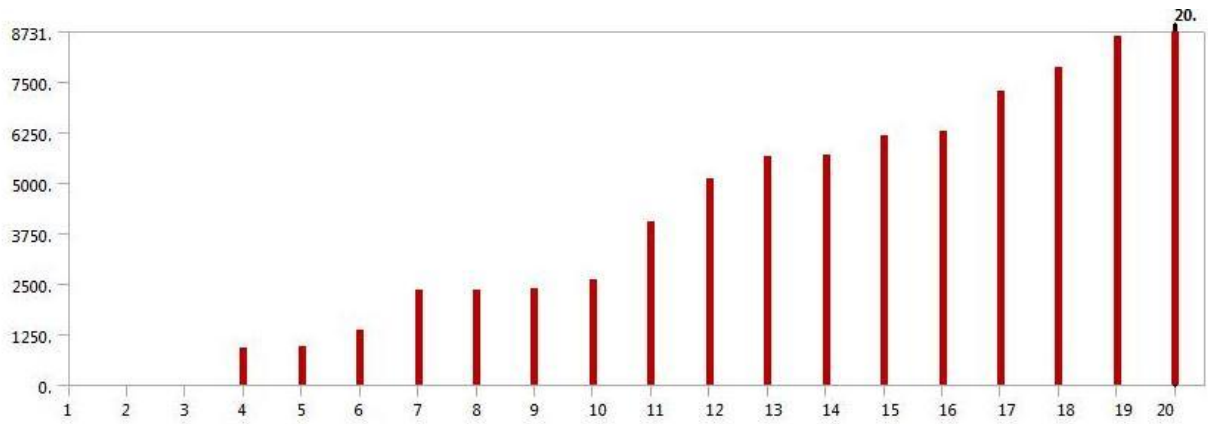
1

14.2. ANSYS Analysis of Iteration 3





	Mode	<input checked="" type="checkbox"/> Frequency [Hz]
1	1.	0.
2	2.	0.
3	3.	8.0586e-003
4	4.	930.08
5	5.	938.73
6	6.	1358.3
7	7.	2339.8
8	8.	2350.7
9	9.	2369.8
10	10.	2599.
11	11.	4045.
12	12.	5088.2
13	13.	5663.1
14	14.	5678.
15	15.	6157.4
16	16.	6261.4
17	17.	7269.3
18	18.	7845.6
19	19.	8677.4



A: Static Structural (ANSYS)

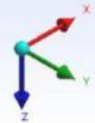
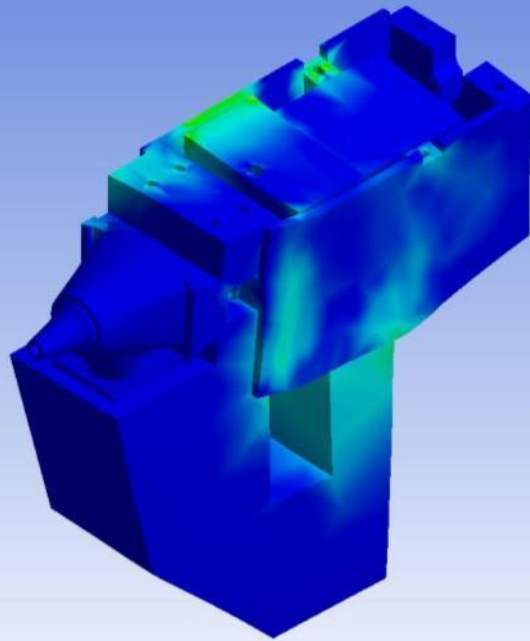
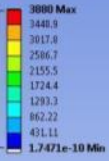
Equivalent Stress

Type: Equivalent (von-Mises) Stress

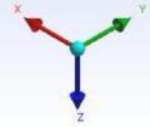
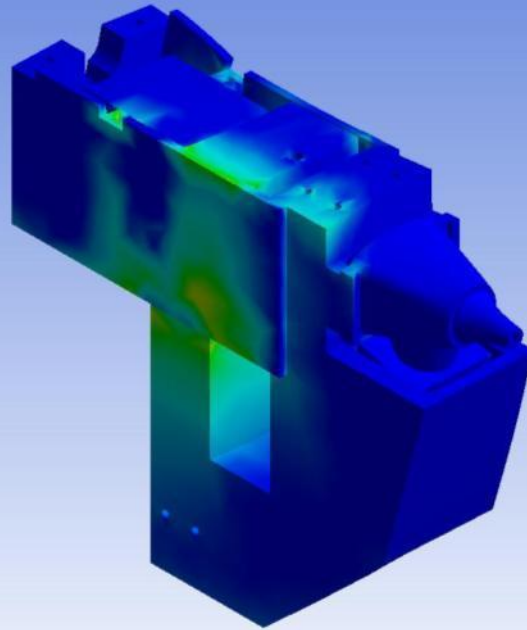
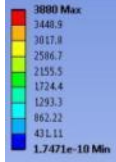
Unit: Pa

Time: 1

3/8/2018 5:28 PM

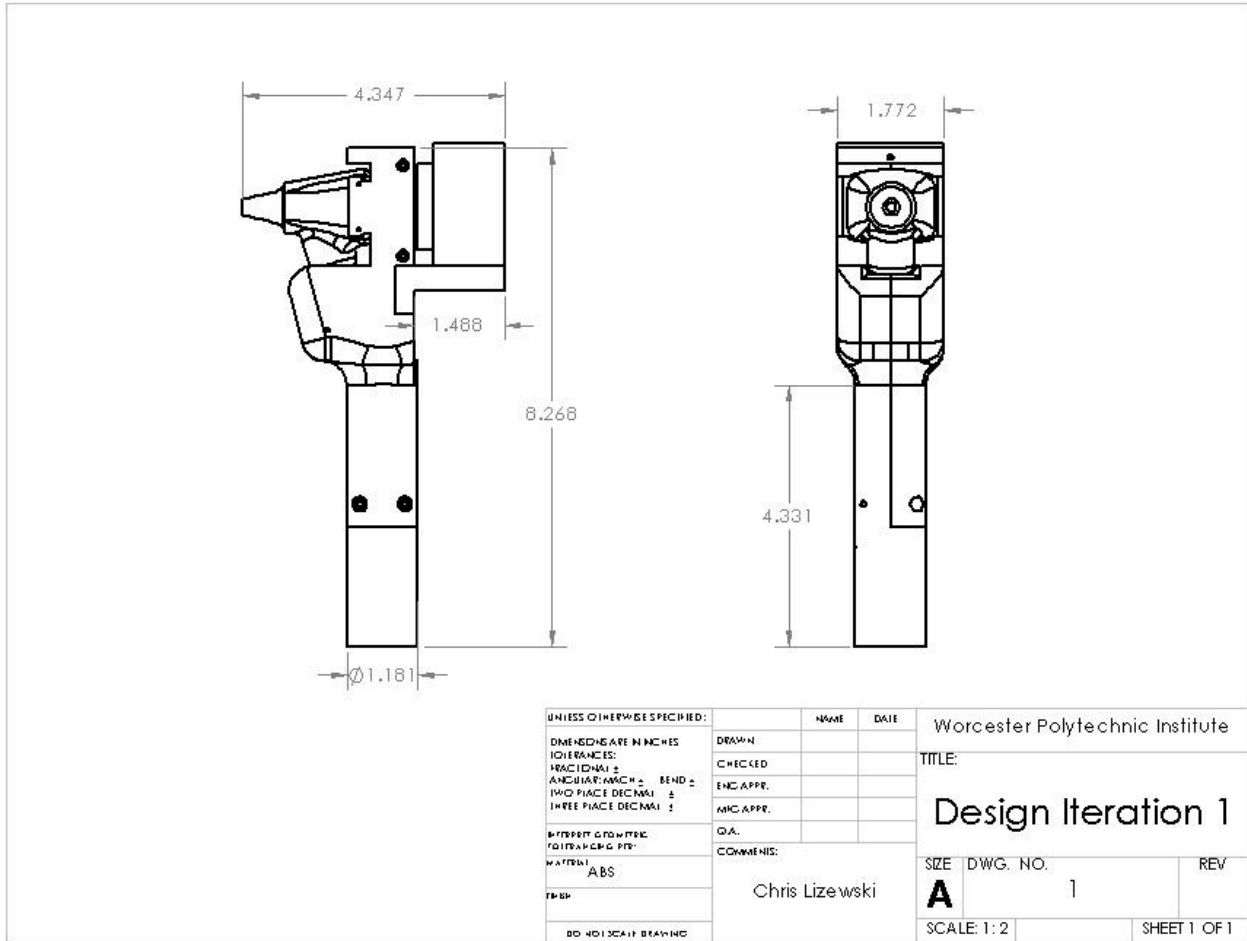


A: Static Structural (ANSYS)
Equivalent Stress
Type: Equivalent (von-Mises) Stress
Unit: Pa
Time: 1
3/8/2018 5:20 PM



Appendix C

Technical Drawing for Iteration 1



Technical Drawings for Iteration 3

